UNIVERSITY OF OKLAHOMA

GRADUATE COLLEGE

ROCK FRICTION AND DYNAMIC FAULTING AT THE MICRO- TO NANO-SCALES

A DISSERTATION

SUBMITTED TO THE GRADUATE FACULTY

in partial fulfillment of the requirements for the

Degree of

DOCTOR OF PHILOSOPHY

By

XIAOFENG CHEN
Norman, Oklahoma
2015

Downloaded from SHAREOK. Persistent Handle URL: https://hdl.handle.net/11244/14232

ROCK FRICTION AND DYNAMIC FAULTING AT THE MICRO- TO NANO-SCALES

A DISSERTATION APPROVED FOR THE
CONOCOPHILLIPS SCHOOL OF GEOLOGY AND GEOPHYSICS

BY

_____
Dr. Ze'ev Reches, Chair

_____
Dr. Andrew S. Elwood Madden, Co-Chair

_____
Dr. David London

_____
Dr. Amy B. Cerato

_____
Dr. Barry R. Bickmore

© Copyright by XIAOFENG CHEN 2015
All Rights Reserved.

Acknowledgements

Here I take this opportunity to express my gratitude to those who supported and helped me throughout my PhD project. I am thankful for their continuous support, aspiring guidance, friendly advice, constructive criticism, and illuminative discussions.

First and foremost, I express my deepest gratitude to my advisor, Dr. Ze'ev Reches, for his continuous support, advising, encouraging, and guidance throughout my PhD study. You guided me switching from Engineering to Geology and you are the best example showing me how to become a good person and a good scientist. Your endless passion toward unknowns, hardworking spirit, confidence, and optimistic attitude are all precious resources that will benefit my whole life. "One day as a teacher, a life as a father". Thanks Ze'ev for all you've taught me.

I offer my sincere appreciation to my advisor, Dr. Andrew Madden, who guided me through such big turnaround from engineering to Geology smoothly and without him this could not happen. Your hands-on instructions on every subtle experimental steps, insightful lecturing, constructive suggestions, and warm encouragements are sincerely appreciated. Thanks Andy for all the opportunities to let me learn from your spirit of responsibility, rigorous attitude, carefulness, and hardworking.

I deeply thank my committee member, Dr. Barry Bickmore at Brigham Young University, for providing me the opportunity to realize the micro-friction measurements and serving as my committee. The trip to Utah is a great experience and a learned a lot from there. Thanks Barry for your continuous support and encouragement.

I also thank Dr. David London and Dr. Amy Cerato for being my committee. I appreciate for the learning opportunities you provided and your continuous support.

My completion of this project could not have been accomplished without the support of my colleagues: Yuval Boneh, Zonghu Liao, Jefferson Chang, Mathew Miller, Andrew Swindle, and Brittany Pritchett. I appreciate the time being with you.

I thank all my family members Chen Qiliang, Wang Xiuhua, Xu Genlong, and Wang Yaping. I know I cannot express enough thanks to you all. But, you are everything to me.

Finally, to my caring, loving and supportive wife, Xu Hui, for accompanying me these years. I remember all the sacrifice you've done to our family: your hardworking to support our family, your countless time cooking for me, and your bringing up of our new family member, Ethan Chen. Thank you, my dear, for all the love you gave me.

Table of Contents

Acknowledgements iv

List of Tables x

List of Figures xi

Abstract xxiv

Chapter 1: Introduction 1

Earthquake and rock friction 1

Rock friction apparatuses 1

Dynamic fault strength and basic friction laws 1

Mechanisms and models of dynamic friction 5

Present research motivation and organization 8

Chapter 2: Experimental systems 10

ROGA system 10

Loading and power system 10

Control and monitoring 12

Powder shear with CROC 12

Friction experiments 13

Solid rock sample preparation 13

Powder sample preparation 14

Friction experiment procedure 14

Microscopic analysis 15

Sample collection 15

Analysis techniques 16

Chapter 3: Effect of roughness on friction 21

Introduction 21

Methods and materials 22

Results 24

Friction coefficient 24

Fault surface roughness 27

Friction-velocity relations 28

Discussion 31

Supplementary information 32

Rock friction experiments 33

Atomic Force Microscope utilization 34

Friction coefficient data 39

Nano-morphology analysis of the fault surfaces 45

Chapter 4: Powder-rolling as a mechanism of dynamic fault weakening 48

Introduction 48

Materials and Methods 51

Test apparatus 51

Micro-analysis techniques 52

Experimental results 53

Mechanical data 53
Micro-structure: smooth surfaces and powder rolls 55
Analysis 61
Formation and life cycle of powder rolls 61
Frictional strength and powder-rolling 63
Rolling friction mechanics 64
Application to present experiments 69
Discussion 70
Faulting conditions that enhance powder-rolls formation 70
Powder-rolling as an effective fault weakening mechanism 73
Summary 74
Chapter 5: Frictional melting of granite faults as mechanical and material phase-transition 75
Introduction 75
Background 76
Microstructure Observations 78
Mechanical results 81
Friction experiment results 81
Phase-transition of weakening-strengthening 83
Discussion 86
Melt-welt: Weakening in gabbro and Strengthening in granite 86

A conceptual model for frictional strength evolution of granite faults 89
Supplementary information 93
Rock samples composition 93
Experimental conditions 94
Chapter 6: Shear experiments of confined gouge 95
Approach 95
Talc gouge shear experiments 96
Mechanical data 96
Microstructural observations 100
Shear of dolomite and ooid grains 101
Cross-section features 102
Fault zone surface structure 104
Shear experiments of gypsum grains 105
Micro-structure 105
Mineralogy 107
Summary 108
Compaction 108
Localization 108
References 109

List of Tables

Table 1 Summary of AFM friction measurements 41

Table 2 Friction coefficient results in AFM measurements 42

Table 3. Summary of experiments with the RRG sample. Rolls quality is defined in the text and Fig. 25. Loading Conditions are: 1, for constant velocity; 2, for ramp velocity (velocity rise then drop); 3, for constant power-density. 54

Table 4. Experimental conditions of the experiments for diorite and granites with weakening-strengthening transition. 94

List of Figures

Figure 1. Shear stress as a function of normal stress for different rock types from Byerlee (1978). The slopes of the best-fit lines are 0.85 and 0.6, which describe the static rock friction values..... 2

Figure 2. Schematic illustration of the rate- and state-variable friction laws from Scholz (1998). The values of empirical parameters *a* and *b* are shown in the plot. In this case, $a-b<0$, meaning a velocity weakening as seen in the plot. 3

Figure 3. Steady-state friction coefficient as a function of slip rate for different of experiments on various rock types from Di Toro et al. (2011). The general trend is stable, high friction of 0.6-0.8 for slip rates less than 1-10 cm/s, a decrease of friction with slip velocity from 10 cm/s to 1 m/s, and the lowest friction coefficient occurring at 1 m/s. 4

Figure 4. Friction coefficient as a function of slip velocity for granite, from Reches and Lockner (2010). There is a stage of velocity weakening from 1 mm/s to 5 cm/s, followed by a stage of velocity strengthening from 5 cm/s to 30 cm/s, with the final stage of velocity weakening at high slip rates. 5

Figure 5. The earthquake deformation apparatus. A. Generalized cross section displaying main power train components. B. 3D view of the assembled apparatus. C. General view of the system. D, E. Blocks of Sierra White granite used in the present experiments. LB-lower block; UB-upper block; SR-sliding ring; TC-thermocouple wires; IR-infra red sensor; EG-gouge ejected from the sliding ring. D.A vertical cut-through the blocks in a finite-element model showing model geometry and temperature distribution due to frictional heating. E. Sample blocks assembled in the loading frame;

note two thermocouple (TC) wires cemented into the sliding ring. (Reches and Lockner, 2010)..... 11

Figure 6. Control and monitoring system of ROGA. A. The National Instruments hardware for system control and digital data collection. B. The front panel of the ROGA software program developed in our lab coded with Labview. 12

Figure 7. The confined rotary cell. A. CROC parts including a powder loading chamber and another loading cylinder before assembly. B. CROC been assembled and placed into the ROGA. C. Close-up view of the teeth design with the porous metal plug. 13

Figure 8. Example of collected samples. A. A piece of hard crust knocked off from the friction experiment of Kasota Dolomite. Note the color variations, fracture patterns, and striations on the fault surface. B. Two pieces of gouge flakes in the petri dish collected from the radiant red granite friction experiments. Note the curvy, shining, and striated top surfaces. C. Cross sectional view of the CROC experiment run with ooid grains after epoxy treatment and polishing. The red color was due to the doping of a chemical heat indicator which turned to red when temperature reached ~200℃. Note the preservation of teeth on top and bottom, principal slip surface near top wall, fractured grains in the middle, and visible ooid grains in the lower part..... 16

Figure 9. A schematic illustration of the AFM working principles. The interaction between tip and sample surface was tracked by monitoring the position change of a laser beam spot which was reflected from the back of cantilever top. 3D Scanning was achieved by controlling the piezoelectric scanner. (From Madden, et al., Welcome to Nanoscience.) 17

Figure 10. Basic AFM friction measurement methods. A. The so-called friction loop collected in an AFM lateral method, in which the tip slides laterally against the sample surface in a back-and forth cycle. Note the original signal of lateral cantilever deflection in Volts. B. Representative force-distance curve with hysteresis collected using the AFM axial method. The interaction between the colloidal probe and sample surface was illustrated in an exaggerated form (from Kosoglu et al., 2010). 19

Figure 11. Fault surfaces. A. Scanning Electron Microscopy (SEM) image of an experimental fault of Kasota dolomite. B. The experimental fault surface of Kasota dolomite after run 1516 of the present study. C. Atomic Force Microscopy (AFM) image of sheared surface of Kasota dolomite (run 1516); note the distinct, clear striations at sub-micron spacing and a few fine grains (elevated bright spots). D. 3D view of C. E. AFM morphology map of un-sheared Kasota dolomite surface; note irregular, rough surface. F. AFM image of sheared surface of Sierra White granite; note the faint slickenside striations in general N-S direction, fine grains and damage (hole in the center). 23

Figure 12. A. The sub-micron friction coefficients (FC) determined with the AFM glass-bead method on experimental fault surfaces of Kasota dolomite (KD) (run 1516) and Sierra White granite (SWG) (run 1614), and the macroscopic FC in the final stage of these experiments. Horizontal axis is arbitrary; each symbol indicates tens to hundreds of repetitions with standard deviation error bar. Note the FC variations with orientations (normal and parallel to slickensides) and conditions (room-dry and wet). B. History of the FC (green), slip velocity (blue), and thermocouple temperature plotted with respect to distance (experiment 1516). 26

Figure 13 A. Power-spectral-density (PSD) of surface roughness of the marked surfaces. The PSD data of the present work were calculated for tens of AFM profiles of the marked length. Note the two end member of cleaved biotite (smoothest) and un-sheared surface (roughest), and the roughness difference between striation-parallel and striation-normal roughness. B. roughness-friction relations at micron scale. Shown: room-dry FC and the AFM roughness of Kasota dolomite and Sierra White granite surfaces (roughness as RMS for 1 μm segments), diamond sample A (Hayward et al., 1992), and Westerly granite (Byerlee, 1967) (roughness as Ra). The relations have the form (solid line): FC=a ln(roughness) + b, where (a, b) are (0.13, 0.99) for KD-SWG combined, (0.13, 0.67) for diamond A, and (0.16, 0.29) for Westerly granite..... 29

Figure 14. Macroscopic steady-state FC and slip velocity of Kasota dolomite. The plot includes 85 data points determined in constant velocity and stepping-velocity experiments (Boneh, 2012). Final FC of experiment 1516 (Fig. 12B) is marked by blue square..... 30

Figure 15. Velocity loading history and corresponding friction and temperature for Sierra White granite run 1614. 34

Figure 16. The AFM colloidal probe geometry. A. An SEM image of the fabricated glass-bead probe for our Nano R2 AFM platform. The glass-bead diameter is 50 μm and the cantilever length is 100 μm. B. 1D AFM profile of the glass-bead (red) compared to ideal sphere shape (black); note asperities and roughness at submicron scale. 35

Figure 17. Schematic illustration of the interaction between glass bead and sample surface with respect to the force curve. Inset displays the cantilever geometric parameters needed for friction coefficient calculations (after Kosoglu et al., 2010) 36

Figure 18. Representative force curves of the AFM friction measurement method. 40

Figure 19. An example of normal and frictional force calculations following Stiernstedt et al. (2005). The plot displays the normal force vs. shear force for Site 33, SWG, parallel, room dry. 43

Figure 20. Calculated shear stress vs normal stress during AFM friction measurements for Kasota Dolomite (A), Sierra White Granite (B), and Biotite (C). 44

Figure 21. A: Examples of four 1D profiles across the KD fault surface on AFM image (inset). The two slip-parallel profiles (blue lines in inset) are significantly smoother than the slip-normal profiles (red line in inset). B: Synthetic profiles with the marked slope (β) in the PSD curve generated with MatLab. 46

Figure 22. Cohesive, shiny, powder flakes formed on experimental faults during slip. A: Fault surface showing several pieces of flakes formed on the slip surface (run 3253). B: The curvy powder flakes; note the difference in smoothness on flake top surface (left) and the bottom surface (right) (run 3251). C: SEM view of a flake cross-section showing internal 3D structure, with the substrate loosely compacted with relatively coarse grains, and the top smooth surface (~0.3 μm thick) with dense compacted finer grains (run 2716). D: SEM view of the bottom side of a powder flake that was attached to the host rock block showing rough surface made of loose agglomerated coarse grains (run 2683). E: General view of the powder flake surface showing patches of smooth areas with powder rolls oriented normal to striations (run 2600). 52

Figure 23. Experimental friction evolution with slip distance. A: Constant-velocity experiment at 0.036 m/s (run 3243). B: Power-controlled experiment in which the power-density (=shear stress × slip-velocity) was maintained constant by the feedback control (run 2600). 55

Figure 24. Close-up views of powder rolls. A: Rolls developed on smooth PSZ. Note sub-micron size thin platelets wrapping up the rolls stacking on the PSZ surface (red arrows) (run 2832). . B, C and D: deformation of the PSZ surfaces below rolls while rolls maintain round (run 2683, 2554, and 2807 for B, C, and D, respectively). The asymmetric deformation are marked as the inward arrow in the gentle-depressed sides and the outward arrow in the abrupt depressed sides. White arrows indicate rolling direction of rolls. E: Well compacted rolls with solid interior. Note the composing grains of <100 nm (run 2716). F and G: broken rolls left traces on PSZ surface showing smearing of materials and axial fracturing. White arrows indicate rolling direction (run 2600, 2704 for F and G, respectively). H: two rolls twisted against each other (run 2716) 58

Figure 25. General view of rolls showing the quality of powder rolls from the best (quality A) to worst (quality D) for runs 3243, 3243, 2813, and 3249. 60

Figure 26. Statistics of rolls diameter and orientation on 14 SEM images of 1183 rolls. A: Frequency distribution of rolls diameter measured on SEM images with average diameter of 1.04±0.25 μm. B: Rolls' orientation with respect to slip direction showing an average of 95 °± 26 °from slip. 60

Figure 27. Proposed formation mechanism and life cycle of powder rolls. A: Slip localization within a narrow zone (PSZ), a few microns thick, inside the gouge layer. B:

SEM image of the cross section of the PSZ showing formation of a PSZ as a layer of compacted ultra-fine grains resting on a porous matrix of coarser grains (Fig. 22C). C: Debris of grains, agglomerated grains and delaminated PSZ between the two smooth PSZ surfaces. D: Rolling of the debris (left) into powder rolls (center), and eventual destruction (right side). Shear direction marked by half arrows. 62

Figure 28. Correlation between rolls and friction reduction. A: The final friction coefficient, μ_f, as a function of initial friction coefficient, μ_f, for all experiments. Note that runs with rolls (red dots) are plotted below the friction equality line indicating friction reduction, whereas runs without rolls (blue dots) are distributed around the equality line indicating minor weakening or strengthening. B: Normalized final friction coefficient, μ_f / μ_i, as function of slip distance. Runs with rolls (red dots) showed systematic dependence of μ_f / μ_i on slip distance (dashed curve and equation) that agrees with the observations of Zanoria et al., (1995a, b) (purple dots). Runs without rolls (blue squares) show no systematic friction reduction for similar slip-distances. 65

Figure 29. Rolling friction of powder rolls. A: Idealized two-dimensional model, after Eldredge and Tabor (1955) and Tabor (1955), of a cylindrical roll of diameter D and length L sheared between two softer slip surfaces. The stressed roll penetrates the slip surface over penetration zone of width d/2 and penetration depth b (text). B: Rolling friction coefficient, μ_R, as function of the penetration ratio, D/d; inset: μ_R as equation 4 in the text. C: AFM morphology of a single roll (bright zone trending NW-SE) resting on PSZ surface (run 2810); note the the roll is ~ 1 μm higher than the substrate. D: AFM morphology of the PSZ surface after the powder roll was pushed away with AFM tip; note N-S depression about 100 nm deep of the removed roll. E: A

series of seven profiles derived from across the AFM images of C and D normal to the roll. The four upper curves, taken in C, delineate both the PSZ and top of the roll. The three lower curves, taken in D, delineate the PSZ without the roll and reveal the shape and depth of the depression. A red circle of D = 0.85 μm was visually fitted to be bound by the upper and lower profiles; this circle is the idealized roll that was removed. Note that the down-facing parts of the roll cannot be traced by the AFM tip and thus the upper profiles cannot accurately delineate the sides of the roll. The roll penetrated the PSZ over a region of d/2 ~ 0.29 μm (yellow arrow). 68

Figure 30. A friction map (after Boneh et al., 2013) displaying normalized final friction coefficient, μ_f/μ_i , as function of normal stress and slip velocity. Symbol size is proportional to the normalized friction and the circle color indicates the presence (red) or absence (blue) of rolls. Note the strong correlation of low friction with rolls presence. 71

Figure 31. Examples of frictional melt on gabbro. A. Friction-distance curve for gabbro sample sheared at normal stress of 1.4 MPa, equivalent velocity of 0.85 m/s, and total slip of 78.65 m. Note the initial weakening from a to b, the transient strengthening from c to d, and the exponential decay from d to e. Peak strength occurred at d, corresponding to the onset of visible frictional melt covering whole fault. Adapted from Hirose and Shimamoto (2005). B. Friction (red), sample shortening (green), and slip velocity (blue) as functions of slip distance for the gabbro sample sheared at normal stress of 20 MPa, slip velocity of 3 m/s, and total slip of 6 m from Niemeijer et al. (2011). 77

Figure 32. Microstructural observations of post SWG 1592 products with SEM. A. General view of the top of fault surface in a cohesive flake, with visible striation patterns from left to right and the rougher edges in top and bottom. B. Enlarged view of the zone of striations. Note the concentric striations and horizons within bands of striations. C. Magnified view of the striation zone with highly porous structure. Note the stretching of melt drops along slip direction, and visible sub-micron grains embedded within and attached to melt drops. D. Striation zone close-up view. Note the flattening on the melt top and stretched melt similar to the simple shear structure. E. Sub-micron glassy fibers in the close-up view, note solid grains attached to the fibers in the center and larger fractured grains in the lower left. 80

Figure 33. Summary of friction-distance curves for SWG and diorite runs at constant velocities. Experiment #, normal stress, and slip velocity are shown in the text box inside each plot. The transition from initial weakening to transient strengthening can be seen in these cases. A final weakening stage followed the transient strengthening can be seen in cases A, C, and F. 81

Figure 34. Friction, temperature, and dilation as a function of slip distance for sierra white granite run 1592. Initial weakening tended to stabilize after 2 m of slip, and the strengthening transition started at ~8 m. The peak friction occurred at ~21 m followed with a decay of friction until a stable value of 0.4. The temperature increased from 23 ℃ to 110 ℃ and dropped to 93℃ in the end. Wear was small in the initial weakening stage, but increased in the strengthening period. Note the wider and spikier friction response in the strengthening period, and the temporal dilation accompanied with friction strengthening..... 82

Figure 35. Normal stress (blue, left axis) and shear stress (red, right axis) response during the transition from initial weakening to the strengthening period for both granite and diorite. Note the systematic temporal increase of normal stress and shear stress during the transition. 84

Figure 36. Slip distance required until weakening-strengthening transition as a function of dissipative power density in log-log scale. Note the general power law relationship showing the higher the dissipated power density the shorter the distance required for strengthening. 85

Figure 37. Left: Initiation of melt streaks formation with gabbro under normal stress of 4 MPa, velocity of 6.5 cm/s, and slip distance of 9.5 meters. Note the two SEM images to the right showing melting on dark streaks and non-melt on surfaces with gouge powder. Right: Three examples of the gabbro friction experiments showing the initiation of weakening was accompanied with the transient increase of normal stress, indicative of volumetric expansion against the normal stress. Adapted from Brown and Fialko (2012). 86

Figure 38. Steady-state friction coefficient as a function of slip rate for gabbro, from TsuTsumi and Shimamoto (1997) and Brown and Fialko (2012). Note the friction coefficient at velocity ranges of 5-30 cm/s is about 0.6-0.8. 88

Figure 39. Cumulative distance until the weakening-strengthening transition as a function of dissipative power density (A) and elapsed time till weakening-strengthening transition as a function of dissipative power density (B). Blue data are from gabbro weakening transition by Brown and Fialko (2012). Note the consistency in power law dependence and slope variation in both cases. 89

Figure 40. A. The evolution of friction coefficient as a function of slip for granite rock sheared at moderate velocity. Data from SWG run 1592 with normal stress of 1.22 MPa and constant slip rate of 4.8 cm/s. Four regions can be categorized as Initial stage, initial weakening, transient strengthening, and final weakening. B. Friction-distance curve for gabbro sample sheared at normal stress of 1.4 MPa, equivalent velocity of 0.85 m/s, and total slip of 78.65 m (same as Fig. 31). Note the similarity between A and B. C. Friction versus slip velocity. Experimental friction values for 35 runs with 254values; each dot is the average friction value at a velocity interval; standard deviation bars are shown only for two runs for sake of clarity; yellow shading bound the data without outliers. D. A proposed model, modified after Reches and Lockner (2010) for friction-velocity relation of a granite fault. Stage I. Initial setting, initial wear, no lubrication; Stage II. Cumulative wear, critical gouge layer and powder rolling lubrication; Stage III. Local melting leading to strengthening; Stage IV. Final weakening, possible bulk melting of the fault zone. 92

Figure 41. Friction (red) and velocity (blue) as a function of slip distances for talc run 3380 (A) and 3388 (B). Velocity values are 0.002 m/s, 0.06 m/s, and 0.018 m/s. Displacements are 0.01 m per stage; normal stress was 3.3 MPa 97

Figure 42. Friction coefficient as a function of slip velocity for both dry (solid circle) and wet (hollow circle) talc powder runs; 19 experiments with 114 velocity-friction pairs. Note the low friction value of wet talc compared to dry talc, and the consistent velocity strengthening in dry talc. 98

Figure 43. Fault-normal dilation as a function of slip distance (log scale) for wet (A) and dry (B) talc. Each plot contains a set of runs for the same sample. Velocity were at

0.002 m/s, 0.006 m/s, and 0.018 m/s. Normal stress was 3.3 MPa. Wet talc runs show, after the initial large compaction, decreased compaction rates but no dilation. Dry talc runs show, after initial large compaction, compaction rate decrease that eventually switched to dilation..... 99

Figure 44. Side view of the dry talc powder sheared at velocity of 0.002 m/s and normal stress of 2.6 MPa for 3.5 m. Note the through-cutting Riedel shears within the talc powders..... 100

Figure 45. SEM images for the dry (3391) and wet (3376) talc powder fault surfaces developed after shearing experiments. Both faults showed well-developed fault plane. Note small submicron grains in dry talc surfaces, while few submicron grains in wet talc surfaces 101

Figure 46. Cross section view of the fault zones. A. dolomite gouge 3165, cut normal to slip direction. B. Ooid grains 3169, cut normal to slip. C. Ooid grains 3169, cut along slip direction. 102

Figure 47. SEM images of cross sections for Kasota dolomite gouge experiments (3160 and 3165), ooid gouge (3169), and dolomite solid rock (1516, E). A, D, and E were cut normal to slip direction. B and C were cut along slip direction. 103

Figure 48. High-resolution SEM images of fault surface structures for gouge experiments with KD and ooid grains. 104

Figure 49. SEM images of the gypsum fault surfaces. A. General view of the well-developed fault surface, with visible striations. B. Close-up view of the fault surface showing the constituent elongated gypsum grains. C. Zoom-in view of the flat surfaces composed of round nano-grains. D. General view of the powder roll along fault

surfaces. E. An aggregated roll lying on top of a flat substrate, note the elongated grains in the bottom surface. F. Close-up view of the roll structure showing the constituent nano-grains. 106

Figure 50. XRD pattern for the gypsum (green) and the post-shearing gypsum fault surface (blue). Note the bassinite peaks in the post-shear material (pink). 107

Abstract

An earthquake occurs when the shear resistance of a crustal fault drops from static friction to dynamic friction during slip. Understanding fault weakening mechanisms is essential for the understanding of earthquake processes. The commonly used rock friction laws are the Byerlee friction law for static-friction (friction between non-moving surfaces, $\mu_S = 0.6 \sim 0.85$, Byerlee, 1978), and the Dieterich rate- and state-friction law for dynamic weakening (Dieterich, 1978). High-velocity slip experiments (velocity from ~1 mm/s to a few m/s), made possible by recent advances in experimental rock shearing instrumentation, revealed new and significant behavior, e.g., strong dynamic weakening at seismic slip rates (Di Toro et al., 2011), or dynamic strengthening (Reches & Lockner, 2010). These new observations challenge the long-standing paradigms. While most previous studies included friction measurements at the macroscopic scale (larger than a few cm^2), my research focuses on friction measurements at the micron- to nano- scales. The dissertation presents three mechanisms that are active at these scales, and which can effectively lead to macroscopic dynamic weakening or strengthening.

Chapter 2 summarizes the experimental methods for the rock friction tests and the microscopic characterization techniques. The experimental faults are composed of granite, diorite, dolomite and limestone, and were sheared at high-velocity (up to 1 m/s) under ambient room temperature and humidity, and normal stress of a few to 14 MPa. Analyses of fault surfaces prior to and after shearing utilized Atomic Force Microscopy (AFM) for surface morphology mapping, Scanning Electron Microscopy (SEM) for surface characterization, the AFM colloidal probe method for measuring friction at the

sub-micro scale, and X-Ray Diffraction (XRD) and electron microprobe (EPMA) for mineralogical analysis.

Chapter 3 presents a systematic investigation of the relations between **surface roughness/smoothness** and fault frictional strength. The roughness of the experimental fault surfaces, as represented by their power-spectral-density, correlates well with the measured friction coefficient at the sub-micron scale. The analysis shows that reduced fault roughness by slip leads to the fault weakening, in agreement with the macroscopic observations.

Chapter 4 focuses on **powder rolling on granitic faults**. The analysis revealed micron-size cylindrical powder rolls that are spontaneously formed and destroyed during granitic faults slip at moderate velocities (0.001-0.1 m/s). The friction reduction due to the powder rolls was calculated using a rolling friction model with good fit to observations. The observed strong correlation between roll occurrence and fault weakening suggests that powder rolling is an effective dynamic weakening mechanism. Further, powder rolling is a likely physical mechanism to explain the enigmatic powder lubrication

The effect of **frictional melting** of granitic rocks is presented in Chapter 5. I found direct SEM evidence for shear-melting of granite faults that slipped for long distances (tens of m) at moderate slip rates (~ 0.05 m/s). The friction evolution in these experiments was complex: from initial weakening to temporary strengthening, and to the final weakening. The switch from initial weakening to strengthening is related to the phase transition from solid gouge grains to local melting, and its timing is proportional

to the dissipative energy. Widespread melt lubrication governs the final weakening similar to bulk melting along gabbro faults.

A summary of preliminary results of high-velocity shear experiments with confined gouge layer appears in Chapter 6. The investigation includes microstructural analysis of experimental fault cross-section produced by focused ion beam milling, fault surfaces, and shear-induced mineralogical alterations in powders of talc, dolomite, clay, and San Andreas gouge. I compared the microstructural results of the solid rock experiments and the gouge layer experiments, and found that slip localization is essentially the in both configurations. I concluded that the development of a central thin principal slip zone structure is critical for the dynamic fault weakening.

Chapter 1: Introduction

Earthquake and rock friction

Frictional behavior of fault-zones controls the slip stability of faulting and earthquakes, and has been a focus of earthquake research for decades. The classical paper of Brace and Byerlee (1966) indicated that stick-slip behavior, a spontaneous jerking motion of repeating "stick" and "slip" events during frictional sliding is an experimental analog of natural earthquakes in the crust. The associated stress drop, or dynamic weakening, is required for the unstable slip of earthquakes. Recent high speed rock friction experiments showed a systematic weakening trend when the slip rate approaches seismic slip rates of ~ 1 m/s (Di Toro et al., 2011) regardless of rock type.

Rock friction apparatuses

Rock friction apparatuses belong to two general categories, direct shear and rotary shear. In direct shear systems (single-sided shear, double-direct shear, or triaxial saw-cut), the rock blocks are under normal stress and sheared in a linear fashion. This design allows for large normal stresses or high confining pressure, but is limited to small displacements (< a few mm) and usually low velocities (< 0.01 m/s). The rotary shear design, on the other hand, can shear at high-velocities (a few m/s) and unlimited slip distances, but are limited to moderate normal stress (< 40 MPa) and no confining pressure. I used the rotary shear apparatus ROGA (ROtary Gouge Apparatus) in the University of Oklahoma that was built by Dr. Ze'ev Reches in 2008.

Dynamic fault strength and basic friction laws

The widely accepted rock friction laws include the empirical Byerlee's law (Byerlee, 1978) for static friction in the brittle regime, and the empirical rate- and state- friction

(RSF) law of Dieterich (1978) and many followers (Scholz, 1998). Byerlee's law (Fig. 1) indicates a universal friction coefficient in the form of Coulomb's criterion that is independent of rock type and normal stresses,

$$\tau = C + \mu_s \sigma_n$$

where τ is the shear stress, C is fault cohesion, μ_s is the static friction coefficient, and σ_n is the normal stress. Byerlee's compilations (Fig. 1) show that

C = 0 and $\mu_s = 0.85$ for $3 < \sigma_n < 200$ MPa, and

C = 60 $\pm$10 and $\mu_s = 0.6$ for $\sigma_n > 200$ MPa

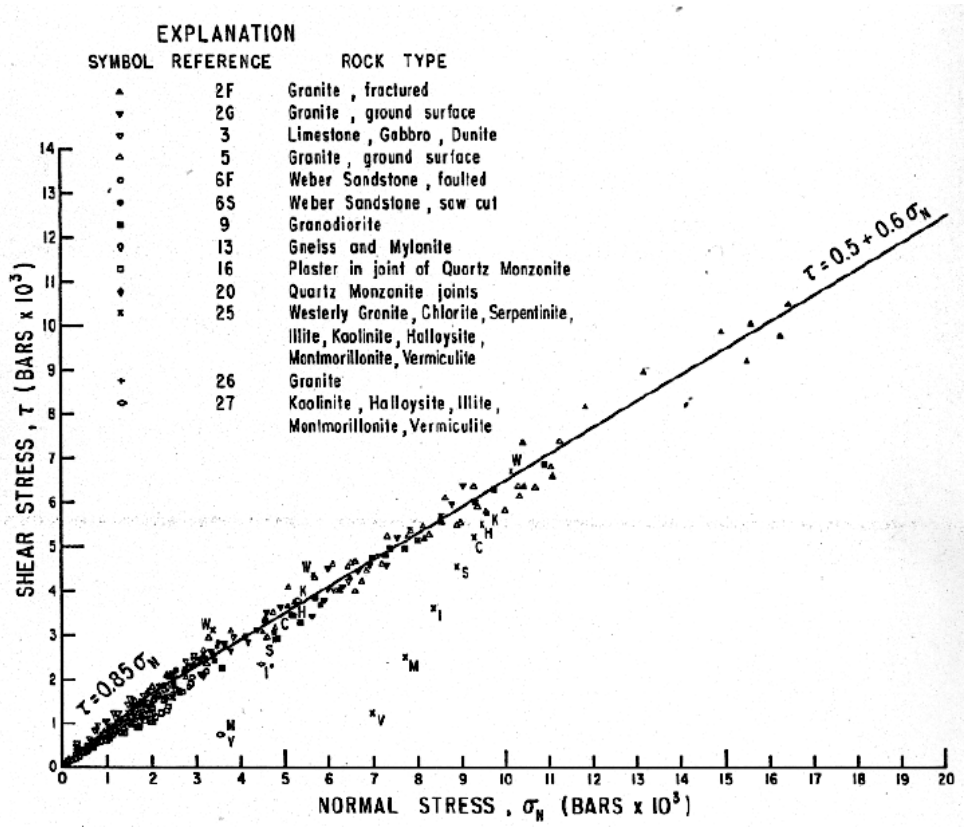

Figure 1. Shear stress as a function of normal stress for different rock types from Byerlee (1978). The slopes of the best-fit lines are 0.85 and 0.6, which describe the static rock friction values.

This law indicates the friction coefficient that must be exceeded to initiate slip, and it is frequently used to estimate the large-scale strength of the brittle, upper crust (e.g., Zoback and Zoback, 1981).

The dynamic rate- and state- friction (RSF) is expressed as (Dieterich and Kilgore, 1994):

$$\tau = \left[\mu_0 + a\, ln\left(\frac{V}{V_0}\right) + b \ln\left(\frac{V_0\theta}{L}\right)\right]\sigma_n$$

where τ and σ_n are shear and normal stresses, V for slip velocity, V_0 for reference velocity, μ_0 for steady state friction at $V=V_0$, *a* and *b* are empirical experimental values related to material properties, L is the critical distance, and θ is the state variable which evolves as

$$\frac{d\theta}{dt} = 1 - \frac{\theta V}{L}$$

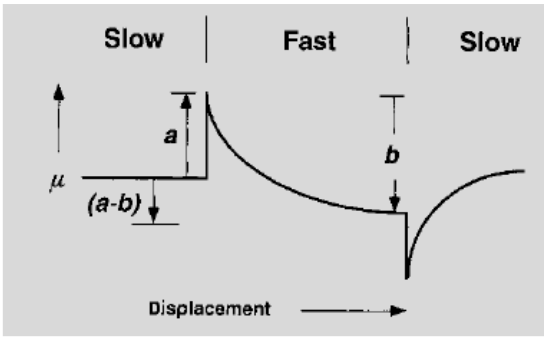

Figure 2. Schematic illustration of the rate- and state-variable friction laws from Scholz (1998). The values of empirical parameters *a* and *b* are shown in the plot. In this case, *a*-*b*<0, meaning a velocity weakening as seen in the plot.

(Fig 2). The RSF law incorporates the effects of both slip distance (L) and slip velocity. The values of *a*-*b* is of central importance in indicate slip stability: *a*-*b* < 0 indicates velocity weakening (the faster the slip, the lower the friction), and *a*-*b* > 0 indicates

velocity strengthening (the faster the slip, the higher the friction). Velocity weakening is likely to induce unstable slip, e.g., earthquake rupture, and velocity strengthening stabilizes the fault; thus, the *(a-b)* became a vital parameter in the earthquake research community (Scholz, 1998). However, Di Toro et al. (2011) and Liao et al. (2014) suggested that as RSF is derived empirically at very low velocities (< 0.001 m/s), it probably cannot represent the dynamic friction at seismic velocity of ~ 1 m/s.

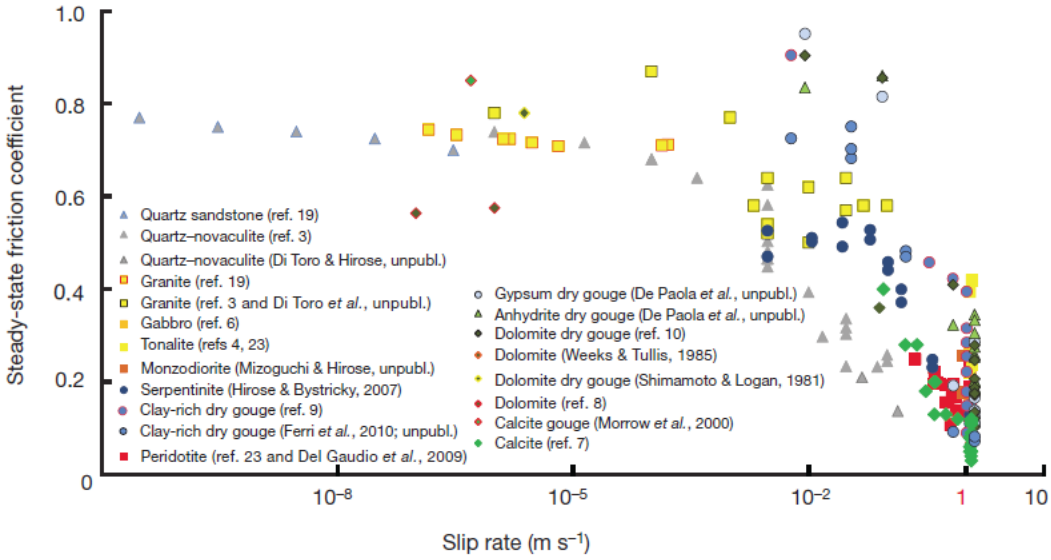

Figure 3. Steady-state friction coefficient as a function of slip rate for different of experiments on various rock types from Di Toro et al. (2011). The general trend is stable, high friction of 0.6-0.8 for slip rates less than 1-10 cm/s, a decrease of friction with slip velocity from 10 cm/s to 1 m/s, and the lowest friction coefficient occurring at 1 m/s.

During the last two decades with the development of rotary shear machines, the frictional behavior of faults was extensively explored at high-velocities ranging from ~mm/s up to ~m/s. A important finding from these experiments is the strong dynamic weakening and velocity dependence of fault strength as slip rates approach the seismic slip rates of 1 m/s, for many lithologies (Di Toro et al., 2011) (Fig. 3). A few other works on granitic rocks show a different trend of velocity strengthening in moderate

velocity ranges from 0.05 to 0.3 m/s (Reches and Lockner, 2010; Mizoguchi and Fukuyama, 2010; Kuwano and Hatano, 2011) (Fig. 4).

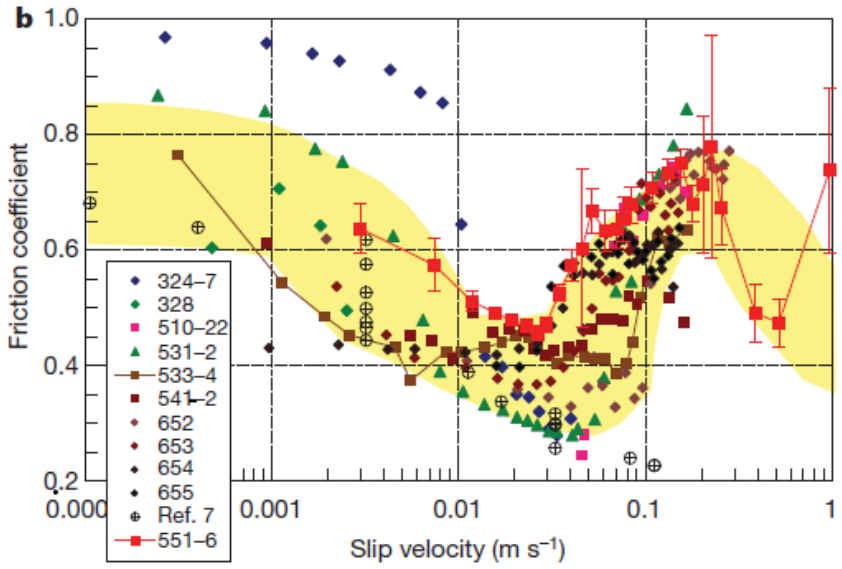

Figure 4. Friction coefficient as a function of slip velocity for granite, from Reches and Lockner (2010). There is a stage of velocity weakening from 1 mm/s to 5 cm/s, followed by a stage of velocity strengthening from 5 cm/s to 30 cm/s, with the final stage of velocity weakening at high slip rates.

Mechanisms and models of dynamic friction

Several conceptual and quantitative models have been proposed to explain dynamic friction in general, and dynamic weakening in particular. The common models are:

1. *Intense deformation at interacting asperities on fault surfaces* (Amontons, 1699; Bowden and Tabor, 1954; Dieterich and Kilgore, 1994). The asperity deformation model assumes that shear force is proportional to the normal force, independent of apparent contact area. The friction coefficient can be expressed as $\mu = \tau_0 A$, with A as the true contact area, and τ_0 as the shear strength of the material. The true contact area is proportional to the normal load (Dieterich and Kilgore, 1994; Rubinstein et al., 2004) and creeps linearly with logarithmic time (Dieterich and Kilgore, 1994;

Marone, 1998). This model provides good explanations for the independence of friction coefficient with normal stress as in Byerlee's law and frictional healing (increase of static friction during stationary contact), but it fails in situations with fault lubricant, such as gouge formation during high velocity or long slip distance.

2. *Melting due to frictional heating* (Hirose and Shimamoto, 2005; Niemeijer et al., 2011; Del Gaudio et al., 2009). The frictional melting mechanism is based on experimental observations of low friction when a melt layer covered the fault surface. Shear was accommodated within the molten layer as continuous layers of melt developed, and friction was related to the viscosity of the melt (Hirose and Shimamoto, 2005; Fialko, 2005).
3. *Thermal decomposition of carbonates* (Han et al., 2007a, b). It was observed that thermal decomposition of carbonate minerals coincided with strong dynamic weakening during high speed experiments of carbonates (Han et al., 2007a, b). Carbonates are chemically unstable at temperatures above 834 ℃ (limestone) and 778 ℃ (dolomite), at which point they decompose into oxides with the emission of CO_2 (Gunasekaran and Anbalagan, 2007). The decomposition was suggested as a mechanism for weakening (pore fluid pressurization), but later on it was found that strong dynamic weakening was observed at high speed even in experiments with the products of carbonate thermal decomposition (lime) (Han et al., 2010). Thus, whether thermal decomposition accompanied slip on carbonate faults or was the cause for dynamic weakening remains unclear.
4. *Powder lubrication within a developing gouge laye*r (Reches and Lockner, 2010; Han et al., 2010). Proponents of powder lubrication observed that nanoparticulate

gouge form consistently during slip along all faults in nature and experiments (Simen Tov et al., 2013; Reches and Lockner, 2010). They used the engineering concept and practice of solid lubrication (Wornyoh et al., 2007), and attributed fault weakening to the existence of a freshly formed gouge layer.

5. *Flash heating at contacting asperities* (Rice, 1999; Goldsby and Tullis, 2011). This model attributes the weakening to a few, highly stressed asperity contacts that were heated to relatively high temperature, and thus deform more easily (Rice, 1999, 2006; Di Toro et al., 2011; Goldsby and Tullis, 2011).
6. *Silica-gel lubrication along silica rich faults* (Goldsby and Tullis, 2002; Di Toro et al., 2004). Silica-gel is a mixture of amorphous silica with water generated during friction experiments on silicate rich rocks. Goldsby and Tullis (2002) and Di Toro et al. (2004) attributed fault weakening to the thixotropic behavior of the silica gel which gets weaker with intense shake or shear.
7. *Thermal pressurization due to water evaporation in low permeability fault zones* (Andrews, 2002). This mechanism assumes that the fluid pressure increases with frictional heat and weakens the fault by reducing the effective normal stress (applied normal stress minus pore pressure) (Andrews, 2002).
8. *Clay minerals in the fault zone*. The flaky crystal structure in many phyllosilicate minerals have weak bonding between sheets, leading to high stress anisotropy with much weaker shear strength along the plane parallel to the sheet (e.g., talc and mica). Shear re-orientation of clay mineral grains facilitate shear and reduce the fault friction (Collettini et al., 2009; Boutareaud et al., 2012).

9. *Elastohydrodynamic of fluidized gouge between rough fault surfaces* (Brodsky and Kanamori, 2001). A thin layer of fluidized gouge that is sheared between rough surfaces supports part of the load by lubricating the contacts between asperities and thus reduces the associated friction.

Present research motivation and organization

The mechanisms mentioned above are mostly based on experimental observations, with a few proved in the field (e.g., clay mineral, carbonate thermal decomposition, frictional melt). Some of the proposed mechanisms are linked to clear, physical, observations such as the melt lubrication and fabrics of clay minerals. However, most of the mechanisms lack direct physical evidence or have incomplete description at the relevant scale. My dissertation addresses three outstanding unknowns of rock friction.

First, what is the control of fault surface roughness on frictional strength? The Bowden and Tabor model predicts that a smooth surface with multi-asperity contacts will have high friction due to the increase of real contact area. Yet, daily experience indicates that smooth surfaces have lower friction than rough ones.

Second, while powder lubrication is apparently effective at macroscopic scale, as shown by wide use in industry (Wornyoh et al., 2007), there is no nano-scale model that explains the lubrication mechanism by solid, nano-powders.

Third, the systematically occurrence of velocity strengthening in granite during high-velocity (Reches and Lockner, 2010) contradicts the flash heating model. This strengthening was explained by granular flow mechanics (Kuwano and Hatano, 2011) and water dehydration (Sammis et al., 2011) models; these models have their limitation, and I searched for a better one.

My approach to investigate the above questions is analysis of the physical processes at the micro- to nano-scale through macro-scale rock friction experiments that are linked to micron-to-nano scale processes. The dissertation includes five chapters.

Chapter 1 (present chapter) outlines the basic background, motivation and objectives of this work, as well as a general framework for the dissertation.

Chapter 2 outlines the experimental methods for the rock friction tests and the ultra-microscopic characterization techniques.

Chapter 3 deals with the roughness effect on frictional strength and shows the results of micro-friction at fault surfaces, quantify the fault surface roughness, and correlates surface roughness with micro-friction to demonstrate the effect of slip smoothing along faults on dynamic weakening. This analysis was published in Geology as Chen et al., 2013 "Dynamic weakening by nanoscale smoothing during high velocity fault slip".

Chapter 4 presents the discovery of powder rolls along experimental fault, and analyzes rolling friction as a likely mechanism of dynamic weakening. I present a detailed microstructural characterization of the micro-size powder rolls to show how the powder rolls formed, rolled, and lead to the dynamic weakening. A manuscript version of this chapter is currently under review in Earth and Planetary Science Letters.

Chapter 5 summarizes my recent work on frictional melting on granitic rocks during slip at moderate velocities (< 0.1 m/s). I present evidence for melting in the granite experimental faults and the associated friction evolution over long slip-distances. The experiments reveal that a weakening-strengthening mechanical transition occurs together with the phase transition from solid gouge particles to partial melt within the fault zone.

Chapter 2: Experimental systems

ROGA system

Rock friction experiments were conducted in the high velocity ROtary Gouge Apparatus (ROGA) at the University of Oklahoma. ROGA includes three main components: (1) Loading system; (2) Control and monitoring system; and (3) a Confined ROtary Cell (CROC) to test gouge powder under confined conditions and elevated pore-pressure.

Loading and power system

ROGA's frame is 1.8 m tall with two decks (Fig. 5 A-C) that are connected to each other by four internally enforced rectangular legs. The normal stress was applied onto the sample (Fig. 5 D, E) by a rotary train from below and the normal stress pump from above. The power system includes:

(1) A 100 HP three-phase motor and controller that provides constant torque of up to 3,000 Nm from 0 RPM to 3300 RPM. The motor velocity is monitored and controlled through an 8192 sector encoder.

(2) A 225 kg flywheel to boost motor torque; it is engaged with a pneumatic clutch.

(3) An electro-magnetic large clutch that is capable of full engagement in 30 ms.

(4) A hydraulic piston system with axial load up to 9,500 N.

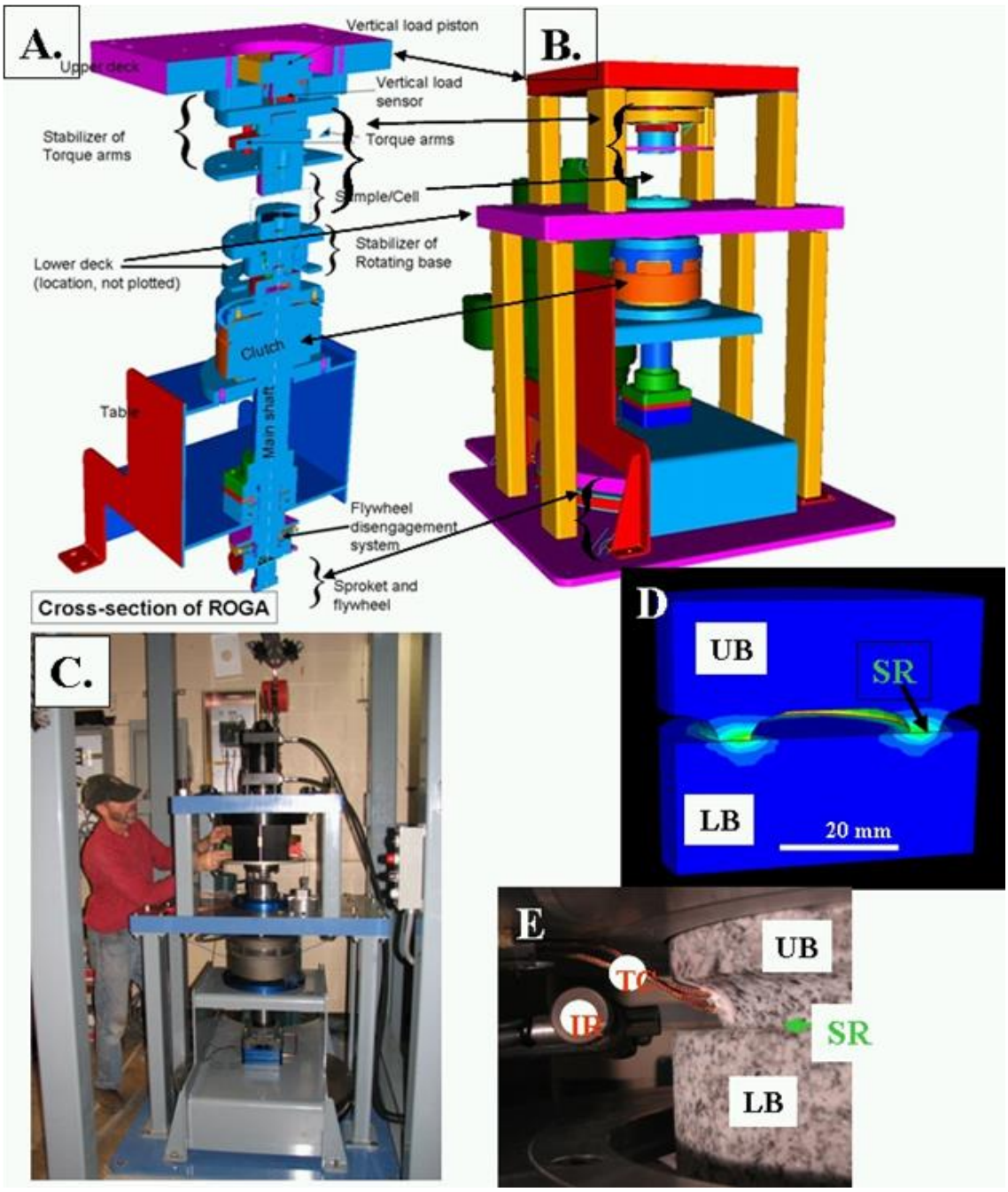

Figure 5. The earthquake deformation apparatus. A. Generalized cross section displaying main power train components. B. 3D view of the assembled apparatus. C. General view of the system. D, E. Blocks of Sierra White granite used in the present experiments. LB-lower block; UB-upper block; SR-sliding ring; TC-thermocouple wires; IR-infra red sensor; EG-gouge ejected from the sliding ring. D.A vertical cut-through the blocks in a finite-element model showing model geometry and temperature distribution due to frictional heating. E. Sample blocks assembled in the loading frame; note two thermocouple (TC) wires cemented into the sliding ring. (Reches and Lockner, 2010)

Control and monitoring

The control and monitoring system is based on National Instruments components, and it includes a SCXI-1100 with modules 1124 (analog control) 1161 (relay control), 1520 (load cell/strain gage), and 1600 (data acquisition and multiplexer), as well as a USB-6210 (encoder measurements) (Fig. 6A), with digital sampling rate up to 10 kHz. The National Instrument LabView platform was used as main control software (Fig. 6B). Load-cells for axial load and torque are made by Honeywell, gouge dilation/compaction is measured with four eddy-current sensors (about 1 micron accuracy), temperature measurement is with thermo-couples, and sample velocity is monitored by a velocity encoder.

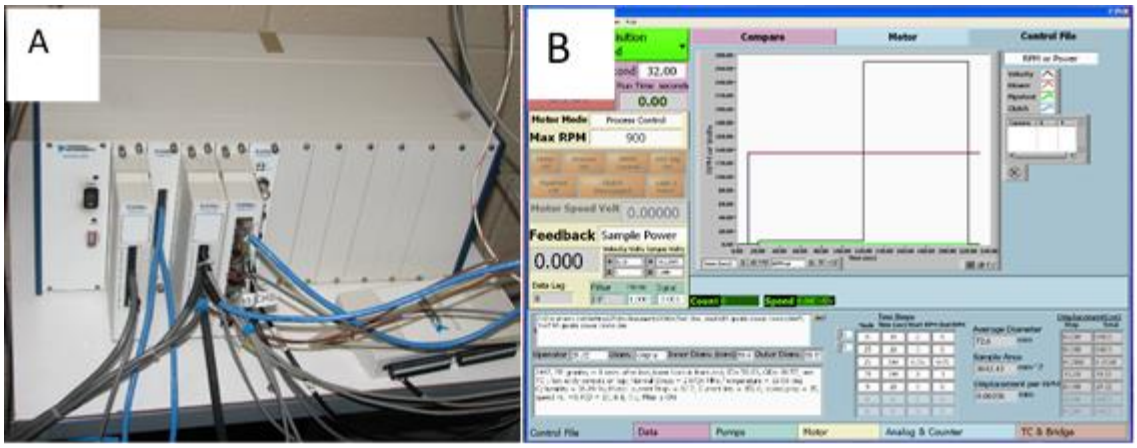

Figure 6. Control and monitoring system of ROGA. A. The National Instruments hardware for system control and digital data collection. B. The front panel of the ROGA software program developed in our lab coded with Labview.

Powder shear with CROC

The powder material experiments described in Chapter 6 were conducted in a Confined ROtary Cell (CROC) which is loaded by the loading apparatus described above. CROC can shear a granular layer either under dry or wet under pore-pressure

controlled by two syringe pumps. CROC includes a ring-shape gouge chamber of inner diameter of 62.50 mm and outer diameter of 81.25 mm, and up to a 3 mm thick gouge sample (Fig. 7A). To reinforce shearing within the powder layer (Fig.7), the metal contact surfaces facing into the cell were shaped with teeth (Fig. 7C). The porous metal plug (Fig. 7) enables water injection during shearing

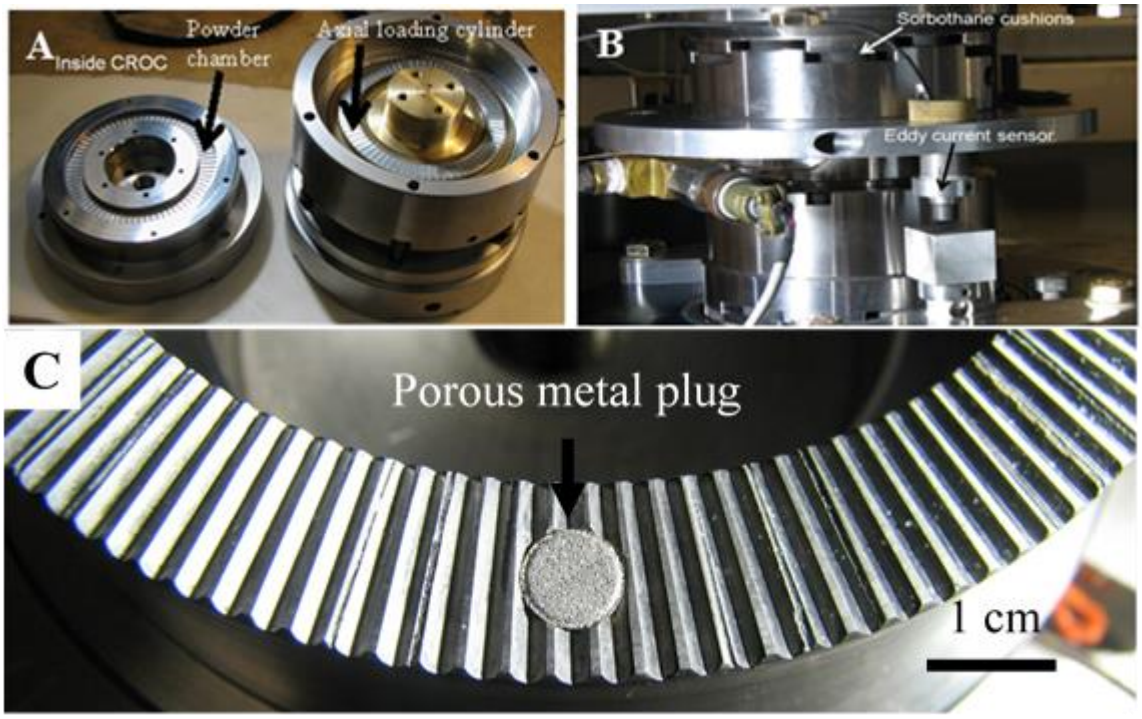

Figure 7. The confined rotary cell. A. CROC parts including a powder loading chamber and another loading cylinder before assembly. B. CROC been assembled and placed into the ROGA. C. Close-up view of the teeth design with the porous metal plug.

Friction experiments

Solid rock sample preparation

The two blocks of the solid rocks are cylindrical, with a diameter of 101.6 mm and ~50 mm height. The lower block is a solid cylinder while the upper block has a raised ring structure with inner diameter of ~63.2 mm and outer diameter of 82.3 mm. The two

rock blocks were pressed against each other along the raised ring, with the velocity at the outside of the ring 14% higher than the inside. Continuous wear of the rocks during multiple runs enlarged the ring size by both reducing the inner ring diameter and increasing the outer ring diameter.

The rock blocks were glued into the aluminum holders with epoxy. The rocks were then placed in a wheel grinding machine to flat the surfaces. A finer polishing with #600 SiC grit on the glass plate by hand was then applied. To place the thermocouple wires, we drilled the holes in the upper block typically ~3 mm away from contact and cement thermocouple wire into the holes. A final 24-hour oven drying procedure at 100℃ was applied.

Powder sample preparation

Depending on the grain size chosen to start, the powder was roughly fractured with grain size as large as a few mm or sieved with <150 μm or 150~250 μm. The powder was loaded into the CROC cell typically as a ~3 mm thick layer, gently compacted, and ~15 gram in weight. Wet samples were mixed and weighed before loading into the CROC cell.

Friction experiment procedure

In the velocity-control mode, the slip velocity history was designated by the control file. Typical velocity-control modes are constant velocity, slide-hold-slide, stepping velocity (stepping up or stepping down), and ramp velocity (linear increase/decrease velocity). In the power-control mode, the power density, which is the product of shear stress and slip velocity, was controlled (usually at a constant value) for a given experiment.

The high speed shear experiments can run under either velocity-control or power-control modes. Velocity range is 0.001-1 m/s. The normal stress, σ_n, was kept constant during a given experiment. In a typical experiment the sample was placed into ROGA, loaded at the selected normal stress, with the sensors connected. The run experimental history is built into a control file in the ROGA1.0 dedicated program (Fig. 6B) which automatically runs the experiment, while recording the following variables: normal force, shear force, vertical displacement normal to the fault, sample temperature, and rate of sample rotation. These parameters were measured at rates between 20-5,000 samples per second, depending on the type of the experiment. The recorded experimental data were first converted to relevant mechanical data (stresses, displacements and slip-velocity) in the dedicated MatLab program, and the final plots and inspections were done with the PSI analytical program.

Microscopic analysis

Sample collection

Most of the microscopic analyses were conducted on the shear products collected after the run. Due to physical limitations, the typical collected samples were a few mm to 1-2 cm in size (Fig. 8), while attempting to preserve the shear-zone structure. Fault surfaces pieces were collected directly after opening the two blocks. Gouge and cohesive gouge flakes were easy to collect, but care was required due to their fragile nature. Broken pieces of the experimental fault zone were collected for cross-sectional view. The fault-zone of powder runs were preserved with a low viscosity epoxy under vacuum before cutting into cross-sections.

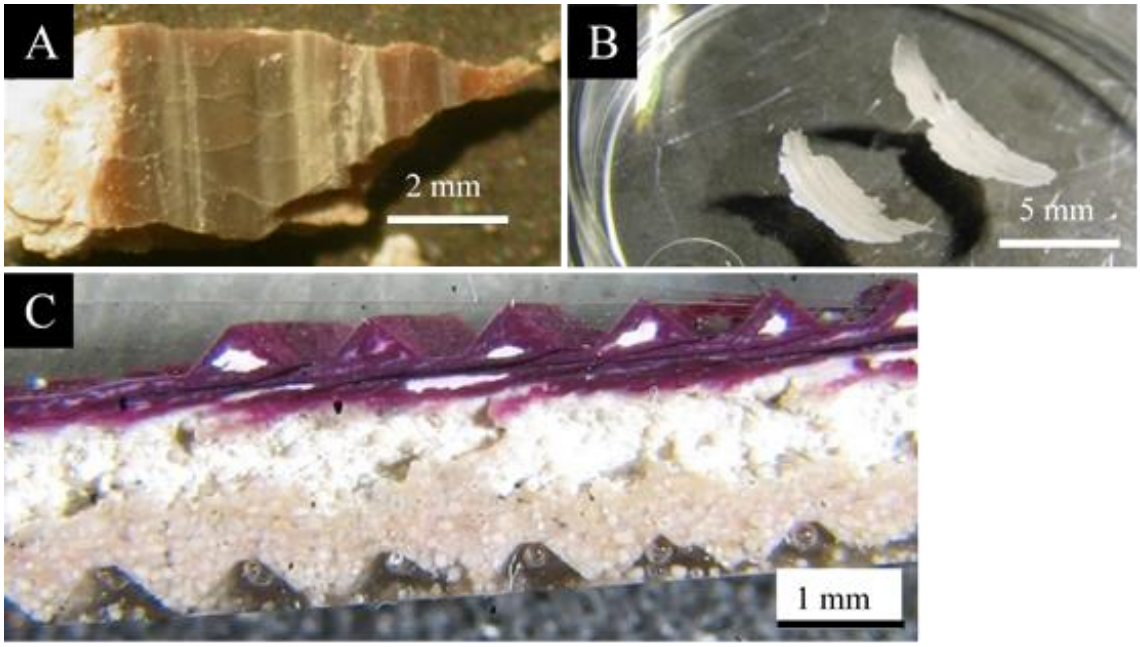

Figure 8. Example of collected samples. A. A piece of hard crust knocked off from the friction experiment of Kasota Dolomite. Note the color variations, fracture patterns, and striations on the fault surface. B. Two pieces of gouge flakes in the petri dish collected from the radiant red granite friction experiments. Note the curvy, shining, and striated top surfaces. C. Cross sectional view of the CROC experiment run with ooid grains after epoxy treatment and polishing. The red color was due to the doping of a chemical heat indicator which turned to red when temperature reached ~200℃. Note the preservation of teeth on top and bottom, principal slip surface near top wall, fractured grains in the middle, and visible ooid grains in the lower part.

Analysis techniques

Atomic Force Microscopy

Atomic Force Microscope (AFM) is a powerful tool for subtle force measurements and surface mapping at the micron to atomic-scales. The basic principles of AFM are schematically shown in Fig. 9. A laser was directed to the top of the cantilever and reflected toward the center of a 4-quardrant photodiode detector. Tiny interactions between the AFM probe tip and sample surface cause deflection of the cantilever and

result in the deviation of the laser beam from the center of the photodiode detector, causing change of the photo-voltage signal output.

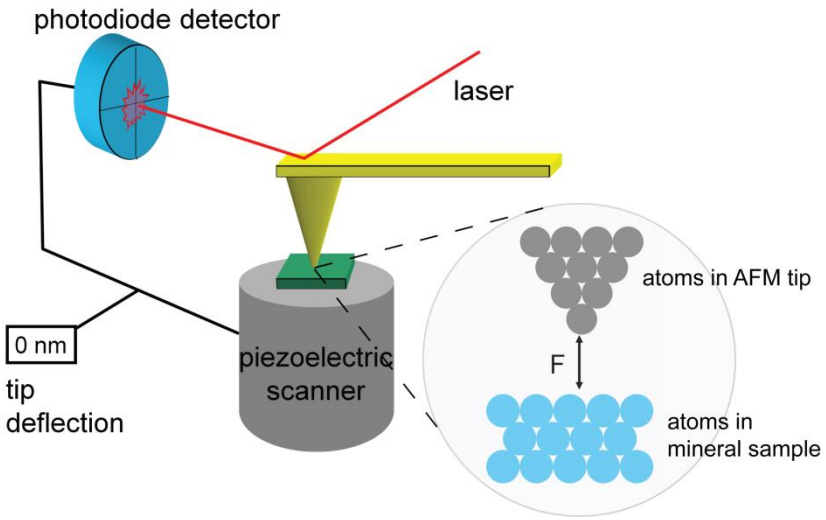

Figure 9. A schematic illustration of the AFM working principles. The interaction between tip and sample surface was tracked by monitoring the position change of a laser beam spot which was reflected from the back of cantilever top. 3D Scanning was achieved by controlling the piezoelectric scanner. (From Madden, et al., Welcome to Nanoscience.)

Topographic map measurement (imaging) is performed by scanning the AFM probe tip across the area to record tip-to-sample distances at each point (x, y, z). AFM imaging requires the AFM probe tip to be as sharp as possible to optimize resolution. The AFM used in this study for topographic mapping is the Pacific Nano R2 AFM, and the probe used for imaging has a sharp tip with radius of curvature 10~100 nm mounted on the end of a flexible cantilever. Topographic height resolution of less than 1 nm, and cantilever force resolution of less than 1 nN can be obtained. For force measurements, the elastic spring constant of the flexible cantilever should be calibrated, which is a tedious and complicated process.

It should be noted that AFM imaging cannot be used rough surfaces with features greater than a few microns in relief. Also, imaging of moveable particles is challenging since the sweeping of the AFM tip across the sample can potentially move the particles away, or adhere particles onto the tip.

Well-developed AFM friction measurement methods include the lateral method (Meyer and Amer, 1990) and the axial colloidal probe method (Stiernstedt, et al., 2005). In the lateral method (Fig. 10A), the AFM tip in contact with sample surface slides in the direction normal to the cantilever arm, resulting in torsional deflection of the cantilever. The frictional force is proportional to the torsional displacement of the cantilever and the photodetector lateral signal (with the proportionality constant called lateral spring constant). The normal force is proportional to the vertical bending of the cantilever arm and is recorded by the non-zero output from the photodetector V_{up}-V_{down} signal (with the proportionality constant called normal spring constant). In the lateral method, both the normal and lateral force constants of the cantilever need to be calibrated in order to transfer the measured signal (in Volts) to forces (in Newtons). The axial friction measurement method relies on the interaction between a colloidal probe and sample surfaces through the measurement of force-distance curves (a process with approaching/retraction of the AFM probe with respect to sample surface, resulting the cantilever deflection with respect to height). Because of the change of direction of the frictional forces from tip from approach to retraction, the cantilever deflection will be different, and hence the hysteresis in the measured deflection signal between tip approach and retraction (Fig. 10B). The friction coefficient is extracted directly from the slopes of the hysteresis force-distance curves.

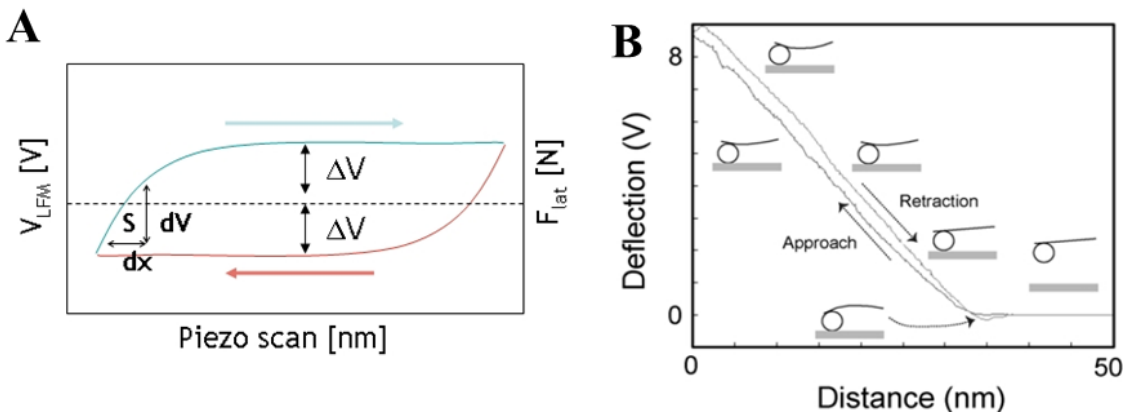

Figure 10. Basic AFM friction measurement methods. A. The so-called friction loop collected in an AFM lateral method, in which the tip slides laterally against the sample surface in a back-and forth cycle. Note the original signal of lateral cantilever deflection in Volts. B. Representative force-distance curve with hysteresis collected using the AFM axial method. The interaction between the colloidal probe and sample surface was illustrated in an exaggerated form (from Kosoglu et al., 2010).

The AFM axial method (Stiernstedt, et al., 2005) for friction analysis has several significant advantages including (1) small contact area (radius of contact ~0.2 μm) allows measurement of friction anisotropy in a controlled fashion, (2) samples are small (< 1 cm^2) with practically no restrictions on properties and characteristics, (3) friction can be measured under dry or wet conditions, and (4) no need for calibration of cantilever spring constant in order to determine the friction coefficient.

XRD

The XRD analysis were done with Rigaku X-ray powder diffractometer equipped with a fully-automated software system at the University of Oklahoma. For mineralogical analyses, procedures included powdering (fracture, micronizing mill), mounting (dry or wet), scanning, and analysis. Default scanning settings are 5-70° for 2θ ranges, 0.02° step size and 2 seconds per step. The analysis software was MDI Jade

2010 interfaced with International Centre for Diffraction Data PDF-2 and PDF-4+ databases, along with the MDI-minerals database.

SEM

Ultra-microstructure observations were made with Zeiss Neon 40 SEM/FIB at the University of Oklahoma. It has a dual beam system with both SEM and focused Ion beam (FIB) capabilities, field emission electron source with 0.1-30 kV accelerating voltage, 20 to 900,000 times magnification, and 1.1 nm resolution. Both secondary and backscattered electron images can be obtained with multiple detector settings, and the X-ray system allows energy dispersive spectrum (EDS) elemental analysis.

In order to run high resolution SEM, the samples were treated by: (1) mounting with super glue and silver paste instead of carbon tape to eliminate image drift during high resolution imaging, and (2) coating with the Au-Pd conductive layer as thin as possible (preserve raw topographic features) while make sure good conductivity (inhibit charging).

EPMA

EPMA analysis was performed with a Cameca SX50 system at the University of Oklahoma. The large beam currents of EPMA allow better contrast in backscattered electron images, and quantified elemental analysis with the wavelength dispersive detectors. Sample surfaces were polished as smooth as possible to eliminate surface effects for quantitative compositional analysis.

Chapter 3: Effect of roughness on friction

Slip during large earthquakes occurs along faults that are hundreds of kilometers long (e.g., San Andreas fault, Alpine fault), yet, the dynamic weakening that drives these earthquakes is controlled by nano- to micro- scale frictional processes (e.g., flash heating (Rice, 2006), gouge lubrication (Reches and Lockner, 2010), asperity deformation (Dieterich and Kilgore, 1994)). We analyzed these processes along experimental faults that slipped at rates approaching seismic velocity and which displayed intense dynamic weakening of 50%–70%. Sheared fault surfaces were extracted, and then Atomic Force Microscopy (AFM) was used to (1) measure friction on sub-micron scale, and (2) determine the three-dimensional morphology at the nano- to micro- scale. The sheared surfaces developed a prevalent anisotropy with a weaker and smoother axis along the slip direction. The nanoscale friction coefficient correlates well with sheared surface roughness: the friction coefficients dropped only on surfaces with RMS values of < 100 nm while rougher surfaces showed no weakening. Our analysis indicates that slip-smoothing at high slip-velocities can be an effective mechanism of dynamic weakening.

Introduction

Rock friction, which has profound effects on faulting processes and earthquake instability, was studied in numerous experiments (Tullis, 1996; Byerlee, 1978; Scholz, 1998). However, the typical experimental analyses suffer from a major inconsistency. On one hand, the rock friction is commonly determined through measurements on relatively large rock samples with areas from a few cm2 to 1 m2 (Byerlee, 1978; Lockner and Okubo, 1983), but on the other hand, theoretical models of frictional

processes are scale-dependent (Li and Kim, 2008), and active at small-scales of a few microns or less (Carpick et al., 1996; Mo et al., 2009; Li et al., 2011). Small-scale friction processes include asperity failure and deformation (Byerlee, 1967; Dieterich and Kilgore, 1994), gouge lubrication (Reches and Lockner, 2010), shearing of clays (Moore and Rymer, 2007), melting (Tsutsumi and Shimamoto, 1997), and flash heating (Goldsby and Tullis, 2011). In the present study, we eliminate this inconsistency by direct friction analysis from nano- to macro- scales.

We conducted rock friction experiments on experimental fault surfaces that were sheared at high slip velocity up to 0.9 m/s (~seismic slip velocity) under normal stress up to 7.0 MPa (Reches and Lockner, 2010). We used AFM and Scanning Electron Microscopy (SEM) to determine the frictional strength and roughness of the fault surfaces, and link these results to the macroscopic experimental observations.

Methods and materials

We measured the friction coefficient on experimental faults made of Sierra White granite (SWG) and Kasota dolomite (KD). The experimental faults were sheared by a rotary apparatus, in which two rock blocks with a ring-shaped contact slipped with respect to each othe r (Reches and Lockner, 2010). The sheared fault surfaces displayed slickenside striations parallel to the slip direction that resemble the well-known striations along natural faults (Fig. 11). Parts of the fault surfaces developed light-reflective, hard coating (Fig. 11B) similar to previous observations (Han et al., 2007a-b; Smith et al., 2012).

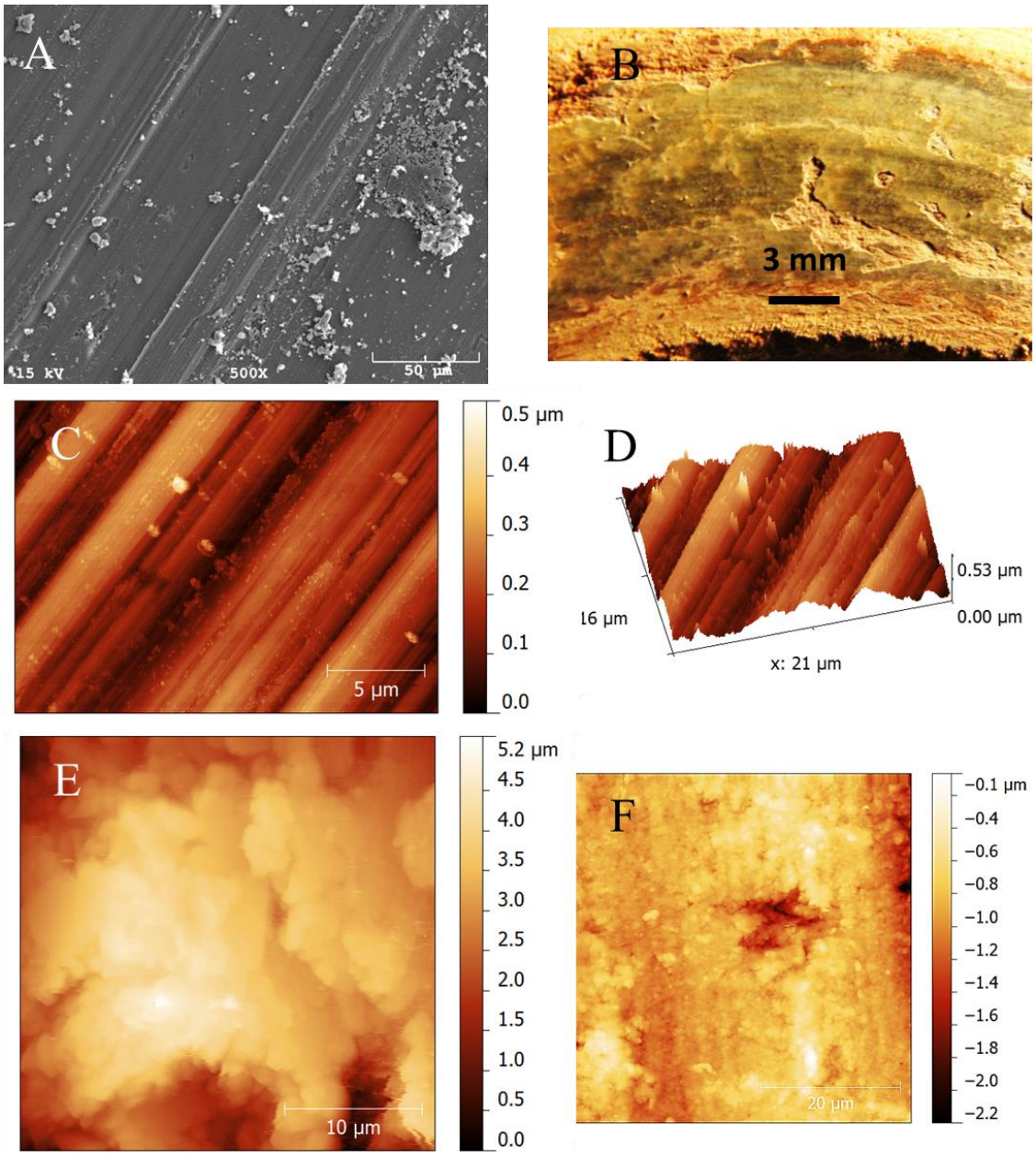

Figure 11. Fault surfaces. A. Scanning Electron Microscopy (SEM) image of an experimental fault of Kasota dolomite. B. The experimental fault surface of Kasota dolomite after run 1516 of the present study. C. Atomic Force Microscopy (AFM) image of sheared surface of Kasota dolomite (run 1516); note the distinct, clear striations at sub-micron spacing and a few fine grains (elevated bright spots). D. 3D view of C. E. AFM morphology map of un-sheared Kasota dolomite surface; note irregular, rough surface. F. AFM image of sheared surface of Sierra White granite; note the faint slickenside striations in general N-S direction, fine grains and damage (hole in the center).

We used two modes of AFM operation. The micron-scale morphology of the fault surfaces was measured in the intermittent contact mode that utilizes a sharp probe mounted on the end of a flexible cantilever (Maurice and Lower, 2008). The friction coefficient (FC), μ = [shear force/normal force], was measured by using the axial method (Stiernstedt et al., 2005; Attard et al., 2007; Kosoglu et al., 2010) in which a spherical silica glass bead (10s of microns in diameter) replaces the sharp tip on the cantilever (Fig. 16A). The FC is calculated from the hysteresis between the deflection of the cantilever while the probe, in contact with the sample, is advanced and retracted along the surface (Supplementary information). The axial method provides friction data for length scales of 0.1–0.25 μm, and allows for many measurements at the same spot under dry or wet conditions. This method yielded FC values in good agreement with macroscopic friction measurements for Na-montmorillonite samples (Kosoglu et al., 2010).

The FC was measured with AFM by aligning the cantilever's long axis either parallel or normal to the slickenside striations. We measured FC at 43 sites on our samples, and the measurement was repeated hundreds of times at each site (Table 1). The average standard deviation in the FC measurements at each site was $\pm$10.4%. Thirty-three of these sites were measured under air and 10 sites were measured under deionized water.

Results

Friction coefficient

We present here the FC data for the SWG and the KD samples; cleaved biotite results are presented in the Supplementary information. The AFM samples were collected from fault surfaces of SWG run 1614 (Fig. 15A), and from KD run 1516 (Fig.

12B). The FC values vary systematically with orientation and conditions (Fig. 12A) (Tables 1 and 2). Under room-dry conditions, the un-sheared surfaces have $\mu = 0.64 \pm 0.05$ for both rock types. On the dolomite surface, the FC slightly dropped to $\mu = 0.60 \pm 0.15$ normal to the slickensides. On granite fault surface, the friction increased to $\mu = 0.71 \pm 0.02$ on a rough, sheared surface. The most profound friction decrease was observed parallel to the slickensides: the FC dropped to $\mu = 0.34 \pm 0.08$ and $\mu = 0.52 \pm 0.03$, for dolomite and granite, respectively. Under wet (water covered) conditions parallel to slickensides, the friction dropped even further to $\mu = 0.15 \pm 0.05$ (dolomite) and $\mu = 0.31 \pm 0.05$ (granite).

The above nanoscale FC is comparable to the macroscopic FC for the host experiments. The AFM-analyzed dolomite surface is from run KD-1516 with stepping slip velocity up to 0.37 m/s, and slip distance of 7.9 m (Figs. 12B). The FC decreased systematically with velocity increase, and reached $\mu = 0.37 \pm 0.02$ at the final stage (Fig. 12B); this FC is almost identical to the AFM $\mu = 0.34 \pm 0.08$ that was measured room-dry, and slickenside-parallel on the same fault (Fig. 12A). This result was initially puzzling: the glass-bead appears as an ideal single-asperity, and single-asperity friction is expected to differ from the multi-asperity, Coulomb friction (Byerlee, 1978; Li and Kim, 2008). However, the AFM profile of the glass-bead (Fig. 16B) reveals roughness of 26.7 nm, such that it should be considered a multi-asperity body. Thus, the friction measurements with a multi-asperity glass-bead may be considered equivalent to the macroscopic friction, as actually observed (Fig. 12A).

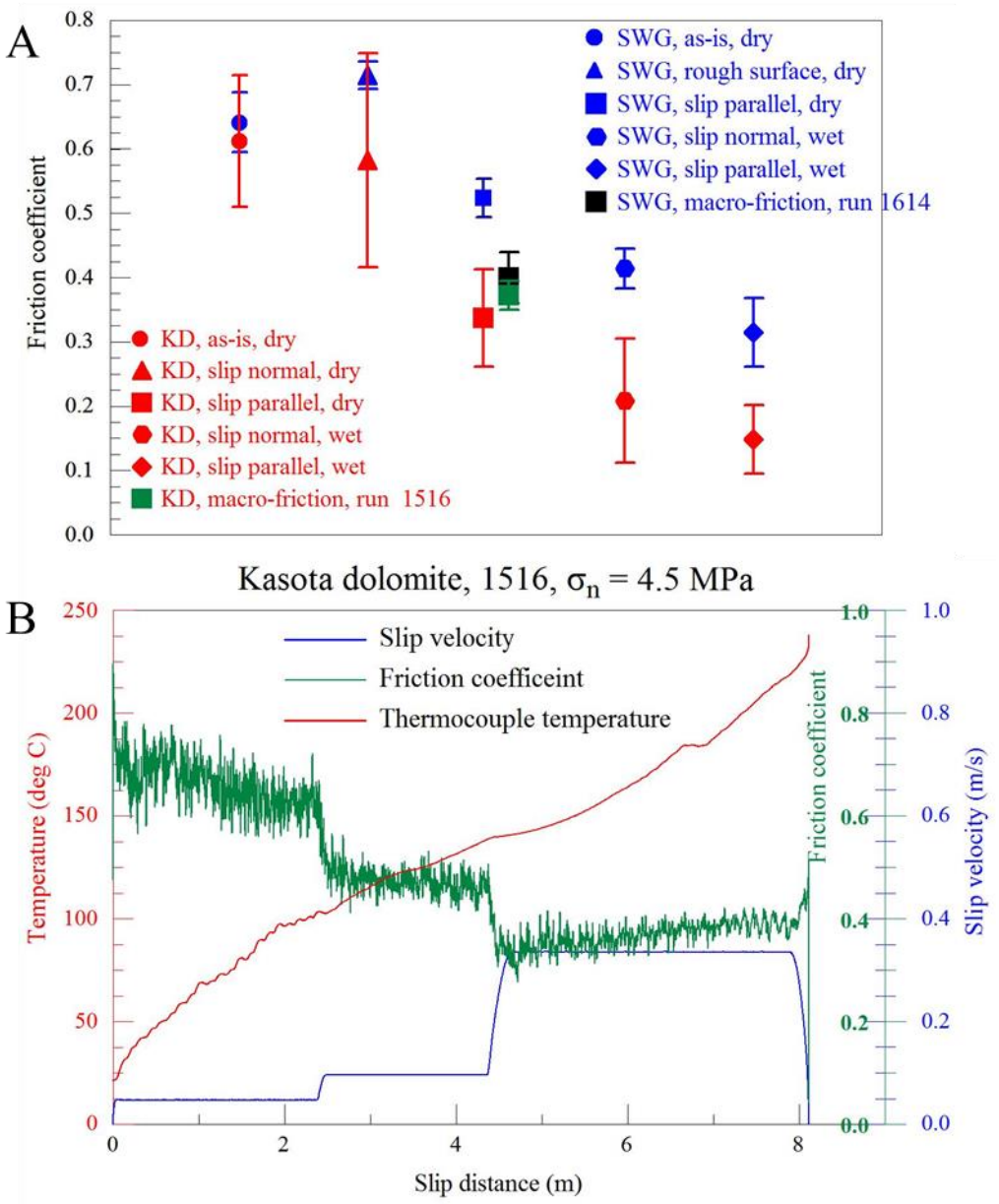

Figure 12. A. The sub-micron friction coefficients (FC) determined with the AFM glass-bead method on experimental fault surfaces of Kasota dolomite (KD) (run 1516) and Sierra White granite (SWG) (run 1614), and the macroscopic FC in the final stage of these experiments. Horizontal axis is arbitrary; each symbol indicates tens to hundreds of repetitions with standard deviation error bar. Note the FC variations with orientations (normal and parallel to slickensides) and conditions (room-dry and wet). B. History of the FC (green), slip velocity (blue), and thermocouple temperature plotted with respect to distance (experiment 1516).

Fault surface roughness

We measured the nanoscale morphology of the experimental faults in typical AFM imaging mode with a sharp tip probe (Fig. 11C-F). Un-sheared dolomite surfaces showed irregular, rough topography (Fig. 11E). The dolomite fault surfaces that were sheared at high velocity are relatively uniform (Fig. 11B) with prevailing slickenside striations spaced a fraction of a micron (Figs. 11C, D). The granite fault surface displays a heterogeneous range of textures. Parts of it are rough with deep holes and plowing traces, other parts are weakly striated (Fig. 11F), or even locally melted. This heterogeneity of the granite surface prevented simple extrapolation of the small-scale AFM measurements to the behavior of the entire macroscopic fault. Thus, the analysis below of friction-roughness relationships focuses on the Kasota dolomite observations.

We measured tens of AFM profiles across the four types of surfaces: cleaved biotite, un-sheared dolomite, and parallel- and normal-to-slickenside striations of the dolomite fault. The roughness of these surfaces can be presented by Power Spectral Density (PSD) (Power and Tullis, 1991), Ra (= mean height differences from a center line), or RMS roughness (= standard deviation of the height differences) (Power and Tullis, 1991). The PSD curves of our data (Fig. 13A) display a clear and expected trend: the cleaved biotite is the smoothest surface, the un-sheared surface is the roughest, and the profiles of parallel-and normal-to striations fall between the two end members.

We further noted systematic changes of the PSD slope, β. The un-sheared profiles have steep PSD curves, with $\beta = 2.3 \pm 0.1$. Profiles measured normal to the striations are smoother, with similar $\beta = 2.4 \pm 0.1$, and profiles measured parallel to the striations are even smoother and with lower $\beta = 1.4 \pm 0.4$. Similar roughness anisotropy between

slip-parallel and slip-normal on fault surfaces were observed by Power et al. (1987), Sagy et al. (2007), Renard et al. (2006), and Candela et al. (2011). The reduction of the un-sheared, original slope $\beta > 2$, to $\beta < 2$ (1.4 ± 0.4 in our case) parallel to the slip direction was previously documented in profilometer measurements of fault surfaces with tens to hundreds meters of slip (Sagy et al., 2007).

In addition to the above PSD curves, we calculated the RMS roughness along hundreds of 1 μm segments both slip-parallel and slip-normal. These 'micron-scale-RMS' values were calculated for 1 μm segments that are close in size to the AFM friction measurements size (0.1–0.25 μm). This scale of roughness calculations was selected because the parameters of Ra or RMS depend on the measurement area (larger areas yield larger Ra and RMS), and thus are valid at the measurement scale. We use the Ra and RMS results in the discussion below.

Friction-velocity relations

The above AFM measurements, which were conducted on a few selected fault surfaces, fit the macroscopic observations of extensive experimental efforts (e.g., Reches and Lockner, 2010; Green et al. 2010; Boneh, 2012; Chang et al., 2012). Figure 14 displays the friction-velocity relations in 81 experiments with Kasota dolomite that slipped under constant or stepped velocity (Boneh, 2012). The figure reveals a consistent trend: steady $\mu = 0.8–0.9$ up to a critical velocity of $V_C \sim 0.08$ m/s, and a rapid drop to $\mu \sim 0.3$ as the velocity approaches 1 m/s. The surfaces of Kasota dolomite that were analyzed here (Fig. 11–13) fit well this trend (blue square, Fig. 14).

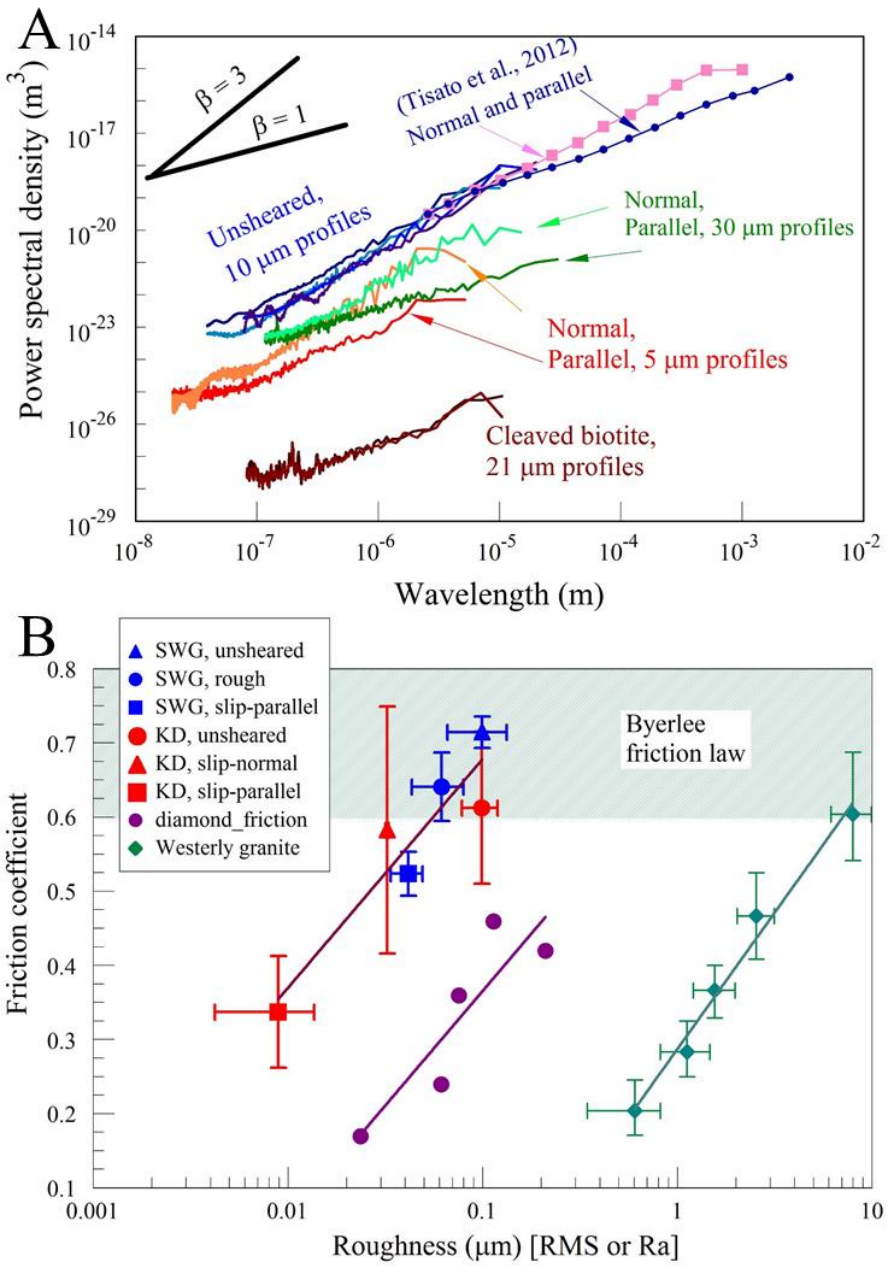

Figure 13 A. Power-spectral-density (PSD) of surface roughness of the marked surfaces. The PSD data of the present work were calculated for tens of AFM profiles of the marked length. Note the two end member of cleaved biotite (smoothest) and un-sheared surface (roughest), and the roughness difference between striation-parallel and striation-normal roughness. B. roughness-friction relations at micron scale. Shown: room-dry FC and the AFM roughness of Kasota dolomite and Sierra White granite surfaces (roughness as RMS for 1 μm segments), diamond sample A (Hayward et al., 1992), and Westerly granite (Byerlee, 1967) (roughness as Ra). The relations have the form (solid line): FC=a ln(roughness) + b, where (a, b) are (0.13, 0.99) for KD-SWG combined, (0.13, 0.67) for diamond A, and (0.16, 0.29) for Westerly granite.

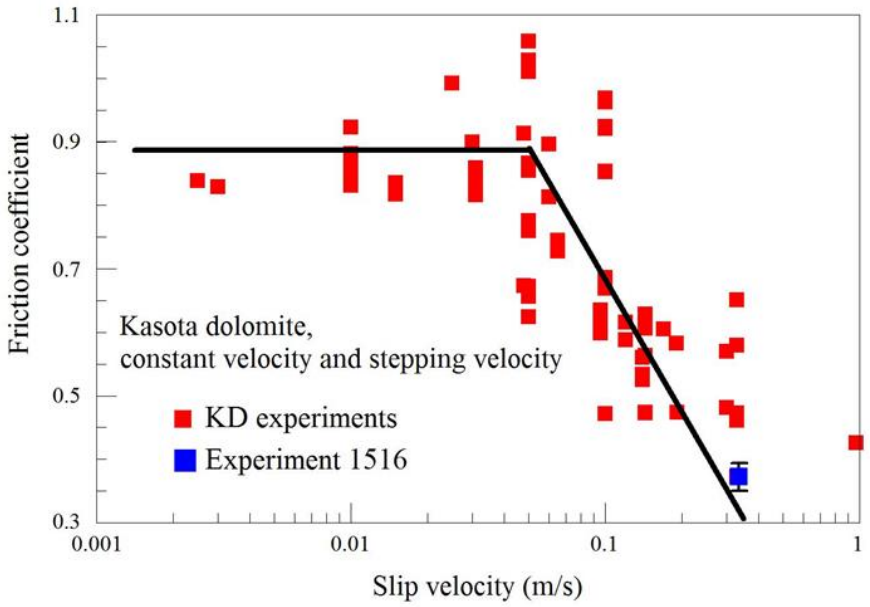

Figure 14. Macroscopic steady-state FC and slip velocity of Kasota dolomite. The plot includes 85 data points determined in constant velocity and stepping-velocity experiments (Boneh, 2012). Final FC of experiment 1516 (Fig. 12B) is marked by blue square.

A common feature in the dolomite experiments at velocities above V_C is that the fault surfaces were coated, partly or fully, with hard, smooth, light-reflective crust (Boneh, 2012; Boneh et al., 2013) that was used for the AFM measurements (Fig. 11A-D). Under velocities exceeding 0.3 m/s, the two fault surfaces were almost fully coated with this crust without gouge powder (Fig. 11B). The top of this hard crust is a layer ~100 nm thick composed of 10–30 nm diameter particles (Green et al., 2010) that are similar in size to the typical gouge grains observed in AFM imaging. Finally, during the high-speed experiments, in which the crust was formed, the average fault surface temperature exceeded 400 ℃ (calculated by finite-element modeling of the

thermocouple data). The contribution of these features to fault weakening is discussed below.

Discussion

The main observations of the experimental dolomite faults are: (1) intense dynamic weakening during high-velocity slip (Fig.12B, 14); (2) formation of a hard, shining surface (Fig. 11B); (3) the sub-micron friction is anisotropic with lower values parallel to slip striations (Fig. 12A); and (4) anisotropic roughness, with significantly smoother surface parallel to slip striations (Fig. 13A). These observations led us to a few inferences.

We first discuss the friction-roughness relations following previous observations which showed that smoother surfaces have lower frictional resistance (Byerlee, 1967; Hayward et al., 1992). The AFM friction coefficients in our analysis are plotted as function of the micron-scale-RMS (both friction and roughness measurements at similar scales, above) (Fig. 13B). We also plotted the equivalent relations for Westerly granite (Byerlee, 1967), and diamond (Hayward et al., 1992). These observations indicate that at length scales of 0.01–10 μm, friction coefficients strongly correlate with roughness RMS (or Ra) with correlation trends of the shape $\mu = a \cdot \ln(\text{RMS or Ra}) + b$ (Fig. 13B). For these rocks (KD, SWG and Westerly granite) the FC quickly approaches the range of 0.6–0.85 which is the "universal" FC for brittle fault surfaces independently of rock type, velocity, and temperature (Byerlee, 1978). We conclude from these relations that the friction reduction of faults is primarily controlled by smoothing (=roughness reduction) at scale of 0.01–10 μm, whereas the roughness at larger scales of natural faults has limited effect on the FC. Faults with sub-micron roughness are recognized in

the field by their “mirror-like”, light-reflecting surfaces (Siman-Tov et al., 2013), and our analysis suggests that such faults slipped under low frictional resistance.

We finally link the main features of high-velocity dolomite faults: they are coated with smooth, shiny crust (Fig. 11A-D, 13A) that is composed of ultra-fine grains of either decomposed carbonate oxide or recrystallized carbonate (Green et al., 2010; Siman-Tov et al., 2013), and which formed under high temperature (> 400 ℃). We envision that the heated, ultra-fine grains were soft enough to deform plastically, and to form the highly smooth surfaces (RMS < 100 nm for 1 μm profiles Fig. 13B) with low friction coefficient (Figs. 12, 14). As these processes occur only at high velocity ($V > V_C$ ~0.08 m/s, Fig. 14), we propose that slip-smoothing under high velocity can be an effective mechanism for dynamic weakening during earthquakes. The explicit slip-smoothing mechanism may vary depending on fault composition and slip conditions. For example, dynamic recrystallization (Smith et al., 2012) or asperity abrasion (Byerlee, 1967) facilitate fault surfaces smoothing and thus could lead to dynamic weakening.

Supplementary information

This section provides supporting information for this chapter “Dynamic weakening by nanoscale smoothing during high velocity fault slip”. The topics covered here are:

1. Modes of usage of the Atomic Force Microscope (AFM), focusing on measuring friction in the glass-bead method and the relevant calculations. The friction data in the paper were determined in this method.
2. The shear and normal stresses associated with the AFM friction measurements.

3. Data base including sample composition, details of AFM friction measurements, and the shear apparatus used for the experiments.
4. Nano-morphology methods and calculations of power-spectral-density (PSD) and surface roughness.

Rock friction experiments

Rock samples:

Sierra White granite. The electron-microprobe (EPMA) modal analysis shows six main minerals in this rock: plagioclase (48%), quartz (38%), alkali-feldspar (5%), ferromagnesian- mica (5%), and muscovite (5%). Mean grain size is about 0.3 mm; mean void space in EPMA images is ~4%.

Kasota dolomite. The Kasota dolomite were quarried at Mankato, Minnesota, and it is supplied under the commercial name "Kasota valley limestone". The XRD analysis indicates that our samples are 97.3% dolomite, 2.6% quartz and traces of plagioclase.

High velocity friction experiments:

The experiments were conducted on the ROGA system with bare, solid blocks of Sierra White granite and Kasota dolomite. Each sample includes two cylindrical blocks of 101.6 mm diameter and 50.8 mm height. The upper block has a raised ring structure with inner diameter of 63.2 mm and outer diameter of 82.3 mm.

The present experiments on the solid rock blocks were run at room-temperature and room humidity. They were run under controlled, stepped velocity, and the normal stress, σ_n, was kept constant during a given experiment. We used one sample of Sierra White granite, and one sample of Kasota dolomite, and the experimental results for SWG are shown here in Fig. 15.

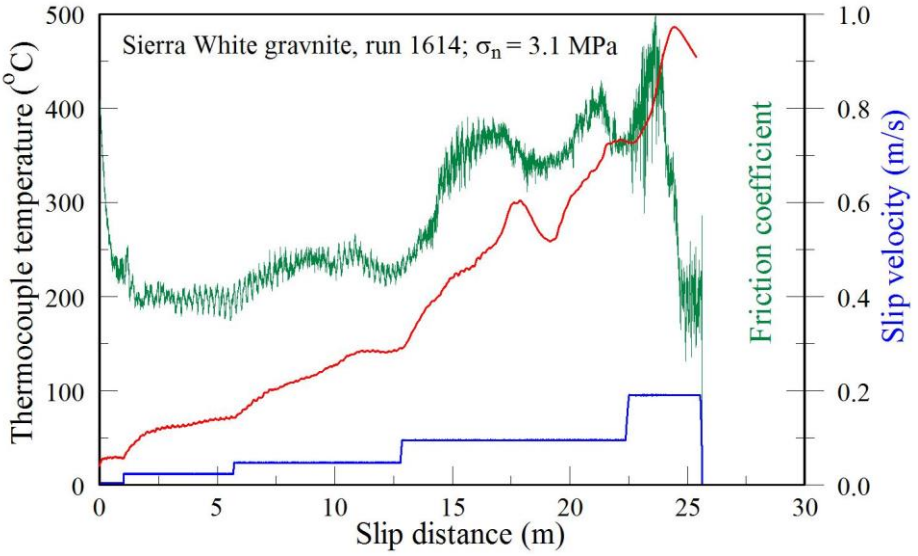

Figure 15. Velocity loading history and corresponding friction and temperature for Sierra White granite run 1614.

Atomic Force Microscope utilization

AFM modes

We used two modes of AFM operation. The micro/nanoscale topography of the fault surfaces was imaged with a *Pacific Nanotechnology Nano R2* AFM using the standard 'close contact' imaging mode (also called non-contact or tapping mode, depending on whether the tip penetrates the absorbed water layer). In this mode the cantilever oscillates at a frequency close to its resonant frequency while the tip interaction forces modify the cantilever oscillation frequency and hence its amplitude. This modification of the resonant frequency is combined with a feedback loop system that maintains a constant oscillation amplitude or frequency by adjusting the average tip-to-sample distance. The tip-to-sample distances are recorded at each point (x, y) to construct the topographic image.

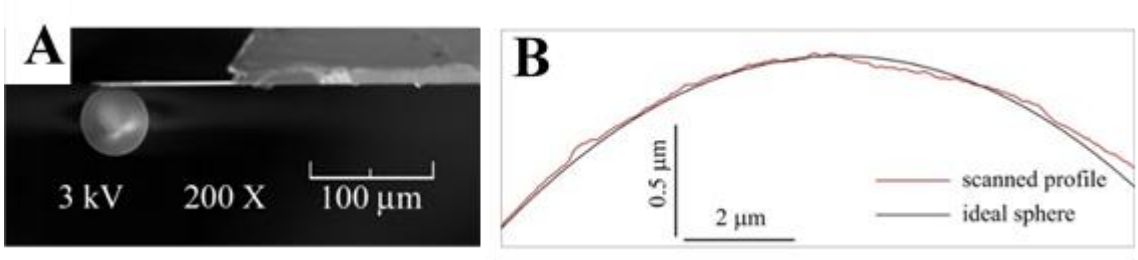

Figure 16. The AFM colloidal probe geometry. A. An SEM image of the fabricated glass-bead probe for our Nano R2 AFM platform. The glass-bead diameter is 50 µm and the cantilever length is 100 µm. B. 1D AFM profile of the glass-bead (red) compared to ideal sphere shape (black); note asperities and roughness at submicron scale.

For the measurement of the friction coefficient we closely followed a recently developed AFM method (Stiernstedt et al., 2005; Attard et al., 2007; Kosoglu et al., 2010) in which a spherical glass-bead (10s of microns diameter) replaces the sharp tip on the cantilever (Fig. 16). The cantilever with the glass-bead is moved vertically to approach and retract with respect to the sample surfaces (Fig. 17). The force-distance curves of the interaction forces during this motion are presented by the deflection voltage versus z-piezo displacement curves (Fig. 17), where deflection voltage records the displacement of a laser beam in a position-sensitive detector reflected from the back of the flexible cantilever. The deflection voltage is proportional to force, considering the cantilever spring constant. The cantilever with the glass-bead is inclined with respect to the sample surface (Fig. 17), and this inclination generates frictional slip at the contact area between the glass-bead and sample surface (red arrows in Fig. 17). The friction force inverses its sense during the shift from approaching to retraction according to the change of sliding between glass-bead and sample surface. This sense inversion of the frictional force changes the deflection of the cantilever since the torque applied on the cantilever changes. The result is a force-distance curve with hysteresis

between approaching and retracting lines (Fig. 17). The analysis of the slopes of the force-distance curves with hysteresis can be combined with geometric and mechanical parameters of the cantilever to calculate the friction coefficient as shown below and elsewhere (Stiernstedt et al., 2005).

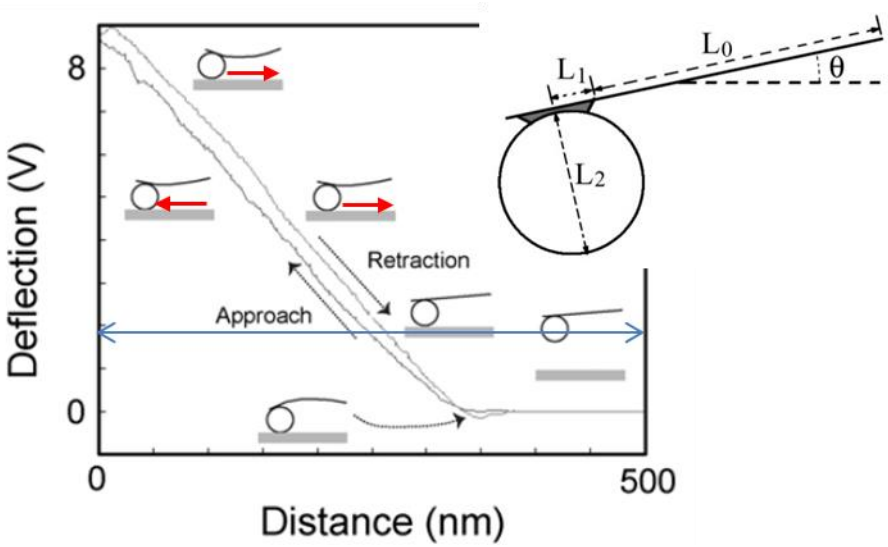

Figure 17. Schematic illustration of the interaction between glass bead and sample surface with respect to the force curve. Inset displays the cantilever geometric parameters needed for friction coefficient calculations (after Kosoglu et al., 2010)

Friction measurement procedure

Glass-bead probe fabrication

The glass-bead probe preparation is of central importance for successful friction measurements. We followed the procedure of Kosoglu et al (2010). To fabricate the probes, we used: (1) rectangular, tip-less silicon AFM cantilevers with aluminum backside coating from *Mikromasch*; (2) silicon oxide microspheres of ~50 micron diameter from *Microspheres-Nanospheres;* and (3) *Loctite* marine epoxy. The *Nano-R2* system has an optic microscope and x-y-z piezo controller, which make it excellent platform for assembling the microsphere onto the end of the cantilever.

Glass-beads were cleaned in de-ionized water and ultrasonically vibrated for a few minutes to remove potential adhesive particles. Then, glass-bead was dropped onto a clean mica surface and dried by heating the mica on a hotplate. The cantilever end was slowly moved down into a tiny drop of epoxy, gently raised up, placed above the glass bead, and then moved down into contact with the top of the glass-bead. Once contact was made, the cantilever with the glued glass-bead was slowly raised, and left undisturbed to cure for 24 hours.

During the fabrication process, glue contamination was avoided on the glass-bead and the backside of the cantilever. Glue contamination on the bead, especially the contact area, may lead to non-direct contact between the glass-bead and the sample surface, and contamination on the back side of the cantilever may lead to reduced optical reflective signal. The fabricated probe was imaged with a Scanning Electron Microscope (SEM) (Fig. 16) to determine the cantilever geometry for the friction coefficient calculations and to inspect the glue quality.

Force-distance curve analysis

The force-distance curves for the friction coefficient analysis were determined with a *Veeco Dimension 3100* AFM at Brigham Young University. Under the force-curve mode, this AFM can collect repeating force curve data automatically at the same spot, either in air or under solution that covers the sample and tip by a meniscus. The operator controls the ramp size (the z piezo movement distance) and repeating frequency that in turn controls the bead sliding velocity and the size of the contact region.

Prior to rock friction measurements, the fabricated probe was applied to fresh-cleaved biotite surfaces. The extracted friction coefficient was compared to reported values to ensure the accuracy of this method. The glass bead method yielded a friction coefficient of 0.27 ± 0.01 (Attard et al., 2007), 0.29 ± 0.03 (Attard et al., 2007), 0.29 ± 0.02 (Kosoglu et al., 2010) on wet mica as reported; and our friction coefficient is 0.27 ± 0.02, which agreed well with literature.

Before the rock friction measurement, the glass-bead probe and the rock surfaces were cleaned in a UV-Ozone cleaner for 20 min. The force-distance curve measurements were conducted either parallel or normal the slickensides striations by aligning the cantilever long axis in the selected direction. Once positioned, preliminary curves were obtained to observe the quality of the force-distance curves. A good curve has the following properties (Fig. 18): (1) zero line at large separation; (2) constant compliance line in the contact region (Attard et al., 2007); and (3) clear hysteresis between the approaching and retracting curves (Fig. 18). If these properties were satisfied, we then collected force curve data at that position with hundreds of repetitions.

Calculation of the friction coefficient

The detailed derivation of the friction coefficient calculation was presented by Stiernstedt et al., 2005. The required parameters are the probe geometry (including total length of the cantilever, length of the flexible part of the cantilever L_0, length of the glue spot L_1, diameter of the sphere L_2, and inclination angle of the cantilever θ) as well as the slopes of the most linear part of the compliance region from the force curve hysteresis (Fig. 18). In our case, the probe geometry parameters are cantilever total

length 130 μm, glue spot length 10 μm, cantilever flexible part length 100 μm, sphere diameter 50 μm, and cantilever inclination of 12° (Fig. 17 inset). Calculations were conducted with Matlab.

Friction coefficient data

Nano-friction measurements with the glass-bead method

We measure and calculated the friction coefficients in 18 positions in which we had 43 sites, and in each we had tens to hundreds of repeat measurements. Table 1 below summarizes the results for all this sites and Table 2 list the average friction coefficients according to rock type, orientation (parallel and normal to slickensides) and conditions (room-dry or wet). The data of Table 2 is used in Figs. 12 and 14 of the chapter.

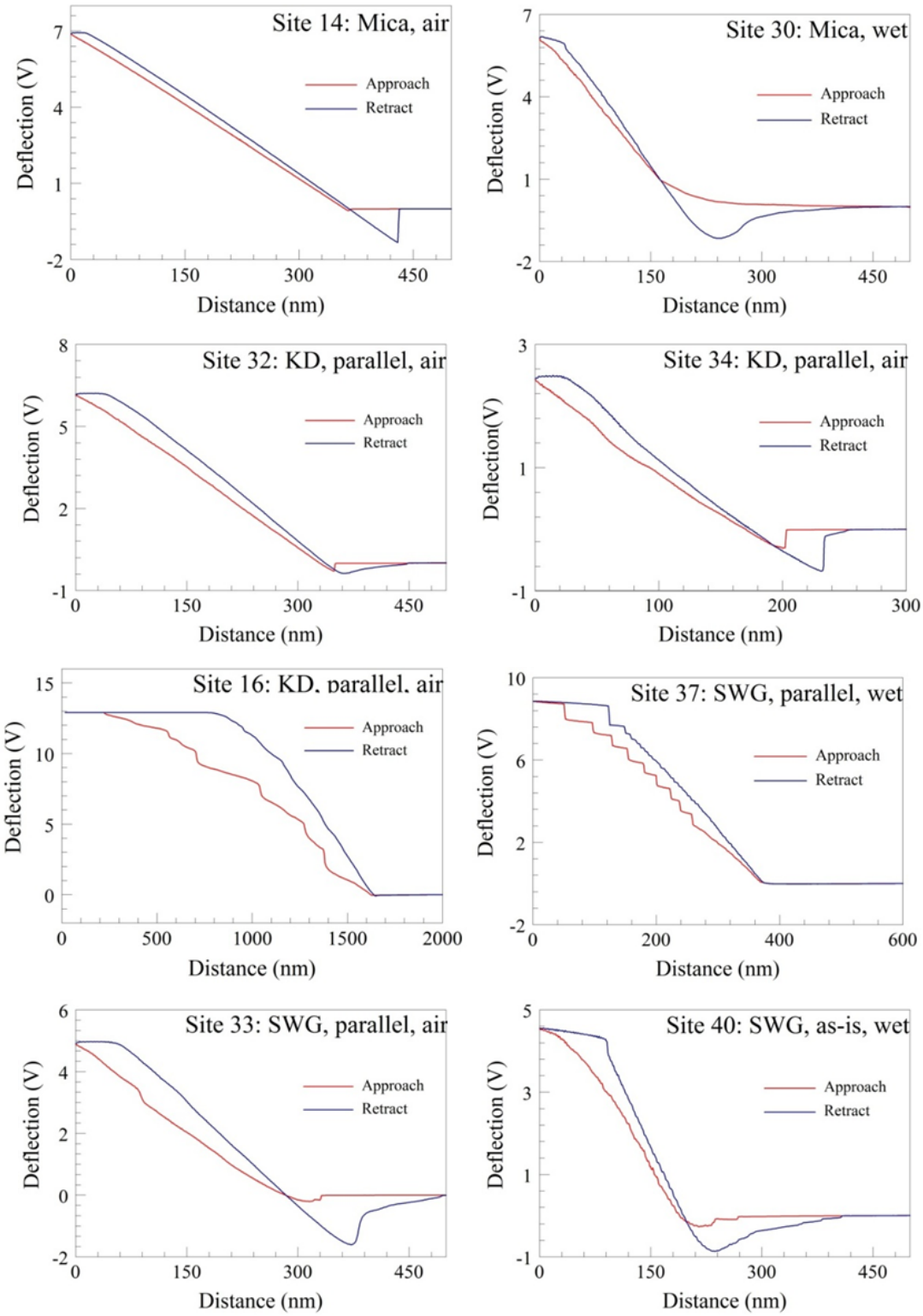

Figure 18. Representative force curves of the AFM friction measurement method.

Table 1 Summary of AFM friction measurements

Site #	Rock type	Surface orientation	Condition	Ramp (μm)	# of repeat	Friction coeff. (Mean ± Stdev)		Comments
						each data point	group of data points	
16	KD	parallel	room-dry	0.5 2 3	133 69 207	0.43 ± 0.096 0.63 ± 0.033 0.64 ± 0.041	0.34±0.17 (8)	Stick-slip? Stick-slip?
31	KD	parallel	room-dry	2	35	0.67 ± 0.051		low quality
32	KD	parallel	room-dry	0.5 1.5	38 35	0.364 ± 0.056 0.295 ± 0.013		
34	KD	parallel	room-dry	0.3	67	0.26 ± 0.043		
32-1	KD	parallel	wet	0.1 0.2 0.4 0.6	113 60 60 99	0.23 ± 0.035 0.17 ± 0.044 0.092 ± 0.05 0.13 ± 0.043	0.15±0.05 (5)	Unstable
34-1	KD	parallel	wet	0.3	76	0.12 ± 0.029		
36	KD	normal	wet	0.15 1	44 41	0.14 ± 0.035 0.277 ± 0.023	0.21±0.1 (2)	
19	KD	normal	room-dry	0.5 2	57 44	0.56 ± 0.018 0.67 ± 0.015	0.56±0.12 (5)	
20	KD	normal	room-dry	0.3 0.5 1.5	38 53 53	0.63 ± 0.01 0.571 ± 0.023 0.37 ± 0.024		Middle linear part Middle linear part Middle linear part
21	KD	As-is	room-dry	0.4 3	35 47	0.54 ± 0.121 0.685 ± 0.034	0.61±0.1 (2)	
33	SWG	parallel	room-dry	0.3 0.5	56 29	0.503 ± 0.022 0.545 ± 0.023	0.52±0.03 (2)	
37	SWG	parallel	wet	0.2 0.3 0.4 0.6 1 3	13 7 4 84 37 34	0.279 ± 0.033 0.3 ± 0.022 0.36 ± 0.026 0.338 ± 0.029 0.296 ± 0.021 0.43 ± 0.028	0.33±0.06 (6)	part of linear region part of linear region part of linear region Stick-slip? Stick-slip?
22	SWG	rough	room-dry	0.5 2	60 42	0.73 ± 0.003 0.7 ± 0.009	0.72±0.02 (2)	
23	SWG	As-is	room-dry	0.3 1 3 5	31 34 49 24	0.61 ± 0.016 0.62 ± 0.011 0.71 ± 0.037 0.625 ± 0.014	0.64±0.05 (4)	
40	SWG	As-is	wet	0.3 0.5 1	76 43 28	0.397 ± 0.03 0.45 ± 0.032 0.394 ± 0.018	0.41±0.03 (3)	
14	biotite	fresh-cleave	room-dry	0.5	102	0.15 ± 0.024	0.15±0.01 (2)	
15	biotite	fresh-cleave	room-dry	0.5	102	0.14 ± 0.008		
30	biotite	fresh-cleave	wet	0.4 0.5 1	33 39 44	0.26 ± 0.043 0.29 ± 0.037 0.26 ± 0.034	0.27±0.02 (3)	

Table 2 Friction coefficient results in AFM measurements

Test conditions	Rough	dry	NA		2	0.72±0.02	3	0.27±0.02 (wet)
	As-is	wet	NA		3	0.41±0.03		
		dry	2	0.61±0.1	4	0.64±0.05		
	Normal	wet	2	0.21±0.1	NA			
		dry	5	0.56±0.12	NA		2	0.15±0.01 (dry)
	Parallel	wet	5	0.15±0.05	6	0.33±0.06		
		dry	8	0.34±0.17	2	0.52±0.03		
Friction coeff. (Mean ± Stdev)			data points	μ	data points	μ	data points	μ
Rock type			KD		SWG		Biotite	

Loading stresses during AFM measurements

We apply the Hertz model (Hertz, 1881) to calculate the contact area and the stresses during the glass-bead friction measurements. The normal spring constant of the glass-bead probe was calibrated using the method by Sader et al. (1999) to find a spring constant of 6.5 N/m. The effective spring constant for the cantilever with glass-bead probe is 14.3 N/m by using the scaling factor $(L_{cal}/L_0)^3$ (Fig. 17 inset). Here L_{cal}=130 μm is the cantilever total length, and L_0=100 μm is the length of the flexible part of the cantilever). This value implies, that a cantilever normal force of 2 μN, the contact area is 0.02~0.07 μm^2 and the normal stress is on the order of a few tens of MPa.

From the cantilever deflection voltage versus z-piezo displacement curves, we extract normal force versus frictional force curves from the region corresponding to bead-sample contact using the equations in Stiernstedt et al., 2005. Separate linear fits describe the normal versus frictional force trends for the approach and retraction directions (Fig. 19). The slope of the linear fit line yields the coefficient of friction, in agreement with the calculated friction coefficient using colloidal probe method.

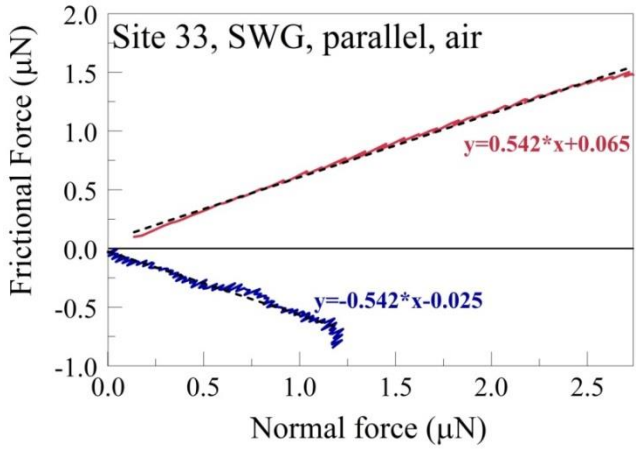

Figure 19. An example of normal and frictional force calculations following Stiernstedt et al. (2005). The plot displays the normal force vs. shear force for Site 33, SWG, parallel, room dry.

Since the linear fit line to the calculated normal force versus frictional force curves have non-zero intercepts due to adhesion forces which accounts for a significant portion of the total normal force applied at the surface, we shifted the fitted line to cross the zero point and in this way convert the normal force versus frictional force curves to normal stress versus shear stress curves shown in Fig. 20. The calculated normal and frictional forces are in tens to hundreds of nN, and the friction coefficient values are corresponds to the values we got using the axial glass bead method as described in the main text. Combining the forces with the contact area calculated from the Hertz model indicate that the normal and shear stress values can reach 50MPa in the present experiments. Stress magnitude here is comparable to crustal stress, raising the possibility to simulate friction process at depth.

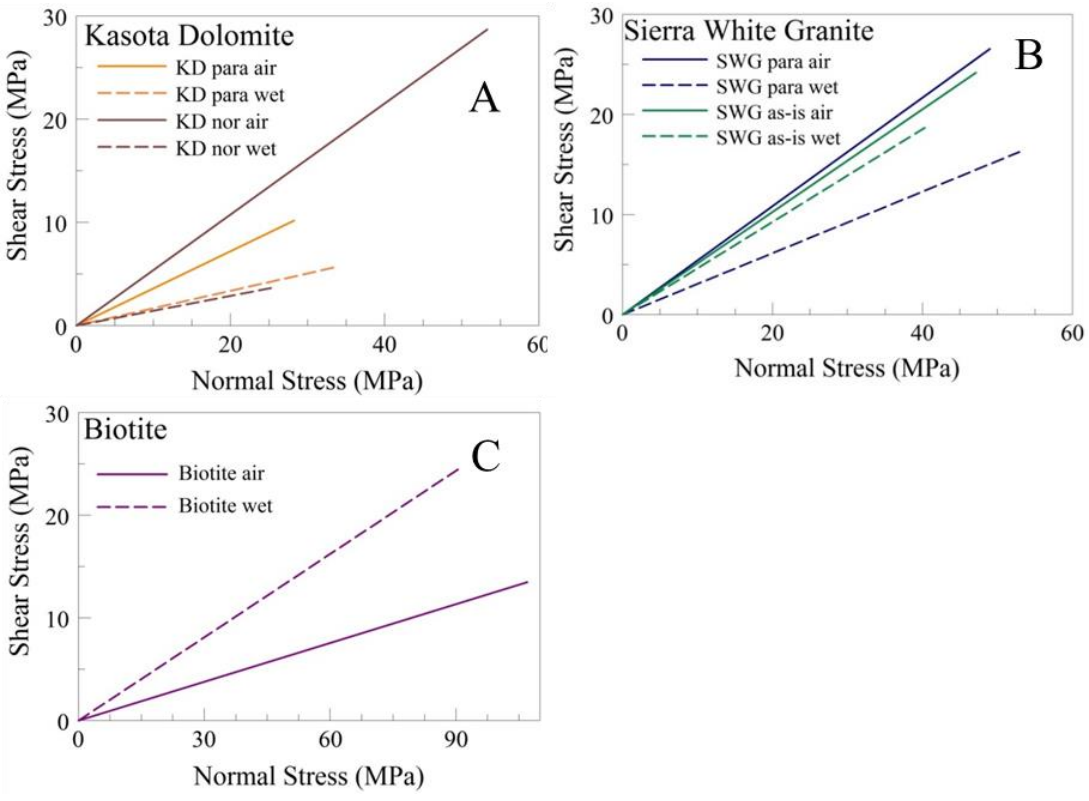

Figure 20. Calculated shear stress vs normal stress during AFM friction measurements for Kasota Dolomite (A), Sierra White Granite (B), and Biotite (C).

PSD and roughness calculations

The AFM topography of the fault surfaces was measured as described above, and some images are presented in Fig. 11. Here we present representative profiles across the fault surfaces (Fig. 21), and outline the calculations of the power spectral density (PSD). The PSD was calculated from profile data following the method of Sagy and Brodsky, 2009.

For each profile $y_i(x)$,

$$(PSD)_i = \frac{\mathcal{F}[y_i(x)]^2 \cdot L}{X^2}$$

where $\mathcal{F}[y_i(x)]$ is the fast Fourier transform of $y_i(x)$, L is the profile total length, and X is the total number of data points in the profile.

The PSD of the AFM fault surface images was calculated in the following procedure:

1. Extract the digital profile data by drawing lines across the AFM images using the dedicated AFM program *Gwyddion* (http://gwyddion.net/). One example of the extracted profiles was shown in Fig. 21A, with large amplitude and wavelength differences displayed between profiles parallel and normal to striations.
2. Each set of lines was either parallel- or normal- to the striation lines (Fig. 21A inset). In each image we selected 50 to 100 individual profiles all at the same length.
3. In *Matlab*, each profile was first leveled by applying the *detrend* command, and the PSD was calculated by using the above equation.

4. The final PSD of an image, for a given orientation is the average PSD of all 50-100 individual profiles. The final PSD curves are plotted in Fig. 13A.

One point should be noted with respect to error presentation in the PSD plot. The data points of the PSD are evenly spaced along the wavenumber ($k = 1/\lambda$) axis, and as the present PSD plot displays wavelength (λ) axis (Fig. 13A), the data points are denser in the shorter wavelength part.

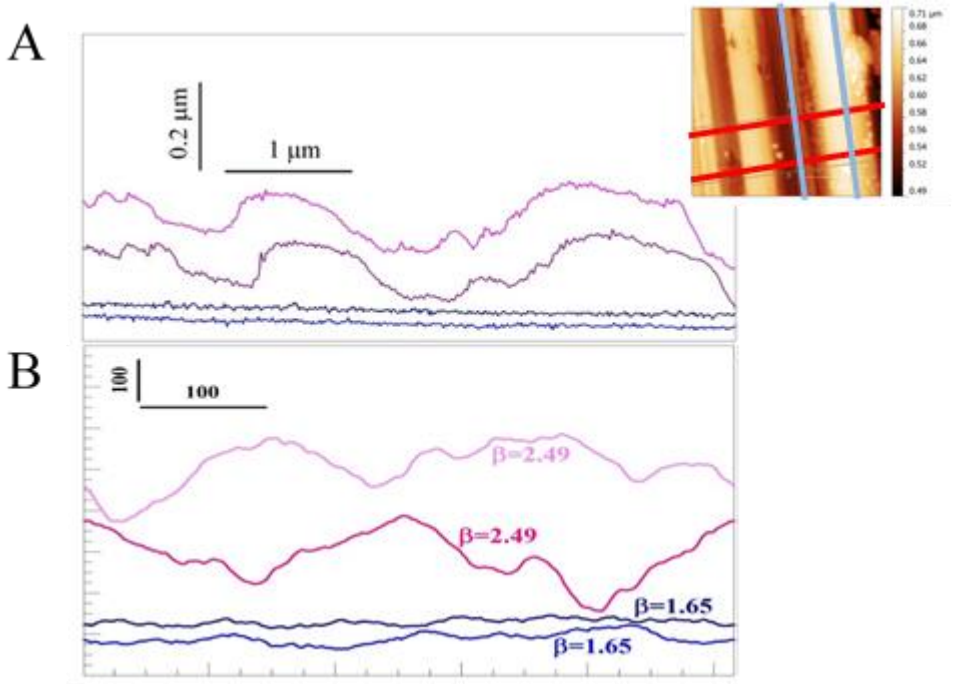

Figure 21. A: Examples of four 1D profiles across the KD fault surface on AFM image (inset). The two slip-parallel profiles (blue lines in inset) are significantly smoother than the slip-normal profiles (red line in inset). B: Synthetic profiles with the marked slope (β) in the PSD curve generated with MatLab.

For comparison, synthetic profiles with fixed slope for the PSD plots are also provided as shown in Fig. 21B. The values for the slopes of the most linear region of the PSD plots are chosen so that the synthetic profiles have the same PSD as the real profiles. Similar amplitude and wavelength characters can be seen fault surface and synthetic profiles.

Roughness values are extracted from the same profile data that we used to calculate the PSD based on their original definition of the roughness parameters. Here the root mean square (RMS) roughness R_q is calculated as the standard deviation of the height differences.

$$R_q = \sqrt{\frac{1}{n}\sum_{i=1}^{n}(y_i - \bar{y})^2}$$

Since roughness values are scale dependent[34], relationship between the RMS roughness and profile length can be calculated using Equation (2), by consider averaging the RMS roughness along each profile and the whole profile set data. In the paper, we picked the RMS roughness value at the profile length of 1 μm for KD, SWG, and the glass bead.

Chapter 4: Powder-rolling as a mechanism of dynamic fault weakening

For millennia, human-made machinery incorporated rolls and wheels to reduce frictional resistance, yet similar elements are practically absent in natural systems. We found in rock shear experiments that tiny, cylindrical rolls spontaneously develop along experimental faults and lead to drastic dynamic weakening. The experiments were conducted on granite samples with a rotary apparatus at slip velocity range of 0.001-1 m/s and normal stress up to 14.4 MPa. At moderate slip velocities of < 0.1 m/s, the fault slip localized along flakes of highly smooth surfaces that frequently displayed a multitude of cylindrical rolls. The rolls diameters are ~1 μm, their length range is 2-20 μm, and they are made of tightly-packed ultrafine (20-50 nm) powder grains. These rolls are systematically oriented normal to the slip direction. The presence of rolls correlates well with reduction of the macroscopic friction, and we propose that these powder rolls leads to a transition from sliding-dominated slip to rolling-dominated slip. It is expected that powder-rolling would be an effective mechanism of fault weakening.

Introduction

Dynamic fault weakening is a central controlling parameter of fault stability and seismic behavior. Thus, major experimental efforts were devoted to understand this weakening at a wide range of conditions, from seismic slip velocity of a few m/s, down to very low velocity of sub-micron per second (Dieterich, 1979; Di Toro et al., 2011; Reches and Lockner, 2010). Commonly, rock frictional strength is determined through macroscopic measurements on samples with slip surface area of a few cm^2 to 1 m^2 (Lockner and Okubo, 1983), and these measurements led to useful friction laws.

However, the macroscopic data cannot provide direct, physical evidence of the weakening mechanisms that are usually defined by micron-scale processes and can be revealed through microscopic analyses. We present here our high-resolution analysis of experimental fault surfaces that revealed micron scale powder rolls that developed spontaneously, converted the rock fault into natural roller-bearing, and weakened the fault.

Several weakening mechanisms were proposed during the last few decades, with only a few supported by direct, physical observations. For example, it was shown that time-dependent deformation of touching asperities controls the velocity-dependent and healing characteristics of planar faults slipped at very low velocity (Dieterich and Kilgore, 1994). Dynamic weakening is clearly associated with rock melting of experimental gabbro faults that slipped at high velocity ($V \geq 1$ m/s) for long distances (> 5 m) (Tsutsumi and Shimamoto, 1997; Niemeijer et al., 2011). Another example is fault lubrication by silica gel that forms along quartzitic faults during slip at moderate velocities (0.003-0.1 m/s) (Goldsby and Tullis, 2002; Di Toro et al., 2004). It was recently proposed that powder-lubrication within a fine-grain powder layer can lead to profound dynamic weakening (Reches and Lockner, 2010; Han et al., 2010). Powder-lubrication is an appealing mechanism because fine-grain rock powder, known as 'gouge', is found along almost all faults of the brittle crust regardless of fault composition (Ben-Zion and Sammis, 2003). Further, comminution into fine-grain gouge is the first process to occur experimentally along rocks of all compositions and at all slip-velocities (Boneh et al., 2013). It is further expected that as slip progresses, fine-grain powder with many sub-micron to nanoscale grains, would react and transform by

complicated physical and chemical processes. The activation of these processes, e.g., amorphization, dehydration, decomposition, melting or sintering, depends on slip conditions (normal stress, velocity, temperature) and fault composition. For example, silica-gel lubrication occurs at sub-seismic slip velocities of ~0.003 – 0.1 m/s only along siliceous rocks (Di Toro et al., 2004; Hayashi and Tsutsumi, 2010). Fault smoothing to mirror-like surfaces made of nanograins occurs primarily along carbonate faults at seismic slip velocities (> 0.05 m/s) (Chen et al., 2013; Siman-Tov et al., 2013). The present analysis focuses on one such process, the formation of powder-rolls, that appears as effective dynamic weakening mechanism.

Our rock friction experiments revealed two central features: First, the fault-slip was localized within a thin zone of the gouge layer, in agreement with many field and experimental observations (Reches and Lockner, 2010; Di Toro et al., 2004; Han et al., 2010; Ben-Zion and Sammis, 2003; Chen et al., 2013; Siman-Tov et al., 2013). Second, cylindrical, elongated rolls developed from the cohesive gouge grains, and their formation strongly correlate with the dynamic weakening of the experimental fault. Similar powder rolls were previously observed in friction experiments of silicon (Zanoria et al., 1995a, b), quartz (Nakamura et al., 2012), chert (Hayashi and Tsutsumi, 2010), ceramics (Boch et al., 1989), and alumina (Dong et al., 1991) with measureable friction reduction (Zanoria et al., 1995a, b). Our work shows, for the first time, that powder-rolling can be an effective weakening mechanism of rock faults.

Materials and Methods

Test apparatus

We used a rotary shear apparatus (ROGA) to study the rock friction (Chapter 2). The apparatus can apply up to 35 MPa of normal stress, slip velocities of 0.0003 to 1 m/s, and infinite slip distances. The control system is capable of loading an experimental fault under either constant velocity mode or constant power-density mode (power-density=slip velocity $\times$ shear stress, Boneh et al., 2013). Experimental data of normal load, shear load, slip velocity, displacement, temperature, and dilation are continuously monitored.

The experimental fault was made of two cylindrical blocks: a stationary one with a raised ring- (63.2 mm and 82.3 mm as inner and outer diameters), and a rotating one that is flat-top (101.6 mm diameter and 50.8 mm height). The blocks were pressed against each other along the raised ring. The sliding surfaces were ground flat and roughened with 600-grit SiC powder. Two thermocouples were embedded at 3 mm away from the sliding surfaces. The experiments were conducted either with fresh, ground blocks or with an experimental fault that has already been sheared (Table 1). The experiments presented here were conducted with samples of RRG quarried at Fredricksburg, TX. It has a bulk density of 2614 kg/m^3 and a uniaxial strength of 146.5 MPa. The mineralogy determined by powder X-ray diffraction (XRD) was composed of quartz (43.6%), albite (19.7%), microcline (22.8%), and biotite (13.9%) in weight percent.

Micro-analysis techniques

After a friction experiment, the experimental fault was opened and inspected. We commonly observed shinning, cohesive, curved flakes on the fault surfaces (Figs. 22A, 22B) that were collected for microanalysis. The flakes were sputtered with a metal (Au-Pt) layer about 15 nm thick, and then imaged with the SEM; we used the Zeiss NEON 40 EsB high-resolution field emission SEM at the University of Oklahoma. The highest resolution revealed the Au-Pt conductive coating layer grains which are typically smaller than 20 nm. We used an AFM (Pacific Nanotechnology Nano R2) to determine the surface topography of the flakes at the sub-micron scale.

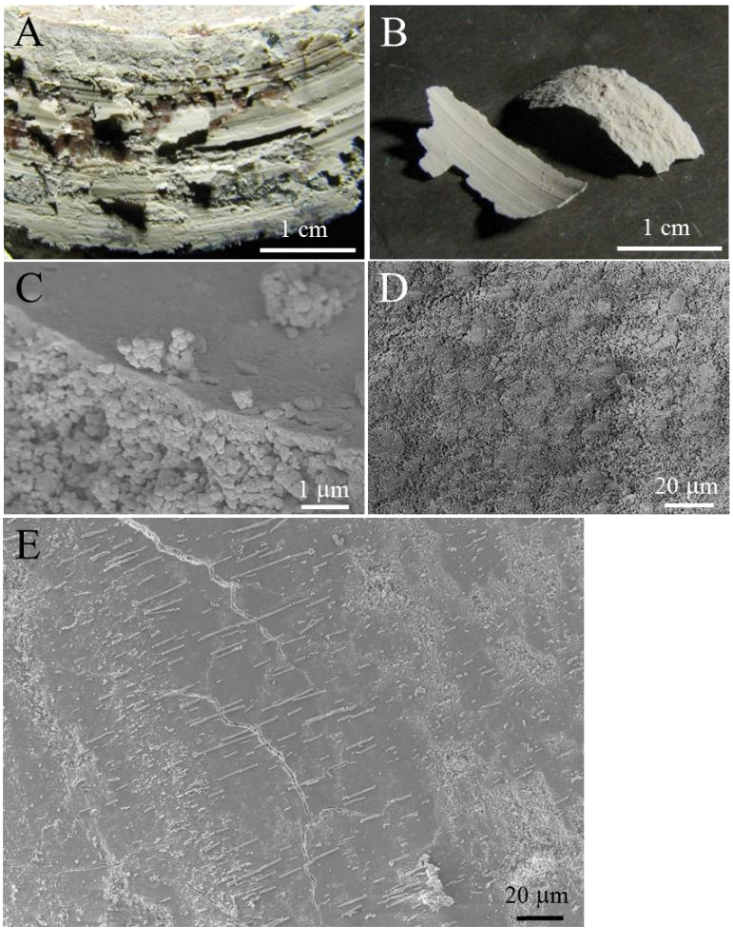

Figure 22. Cohesive, shiny, powder flakes formed on experimental faults during slip. A: Fault surface showing several pieces of flakes formed on the slip surface

(run 3253). B: The curvy powder flakes; note the difference in smoothness on flake top surface (left) and the bottom surface (right) (run 3251). C: SEM view of a flake cross-section showing internal 3D structure, with the substrate loosely compacted with relatively coarse grains, and the top smooth surface (~0.3 μm thick) with dense compacted finer grains (run 2716). D: SEM view of the bottom side of a powder flake that was attached to the host rock block showing rough surface made of loose agglomerated coarse grains (run 2683). E: General view of the powder flake surface showing patches of smooth areas with powder rolls oriented normal to striations (run 2600).

Experimental results

Mechanical data

We performed 34 runs (Table 3) on samples of Radiant Red granite (RRG), with total slip of 0.1-12.94 m, normal stress of 1.1-14.4 MPa, and slip velocity of 0.001-1 m/s. This section outlines typical friction evolution of the present experiments, and later we describe and link these observations to the micron-scale mechanism that apparently controls the friction.

The friction coefficient and slip velocity of typical velocity-controlled and power-controlled experiments are shown in Fig. 23. In most experiments the initial friction coefficient of μ_i = 0.5 - 0.8 dropped to steady state values of 0.2-0.4 after slip distance of 0.5-2 m (Figs. 23A, 23B). The observations are consistent with frictional behavior of silicate rocks under similar velocity range (Reches and Lockner, 2010; Goldsby and Tullis, 2002; Di Toro et al., 2004). The experiments at low velocity (0.001-0.003 m/s) show no weakening, and experiments at high velocity (>0.1 m/s) displayed strengthening (Liao and Reches, 2012). The experimental observations reveal that the macroscopic friction depends on both slip velocity and normal stress as is discussed later.

Table 3. Summary of experiments with the RRG sample. Rolls quality is defined in the text and Fig. 25. Loading Conditions are: 1, for constant velocity; 2, for ramp velocity (velocity rise then drop); 3, for constant power-density.

Exp #	σ_n MPa	velocity m/s	Distance m	μ_i	μ_f	Flakes & rolls	Rolls quality	Loading condition
2554	2.3	0.001	0.55	0.79	0.74	Yes	A	3
2600	2.3	0.014	3.79	0.7	0.30	Yes	B	3
2683	2.4	0.050	12.94	0.62	0.33	Yes	C	3
2704	6.5	0.017	0.14	0.6	0.46	Yes	B	3
2713	1.1	0.012	2.41	0.78	0.49	Yes	C	1
2714	1.1	0.024	2.40	0.75	0.42	Yes	C	1
2715	1.1	0.048	2.42	0.78	0.38	Yes	C	1
2716	1.1	0.047	4.82	0.72	0.34	Yes	A	1
2751	2.4	1.000	2.33	0.8	0.72	No		2
2752	2.4	0.267	2.85	0.85	0.68	No		1
2785	2.3	0.850	3.47	0.82	0.84	No		2
2806	3.8	0.036	4.34	0.60	0.34	Yes	A	1
2807	10.6	0.013	0.10	0.65	0.58	Yes	B	1
2810	10.6	0.024	1.95	0.64	0.48	Yes	A	1
2813	14.4	0.012	1.49	0.7	0.49	Yes	C	1
2832	2.6	0.048	3.63	0.54	0.35	Yes	B	1
3240	2.2	0.001	1.37	0.5	0.38	Yes	B-C	1
3241	2.1	0.004	1.32	0.53	0.34	Yes	B-C	1
3242	2.2	0.012	1.33	0.53	0.38	Yes	A	1
3243	2.2	0.036	1.38	0.52	0.34	Yes	A-B	1
3244	2.1	0.116	1.64	0.56	0.49	No		1
3245	2.1	0.325	1.79	0.5	0.58	No		1
3248	5.8	0.012	1.34	0.6	0.43	Yes	B-C	1
3249	5.6	0.036	1.39	0.72	0.63	Yes	D	1
3250	5.6	0.012	3.95	0.65	0.40	Yes*		1
3251	5.6	0.004	1.25	0.53	0.38	Yes	B-C	1
3252	5.5	0.137	1.69	0.75	0.63	No		1
3253	5.5	0.006	3.79	0.7	0.31	Yes	C	1
3255	1.3	0.001	1.42	0.54	0.58	No		1
3256	1.2	0.004	1.27	0.61	0.59	No		1
3257	1.2	0.035	2.69	0.65	0.29	Yes	C	1
3258	1.2	0.111	2.96	0.55	0.50	No		1
3259	1.2	0.036	5.43	0.51	0.16	Yes	A-B	1
3260	1.2	0.012	6.01	0.51	0.24	Yes*		1

** Runs 3250 and 3260 generated tiny powder flakes that are too small for sampling.*

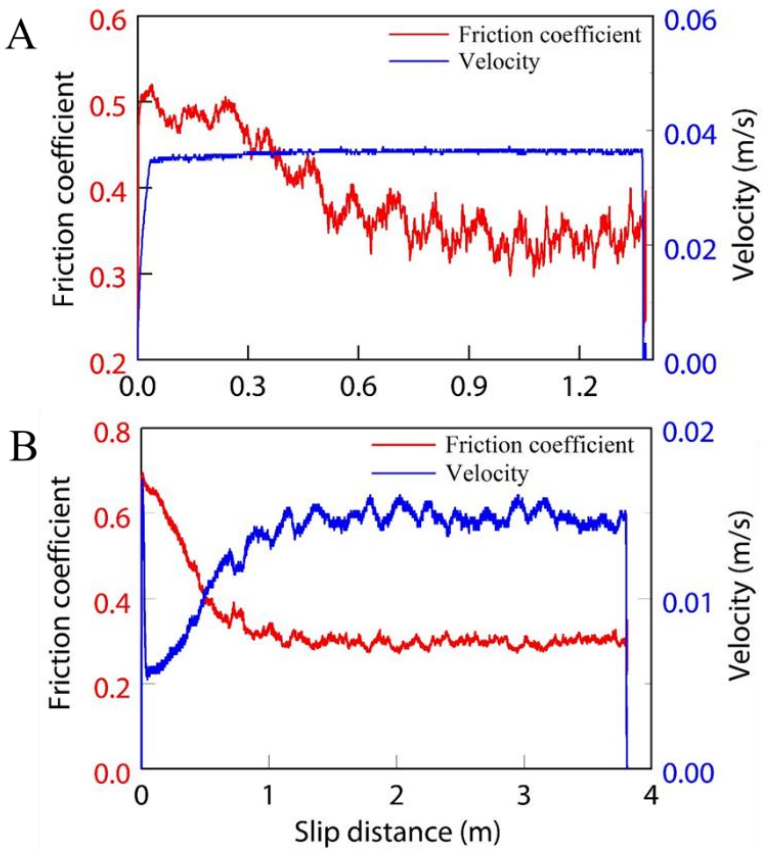

Figure 23. Experimental friction evolution with slip distance. A: Constant-velocity experiment at 0.036 m/s (run 3243). B: Power-controlled experiment in which the power-density (=shear stress × slip-velocity) was maintained constant by the feedback control (run 2600).

Micro-structure: smooth surfaces and powder rolls

The micro-structural analysis was conducted on the cohesive flakes (Figs. 22A, 22B) that were collected at various stages of slip (Table 3). The flakes grew within the freshly formed gouge powder of the experimental fault after displacement of tens of cm or more, and they were found in both experiments that started with fresh, ground fault surfaces and with a fault surface cover with gouge of previous runs. These flakes were observed regardless of the loading mode, in both velocity-controlled and power-

controlled conditions (Table 3). Flakes were found on both blocks of the experimental fault, while sometimes they were preferentially bound onto one block.

The scanning electron microscopy (SEM) and atomic force microscopy (AFM) analyses of the flakes revealed three prevailing structural features:

1. At the scale of light microscopy, the flakes appear cohesive and are a few hundred microns thick (Figs. 22A, 22B). Internally, the flakes are made of a layered 3D structure of agglomerated powder grains less than one micron in size with a few angular, larger grains embedded in the porous matrix (Fig. 22C). The flakes have two distinctly different zones. The rough, porous, coarse zone (Figs. 22B, 22D) was attached to the solid, rough surface of the host rock. The other zone formed a smooth and shiny surface (Figs. 22A, 22B, 22E) that faced similar smooth surface on the matching side of the fault. Detailed description of the shiny surfaces appears below.
2. Shiny surface is a 0.1-0.5 μm thick layer composed of a well-compacted, dense mosaic of ultra-fine grains that are 20-50 nm in size (Fig. 22C). We observed local indications of grain sintering (Figs. 2A, 24B, 24D, 24F, 24G) and platelets of sub-micron sizes stacking on top of the shiny surface (Figs. 24A, 24B, 24F). This surface commonly displays distinct slip-parallel striations (Figs. 22E, 25A-25C), and micron-sized wear debris of agglomerated nano-grains (Figs. 22C, 22E, 24D, 24G, 25A-25D). As these smooth, shiny surfaces face each other on the opposite sides of the fault, and as they carry slip-parallel striations, they are interpreted as zones of slip localization within a gouge layer of disorganized fine, powder grains (Fig. 22A). Similar smooth surfaces of localized slip were observed in many friction

experiments of solid rocks and gouge layers and natural faults (Han et al., 2010; Chen et al., 2013; Siman-Tov et al., 2013; Smith et al., 2011). We refer to the smooth, shiny surface as a Principal Slip Zone (PSZ).

3. Most striking feature observed on the PSZs is powder rolls that are: (1) made of agglomerated fine powder grains; (2) cylindrical in shape; (3) trend normal to slip direction; and (4) develop only on isolated patches of smooth, clean surfaces of PSZ (Fig. 22E). Description and interpretation of these powder rolls are presented below.

The rolls are invariably made of agglomerated powder grains of particle size of 20 to 100 nm (Figs. 24B, 24C, 24E). An ideal roll is a long cylinder, with well-rounded, smooth outer surface formed by closely packed grains in a 3D structure with a few voids (Figs. 24A, 24C). A roll with a solid center is usually well compacted and externally smooth (Figs. 24B, 24C, 24H), whereas a less well developed roll contains more voids and deviate from the cylindrical shape (Figs. 24D, 24F, 24G). Some rolls are poorly developed, with partial compaction, and rough exterior (Figs. 24A, 24D, 24F). The roll diameters have a narrow range of 0.5-1.75 μm (Fig. 26A) with mean diameter of 1.04 ± 0.25 μm; their lengths vary from 1 to 26 μm. Many rolls are partly destroyed by axial fractures (Figs. 24F, 24G, 25C), and broken rolls are smeared on the slip surfaces (Figs. 24F, 24G). The appearance of both intact and fractured rolls suggests that they undergo a life cycle, which will be discussed later.

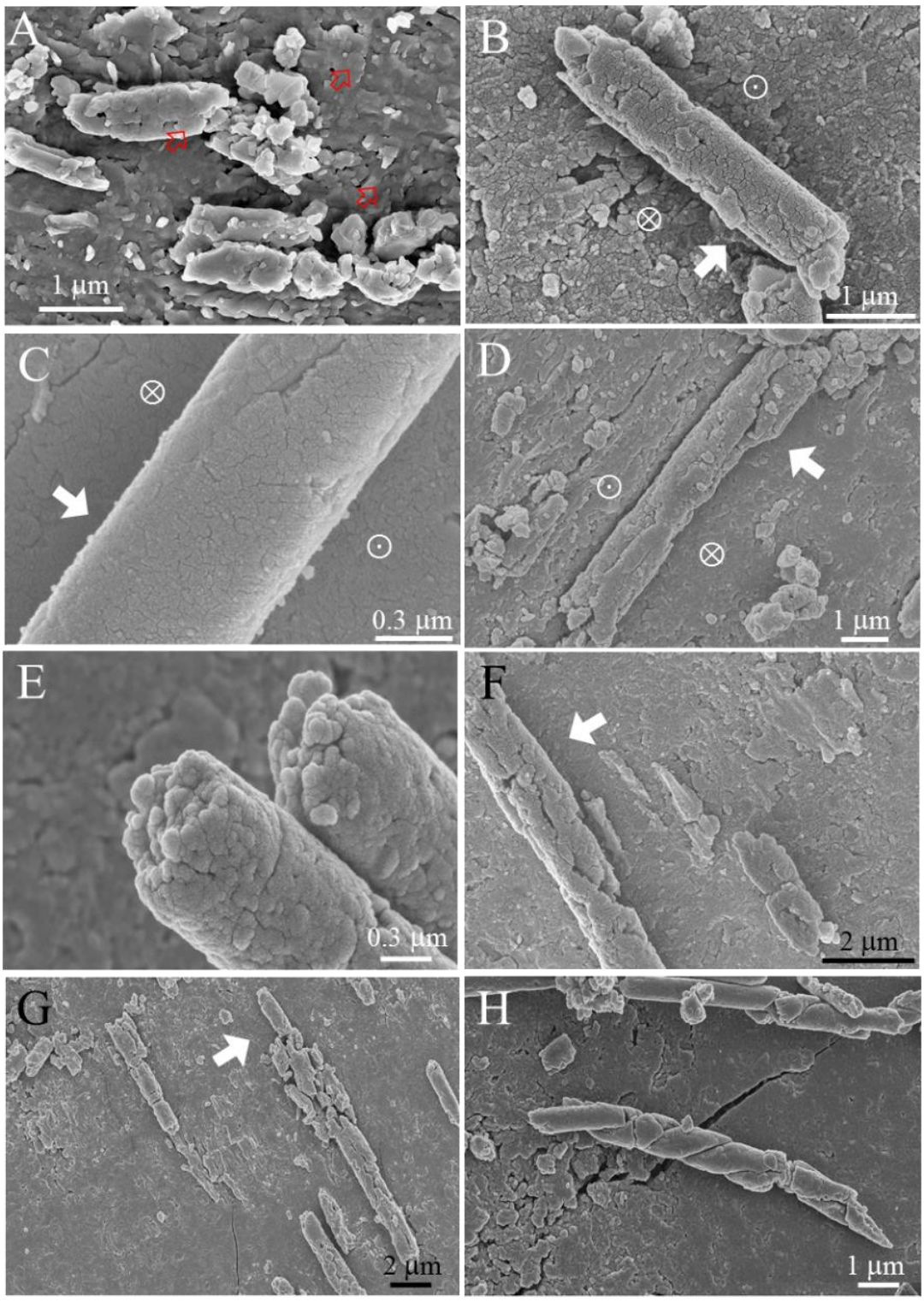

Figure 24. Close-up views of powder rolls. A: Rolls developed on smooth PSZ. Note sub-micron size thin platelets wrapping up the rolls stacking on the PSZ surface (red arrows) (run 2832). . B, C and D: deformation of the PSZ surfaces below rolls while rolls maintain round (run 2683, 2554, and 2807 for B, C, and D,

respectively). The asymmetric deformation are marked as the inward arrow in the gentle-depressed sides and the outward arrow in the abrupt depressed sides. White arrows indicate rolling direction of rolls. E: Well compacted rolls with solid interior. Note the composing grains of <100 nm (run 2716). F and G: broken rolls left traces on PSZ surface showing smearing of materials and axial fracturing. White arrows indicate rolling direction (run 2600, 2704 for F and G, respectively). H: two rolls twisted against each other (run 2716)

.

The quality of the powder rolls was evaluated in the SEM images based on the following qualitative criteria: A. Well-developed rolls of idealized cylindrical shape, distributed on well-developed, smooth PSZ, with systematic orientation normal to slip direction (Fig. 25A). B. Rolls that are nearly ideal, cylindrical shape, distributed on well-developed, smooth PSZ, but with occurrence of scattered particles in roll areas. Rolls are orientated parallel to each other, with local deviations. Appearance of a few broken rolls and a few truncated, short rolls is common (Fig. 25B). C. Rolls deviate from cylindrical shape, with many broken and smeared rolls, truncated, short rolls and many scattered particles (Fig. 25C). D. Well-established PSZ surfaces with many particles, rolls are loosely compacted and close to grain-aggregates (Fig. 25D). The quality of rolls on a single flake may vary from high-quality rolls to low quality rolls (Figs. 25A, 25B).

Close-up view of the contacts between the powder rolls and the PSZ surface reveals that the rolls deform the host PSZ by forming a depression in which one side is gently inclined (inward arrow in Figs. 24B, 24D, 24F), whereas the other side bulges abruptly out of the depression (outward arrow in Figs. 24B, 24D, 24F). This deformation occurs while the rolls remain cylindrical.

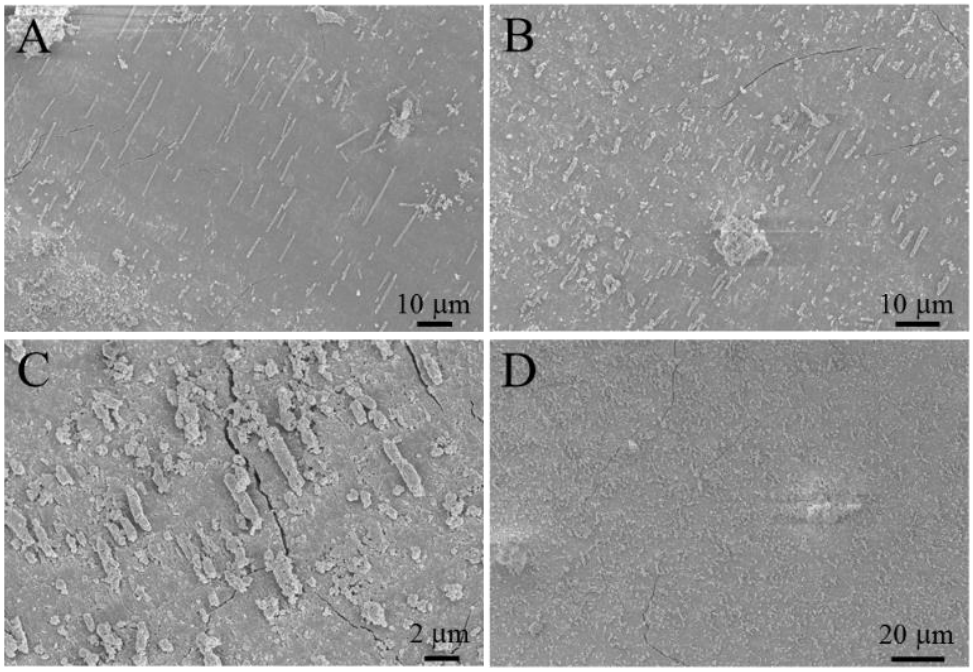

Figure 25. General view of rolls showing the quality of powder rolls from the best (quality A) to worst (quality D) for runs 3243, 3243, 2813, and 3249.

Finally, a central observation is that the long axes of the rolls are systematically oriented normal to the striations (parallel to slip direction) (Figs. 22E, 25A-25C, 26B). The mean orientation of the measured 1183 rolls in 12 experiments is 95 º ± 26 º.

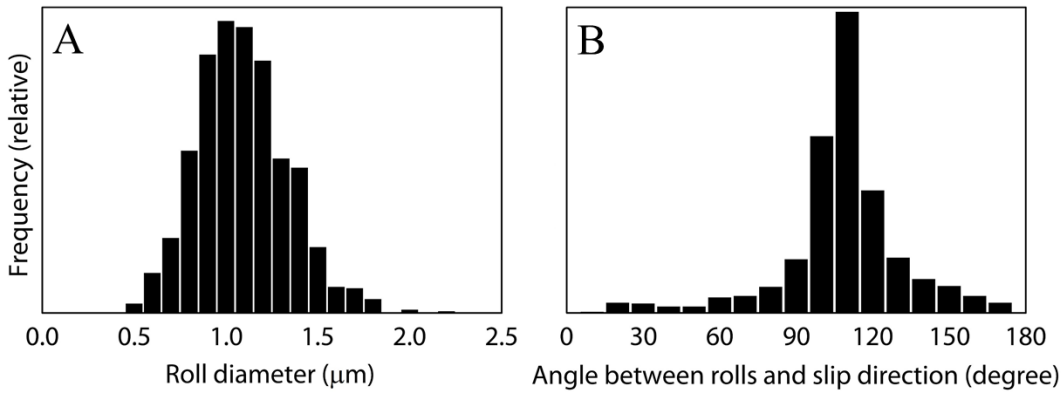

Figure 26. Statistics of rolls diameter and orientation on 14 SEM images of 1183 rolls. A: Frequency distribution of rolls diameter measured on SEM images with average diameter of 1.04±0.25 µm. B: Rolls' orientation with respect to slip direction showing an average of 95 º ± 26 ºfrom slip.

Analysis

Formation and life cycle of powder rolls

The powder rolls in the present experiments are strikingly similar in diameter, length and orientation to debris rolls found in shear experiments of ceramics, silicon, quartz, chert, and alumina (Hayashi and Tsutsumi, 2010; Zanoria et al., 1995a, b; Nakamura et al., 2012; Dong et al., 1991; Boch et al., 1989). These similarities suggest a general mechanism of roll formation and destruction (Zanoria et al., 1995a) (Fig. 27). During initial slip, the experimental fault surfaces wear to generate a fine-grain gouge layer (Reches and Lockner, 2010; Boneh et a., 2013) that separates the solid rock blocks (Fig. 27A). The slip is initially accommodated within the entire gouge layer, but quickly localizes along discrete thin principal slip zones (PSZs). The frictional heating and further grain-size reduction within the PSZs, lead to grain compaction, agglomeration, local sintering enhanced by quartz amorphization (Nakamura et al., 2012) and absorption of atmospheric water (Hayashi and Tsutsumi, 2010). These processes lead to the formation of cohesive gouge flakes with smooth, continuous top PSZ surface (Fig. 27B). Debris of gouge powder grains and delaminated fragments of the PSZ layer overlie the PSZ surfaces (Fig. 27C). Locally, this debris agglomerate into powder rolls by the shear-induced torque between the opposing slipping surfaces of the PSZs (Fig. 27D). The rolling of the powder rolls further enhances the compaction of both the powder rolls themselves and the PSZ and also help clean up the PSZ surface by incorporating encountered particles (Fig. 24B). As this process is shear driven, it generates powder rolls with axes normal to slip direction (Fig. 26B). As rolls encounter rough areas or areas with more wear debris, the rolls are vulnerable to damaging by

collapse and fracturing (Figs. 24E-24G, 25C). The debris of the failed rolls are re-agglomerated into new rolls and smooth surfaces until a dynamic balance of steady state between formation and destruction is reached. Fault slip along the smooth patches of PSZ was facilitated by rolling of the powder rolls, and the weakening along these spots lowers the overall friction.

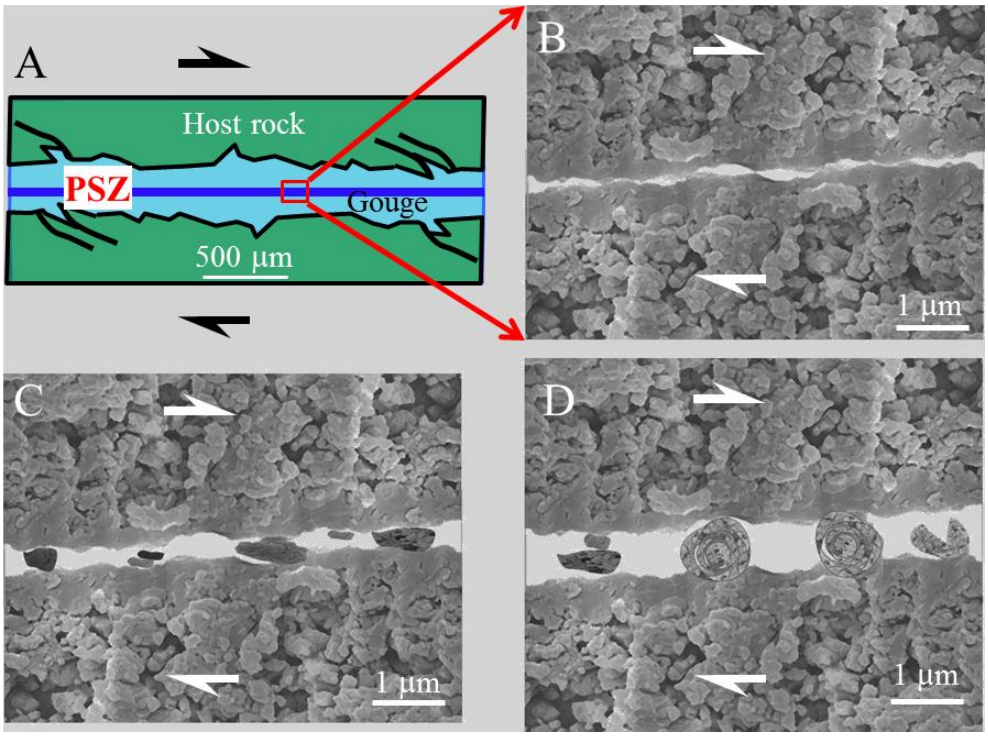

Figure 27. Proposed formation mechanism and life cycle of powder rolls. A: Slip localization within a narrow zone (PSZ), a few microns thick, inside the gouge layer. B: SEM image of the cross section of the PSZ showing formation of a PSZ as a layer of compacted ultra-fine grains resting on a porous matrix of coarser grains (Fig. 22C). C: Debris of grains, agglomerated grains and delaminated PSZ between the two smooth PSZ surfaces. D: Rolling of the debris (left) into powder rolls (center), and eventual destruction (right side). Shear direction marked by half arrows.

The development of the PSZ along faults is critical for roll formation as powder rolls were observed only on cohesive gouge flakes (Table 3). The present smooth, clean PSZs (Figs. 22B, 22C) are analogous to the compacted silica films of Zanoria et al.,

(1995a). Due to the roughness of the experimental faults, only a small portion of the opposing fault surfaces is in contact (Dieterich and Kilgore, 1994), in which powder rolls ere formed by the processes described above. This is the reason pin-on-disc friction experiments (Zanoria et al., 1995a, b; Nakamura et al., 2012) can generate high quality powder rolls across the slip zone, while rotary rock friction experiments with large contact areas only generate powder rolls on patches of only a small portion of the available contact area, leading to variable rolls quality.

Frictional strength and powder-rolling

Macroscopic friction evolution

We found that the existence of powder rolls is systematically associated with reduction of the macroscopic friction coefficient. This reduction is first observed by comparing the initial friction coefficient, μ_i, and the final friction coefficient, μ_f for all experiments (Fig. 28A). The figure reveals consistent friction reduction in experiments with powder rolls (red dots), and no (or minor) friction reduction in experiments without powder rolls (blue dots). Second, the final friction coefficient normalized against the initial value, μ_f / μ_i, shows a systematic decrease with slip distance in experiments with rolls (red dots in Fig. 28B). The data points of runs with rolls fit exponential slip-weakening predicted by Mizoguchi et al. (2007) (Fig. 28B) as shown the following curve in Fig. 28B,

$$\frac{\mu_f}{\mu_i} = 0.43 + 0.57 \exp\left(\frac{\ln(b) \cdot D}{D_C} \right) \quad (1)$$

where μ_f is the final friction coefficient, μ_i is the initial friction coefficient, D is slip distance, and D_C is the distance over which μ_f/μ_i reduces to the fraction b of the total

weakening. The best-fit exponential curve here is for b=0.1, and D_c=4.3 m. The trend for rolls is in reasonable agreement with the observations of Zanoria et al. (1995a, b) for silica samples sheared at controlled humidity and temperature (purple dots in Fig. 28B). This slip-weakening trend in our experiments fits well the classical slip-weakening curves observed here (Fig. 23) and elsewhere (Di Toro et al., 2011).

The slip-weakening behavior of roll-bearing experiments leads to two important deductions. First, a characteristic shear strain, which is manifested by the slip distance, is required for the formation of powder-rolls. This shear strain is needed to localize the slip, and build the smooth PSZs on which the powder rolls can form. Second, the powder rolls presence and the associated weakening according to the predicted style of slip-weakening (Mizoguchi et al., 2007) strongly suggest that the powder-rolling facilitates this dynamic weakening.

Rolling friction mechanics

The powder rolls described above are distributed on smooth PSZs (Figs. 22E, 24, 25), are oriented normal to the slip direction (Figs. 22E, 25A-25C, 26B), and form between two PSZs (Fig. 27). We thus idealize the system of multiple, parallel powder rolls of equal diameter (Fig. 26A) placed between two smooth PSZs by a roller-bearing. In this section, we use this roller-bearing model to evaluate powder-rolling mechanics.

Consider the rolling of a cylinder (or a sphere) on a flat surface (Fig. 29A). This motion can be described by the transition between two idealized end members. **Sliding** occurs when the roll slides at velocity V with respect to the surface, but it does not spin,

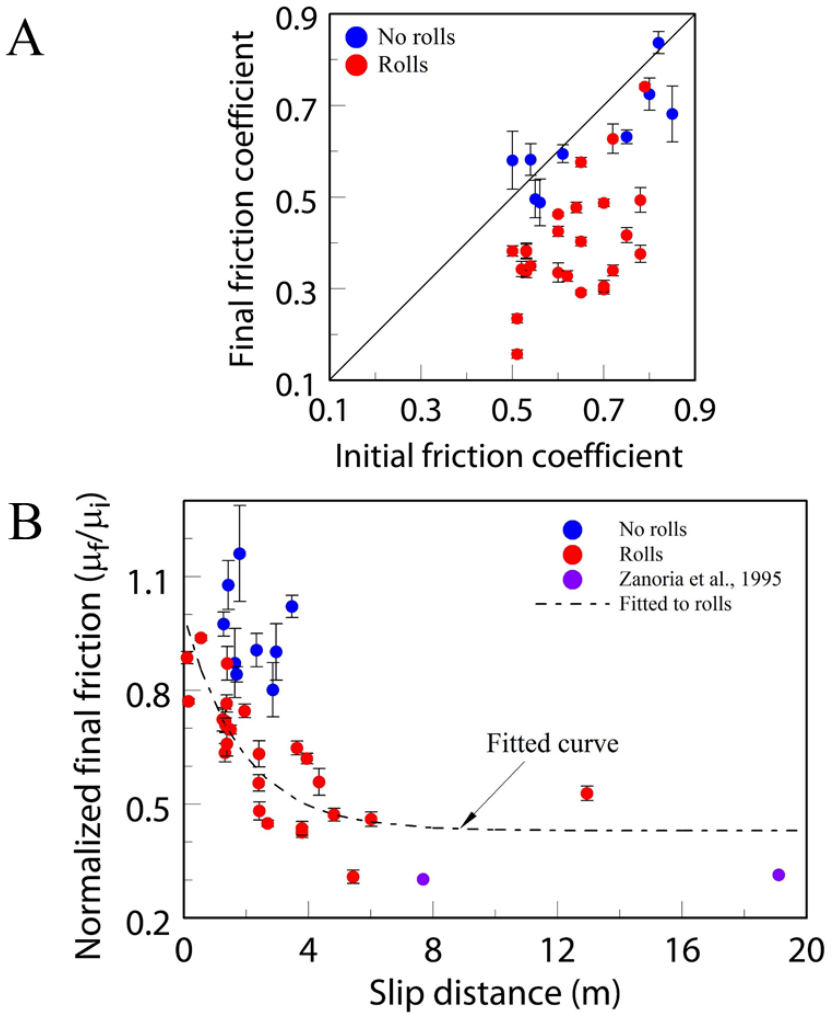

Figure 28. Correlation between rolls and friction reduction. A: The final friction coefficient, μ_f, as a function of initial friction coefficient, μ_f, for all experiments. Note that runs with rolls (red dots) are plotted below the friction equality line indicating friction reduction, whereas runs without rolls (blue dots) are distributed around the equality line indicating minor weakening or strengthening. B: Normalized final friction coefficient, μ_f / μ_i, as function of slip distance. Runs with rolls (red dots) showed systematic dependence of μ_f / μ_i on slip distance (dashed curve and equation) that agrees with the observations of Zanoria et al., (1995a, b) (purple dots). Runs without rolls (blue squares) show no systematic friction reduction for similar slip-distances.

namely its angular velocity vanishes, $\omega = 0$. In this case, the resistance to slip can be expressed as $F_S = \mu_{slide} \cdot F_N$, where F_S and F_N are the shear force and normal force acting on the roll, and μ_{slide} is the sliding friction coefficient between the roll and the surface.

Rolling occurs when the motion is fully accommodated by the roll's rotation along the surface, and in this case $V = 2R\omega$ where R is the roll's radius. Along parts of the contact between a roll and the surface, the shear stress is lower than the shear resistance (friction and/or adhesion), and thus these parts are "glued" to the surface. The gluing makes it possible for the roll to rotate rather than slide. For example, the high friction between rubber tires of a car and the road facilitates the car's motion.

We now analyze the rolling friction of the powder rolls following the approach and results of Eldredge and Tabor (1955) and Tabor (1955). They examined the system of a hard steel sphere that rolls between two flat, parallel blocks of softer metals (tin, lead, copper) (Fig. 29A) In this model, the soft plates are plastically deformed as recognized by the grooved tracks, and the size of the deformed zone can be evaluated from the size of the grooves. In the experiments of Eldredge and Tabor (1955) and Tabor (1955), the shear force, normal force, and indentation depth into the softer surface were measured, allowing calculation of the shear stress, P_f, and normal stress, P_m, that act on the soft plate indentation zone. They showed that $P_f = P_m$, as expected because both these stresses reflect the plastic strength of the same plate. In their experiments, the authors found that the shear force is $F_S = k\ F_N\ 1.5\ /D$, where F_S and F_N are the shear and normal forces on a single sphere, D is the sphere's diameter, and k is a constant that depends on the soft metal properties.

We adopt this model of rolling friction to the cylindrical powder rolls in our experiments. Fig. 29A displays a cross-section of a loaded powder roll that is sheared between two smooth PSZs. Roll diameter is D and length is L. We assumed that: (A) $P_f = P_m$ (following Eldredge and Tabor's observations); (B) the powder roll does not

deform, based on our observations that most rolls are cylindrical (Fig. 3); and (C) the smooth PSZ surface deforms (bulges and depressions in Figs.24B, 24D, 24F) by F_S and F_N loading.

The loading by the normal force F_N deforms the PSZ surface in a zone of width d/2 and depth b (Fig. 29A). The mean stress on the zone of d/2 width is

$$P_m = F_N \Big/ \left(L \cdot \frac{d}{2} \right) \tag{2}$$

The shear force F_S acts parallel to the PSZ surface and on a zone of thickness b, and thus the mean stress on this zone is

$$P_F = F_S / (L \cdot b) \tag{3}$$

From the geometry of the deformation area, one can derive that

$$b = \frac{1}{2}\left(D - \sqrt{D^2 - d^2} \right) \tag{4}$$

By using assumption (A), equations (2) and (3), and substituting with equation (4), we get

$$\mu_R = \frac{F_S}{F_N} = \frac{2b}{d} = \frac{D}{d} - \sqrt{\frac{D^2}{d^2} - 1} \tag{5}$$

The last equation provides the rolling friction coefficient as μ_R due to the work associated with the plastic deformation. This equation is used to display the predicted rolling friction as function of the penetration factor D/d (Fig. 29B).

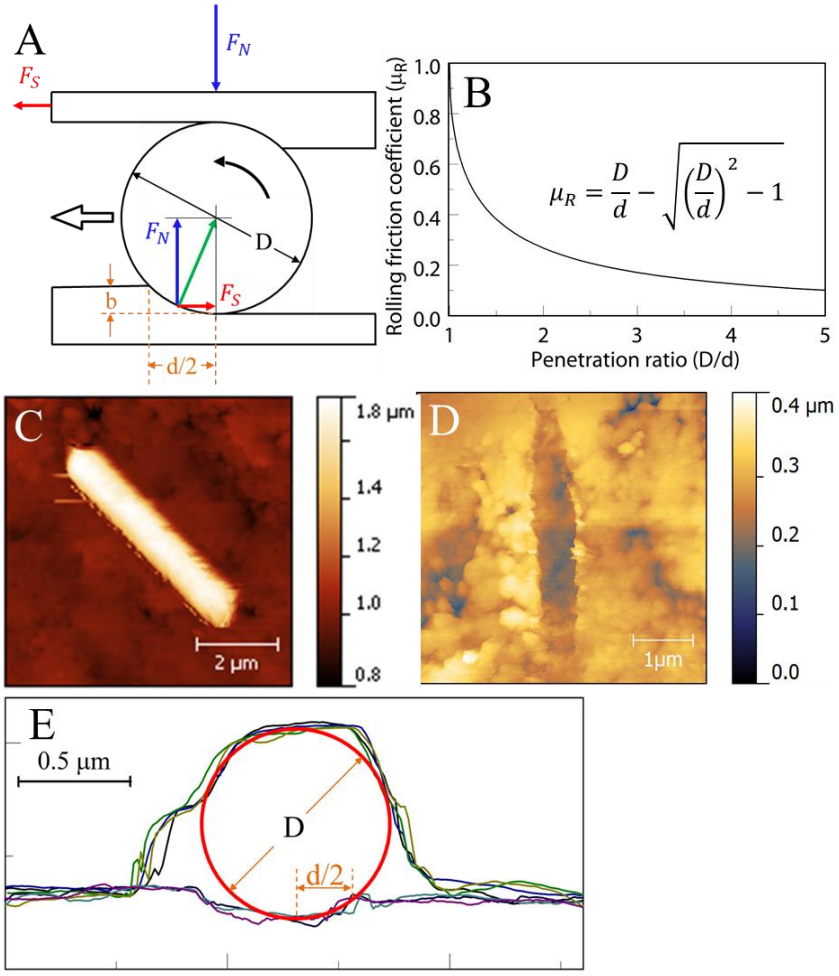

Figure 29. Rolling friction of powder rolls. A: Idealized two-dimensional model, after Eldredge and Tabor (1955) and Tabor (1955), of a cylindrical roll of diameter D and length L sheared between two softer slip surfaces. The stressed roll penetrates the slip surface over penetration zone of width d/2 and penetration depth b (text). B: Rolling friction coefficient, μ_R, as function of the penetration ratio, D/d; inset: μ_R as equation 4 in the text. C: AFM morphology of a single roll (bright zone trending NW-SE) resting on PSZ surface (run 2810); note the the roll is ~ 1 µm higher than the substrate. D: AFM morphology of the PSZ surface after the powder roll was pushed away with AFM tip; note N-S depression about 100 nm deep of the removed roll. E: A series of seven profiles derived from across the AFM images of C and D normal to the roll. The four upper curves, taken in C, delineate both the PSZ and top of the roll. The three lower curves, taken in D, delineate the PSZ without the roll and reveal the shape and depth of the depression. A red circle of D = 0.85 µm was visually fitted to be bound by the upper and lower profiles; this circle is the idealized roll that was removed. Note that the down-facing parts of the roll cannot be traced by the AFM tip and thus the upper profiles cannot accurately delineate the sides of the roll. The roll penetrated the PSZ over a region of d/2 ~ 0.29 µm (yellow arrow).

Application to present experiments

The derivation above indicates that the rolling friction, μ_R, is a function of the intensity of the penetration depth ratio D/d (Fig. 29B). Small D/d ratio implies large penetration, which corresponds to a softer slip surface, and the inverse for large D/d. The model predicts a friction drop with increasing D/d (Fig. 29B), e.g., $\mu_R < 0.3$ for $D/d > 1.8$. Micro-scale images showed that the powder rolls in the experiments were sheared between two smooth slip surfaces (PSZ), and they support the normal stress applied on the fault. This structure indicates that the rolls converted the experimental fault into a roller-bearing as proposed above, and switch the friction from sliding mode to rolling mode. It is important to note that unlike steel rolls of industrial bearing where rolls persist over different shear conditions, the powder rolls undergo formation-and-destruction cycle throughout the shear (Fig. 27).

To test the above model, we used the AFM to measure the geometric relations of a roll and PSZ. Two sets of surface maps were measured: the first with the roll resting on the PSZ (Fig. 29C), and the second after the roll was pushed away to reveal the topography of the PSZ depression (Fig. 29D). Fig. 29E displays elevation profiles normal to the roll as taken from the two maps. The two sets of profiles suggest that a roll of ~0.85 μm fits the profile (red circle), and the penetration zone is d/2 ~0.29 μm (thin yellow arrow line). These values yield $\mu_R \sim 0.4$ which is similar but lower than the 0.47 macroscopic friction coefficient in this experiment.

Discussion

Faulting conditions that enhance powder-rolls formation

Powder rolls were not observed in all our experiments (Table 3). Part of this limited appearance stems from sampling difficulties; for example, many opportunities exist for losing powder rolls in sample collection and preparation, and locating the small clean, smooth areas in the cohesive gouge flake top surfaces is not always an easy task. Beyond these technical difficulties, there are limiting mechanical factors displayed on a map of the normalized experimental final friction coefficient, μ_f/μ_i, as functions of the normal stress, σ_n, and slip velocity, V (Fig. 30). The figure shows that powder rolls (red circles) are present in runs of V < 0.07 m/s, and that the lowest values of μ_f/μ_i (as low as 0.3) are restricted to V = 0.003 - 0.06 m/s and σ_n = 1 - 5 MPa. Experiments without powder rolls and high friction (blue circles) appear in runs at V > 0.1 m/s, and at combined low velocity (V < 0.004 m/s) and low normal stress (σ_n < 2 MPa).

This distribution of powder rolls and associated friction values is compatible with previous experimental studies of granite friction (Reches and Lockner, 2010; Kuwano and Hatano, 2011). These studies showed that the steady-state friction of granitic rocks changes non-monotonically with slip velocity (Fig. 1 in Reches and Lockner, 2010): High friction coefficient at V < 0.005 m/s, minimum friction values ($\mu_f \sim 0.3$) at V=0.01- 0.05 m/s, and strengthening to static friction values at V > 0.07. Fig. 30 reflects this trend. The strengthening at V > 0.07 m/s was attributed to dehydration of the water coating of the fine-grain gouge powder by the high-velocity heating (Sammis et al.,

2011), or to the partial unloading of the stress by volumetric expansion of local melting (Chen et al., in preparation).

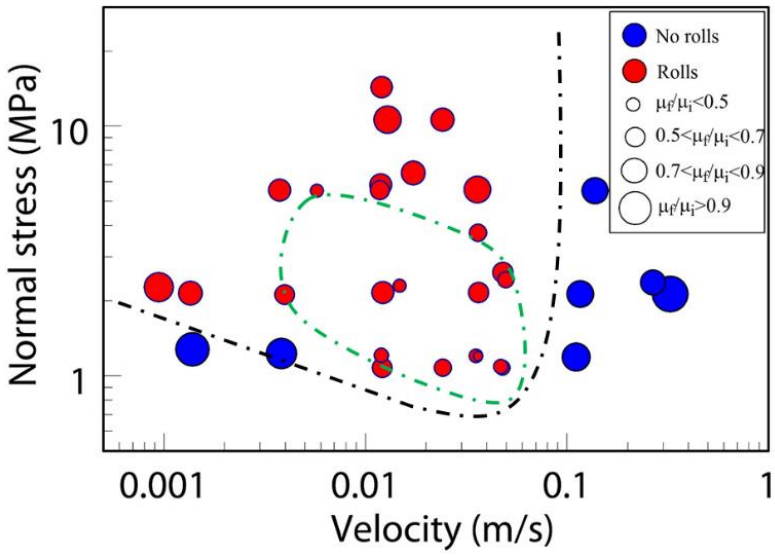

Figure 30. A friction map (after Boneh et al., 2013) displaying normalized final friction coefficient, μ_f/μ_i , as function of normal stress and slip velocity. Symbol size is proportional to the normalized friction and the circle color indicates the presence (red) or absence (blue) of rolls. Note the strong correlation of low friction with rolls presence.

More specifically, our analysis shows that powder roll formation requires development of PSZ surfaces of localized slip (Figs. 22, 24, 25, 27, and appearance of rolls accompanied formation of cohesive gouge flakes in Table 3). The PSZ formation is enhanced by elevated fault temperature that depends on power-density (shear stress × velocity) (Boneh et al., 2013). The velocity range of V=0.01- 0.05 m/s generates favorable conditions of humidity and temperature that are necessary for PSZ and roll development (Zanoria et al., 1995a). At low velocity (low power), the fault temperature does not reach the range for PSZ formation or cannot maintain stable PSZ surfaces, and this results in covering the fault surface by incohesive gouge and associated high

friction coefficient. At V>0.07 m/s, the favorable conditions for powder-rolling were no longer met, which led to the destruction of PSZ and powder rolls by dehydration or local melt and formation of incohesive gouge again (no cohesive flakes in high velocity runs in Table 3). Zanoria et al., (1995b), found that the diameter and length of rolls increase with temperature, while the rolls population density decreases with temperature. These opposite effects generally balanced each other, resulting in a friction coefficient insensitive to temperatures and normal load. This result suggests that while rolling can reduce fault friction, rolling weakening has no simple relation to slip velocity as demonstrated in Fig. 30.

We noticed that the above mechanical conditions are similar to those reported previously for friction experiments on quartz-rich rocks (Goldsby and Tullis, 2002; Di Toro et al., 2004; Hayashi and Tsutsumi, 2010). The common features for these experiments are the velocity range of V = 0.003 – 0.1 m/s, the appearance of shiny, flaky gouge on fault surfaces and the formation of silica gel. The silica gel formed thin, amorphized layers of fluid-like material that was attributed to the weakening (gel lubrication). In our experiments with granite sample, silica-gel could form at the experimental conditions due to the presense of quartz. Indeed, minor amounts of silica-gel could enhanced powder-rolling by establishment of cohesive gouge layer, facilitating rolls formation, and enhancing compacting and densification of rolls and PSZs. However, our experiments displayed no evidence of fluid-like flow structures either on the top of PSZ or in its cross-section. In addition, the slip surfaces were covered with solid grains and rolls that deformed the PSZs (Figs. 24, 25). We thus

envision that once the PSZs and rolls developed, powder-rolling became the dominant weakening mechanism.

Powder-rolling as an effective fault weakening mechanism

Our observations of powder rolls, PSZ structure, roll orientations, and deformation structures are direct evidence for rolling during the friction experiments. The strong correlation between rolls presence and friction reduction, and the low rolling friction derived from deformation structure suggest powder-rolling is the most likely and effective dynamic weakening mechanism in the present loading conditions (Fig. 30). We further propose, based on previous observations of rolls in other contexts (Hayashi and Tsutsumi, 2010; Zanoria et al., 1995a, b; Nakamura et al., 2012) that powder-rolling could be active as a general mechanism of powder–lubrication (solid lubrication, Wornyoh et al., 2007).

Our experiments show that the activation of powder-rolling requires two ingredients: (1) the existence of ultra-fine powder, and (2) the localization of slip along discrete, smooth surfaces. These ingredients are common in faults in the upper crust. First, natural fault-zones contain granular layers that are dominated by particles in the range of 20-100 nm. For example, the few cm thick ultracataclasite (cohesive, ultra-fine grained rock) zone in the core of the North San Gabriel fault (Chester et al., 2005), or the gouge zone of the exposed San Andreas fault in Tejon Pass area (Wilson et al., 2005). Second, slip localization is commonly observed in natural fault zones (Ben-Zion and Sammis, 2003; Chester et al., 2005; Sibson, 2003; Katz et al., 2003). Some field studies indicate that slip of tens of km may be localized within a fault core which is less than 1 m thick with further extreme localization along thinner ultracataclasite bands

(Chester et al., 1993). Thus, it is expected that powder-rolling would activate dynamic weakening of natural faults.

Summary

The present set of experiments performed with a rotary shear apparatus on radiant red granite demonstrated that powder-rolling is an effective mechanism of powder lubrication and contributes to the dynamic weakening at moderate velocity ranges up to a few cm/s and moderate normal stress ranges up to a few MPa. This conclusion is based on the following observations:

1. Macro friction reduction correlates with the observation of cohesive flakes and powder rolls present on flake surfaces (Figs. 28, 30).
2. The spontaneous development of powder rolls and PSZ along with the micro-structure of powder rolls such as the roller-bearing structure, roll orientations, asymmetric depression suggest that these powder rolls were formed by rolling and they rolled instead of slid on surfaces (Figs. 22, 24, 27, 29).
3. The calculated rolling friction coefficient is lower than the overall friction (Eq. 4) and the amount of weakening systematically increased with slip distance (Fig. 28B), suggesting that the small patches with powder rolls served as regions of fault weakness and contribute to the reduction of the overall friction.
4. Powder-rolling is a likely mechanism of solid lubrication.

Chapter 5: Frictional melting of granite faults as mechanical and material phase-transition

Introduction

This chapter summarizes my research on frictional melting of experimental granite faults. During high-velocity fault slip, the associated frictional heat could lead to melting within the fault zone. The natural frictional melt product, termed pseudotachylite, is a dark, aphanitic, glassy material commonly observed by dike-like veins and networks. The presence of pseudotachylites is recognized as a clear indicator of fossil seismic events (Spray, 2010; Lin, 2008). The links between frictional melt and earthquakes led to many studies of frictional behaviors associated with melt formation with emphasis on mechanical and melting processes, temperature evolution, the transition from solid state faulting to melting, and the chemical/mineralogical evolution of the melt (Spray, 1993; Shimamoto and Lin, 1994; Hirose and Shimamoto, 2005; Di Toro et al., 2006, 2011; Niemeijer et al., 2011; Del Gaudio et al., 2009).

Interestingly, most frictional melting experiments were performed with samples made of gabbro, peridotite, and basic metamorphic rocks, while only a few high-speed shear experiments were conducted on granitic rocks (Spray 1993, 2005, 2010). This situation probably reflects the tendency of granitic rocks to fracture at high thermal stress during high-velocity shear in rotary apparatuses. The large differences of thermal expansion between quartz versus feldspars in granitic rocks induces inhomogeneous thermal expansion and intense thermal stresses that fracture the granite. As Toshi Shimamoto said (personal communication to Ze'ev Reches, 2008): "granite fractures before it melts and gabbro melts before it fractures…"

This chapter focuses on our experiments at medium slip rates (a few cm/s) for long distances (tens of meters) with granitic rocks. These experiments frequently show a complex evolution of friction with slip-distance from weakening to temporary strengthening, to final weakening (as described in detail below). The characterization of the transition from weakening to strengthening showed a power-law dependence on the dissipative power density, and the temporal increase of normal stresses during this transition. The normal stress increase indicated a volumetric expansion mechanism similar to the gabbro "melt welt" (Brown and Fialko, 2012). The final weakening is governed by melt lubrication as confirmed by the observation of frictional melt in the fault zone.

Background

Laboratory simulation of frictional melting has been successfully carried out with high speed rotary shear apparatuses (Di Toro, 2006; Hirose and Shimammoto, 2005; Reches and Lockner, 2010). Most experimental melting studies used gabbro samples that melts at typical conditions ~ 1 m/s and above, normal stress of a few MPa to tens of MPa, and slip distance of tens of meters (Hirose and Shimamoto, 2005; Niemeijer et al., 2011; Del Gaudio et al., 2009). The common friction evolution during laboratory rock frictional melting experiments are (Fig. 31): (1) initial weakening during the first few meters of slip, (a-b) in Fig. 31A; (2) transition to unsteady dynamic strengthening, (b-c-d) in Fig. 31A, (3) peak friction marks the onset of wholescale, continuous melting (d) in Fig. 31A, (4) an gradual decay of friction when bulk melt layers cover the whole fault zone, (d-e) in Fig. 31A, (5) a short strengthening stage when the slip slows down (f) in Fig. 31A. The first weakening was attributed to flash heating (Hirose and Shimamoto,

2005). The second, exponential weakening at the bulk melt stage was termed "melt lubrication", and was attributed to fluid behavior governed by melt viscosity. The temporary strengthening, (b-d) in Fig. 31A preceding peak friction was attributed to the "viscous break" effect, arises from resistance of the melt patches to smearing.

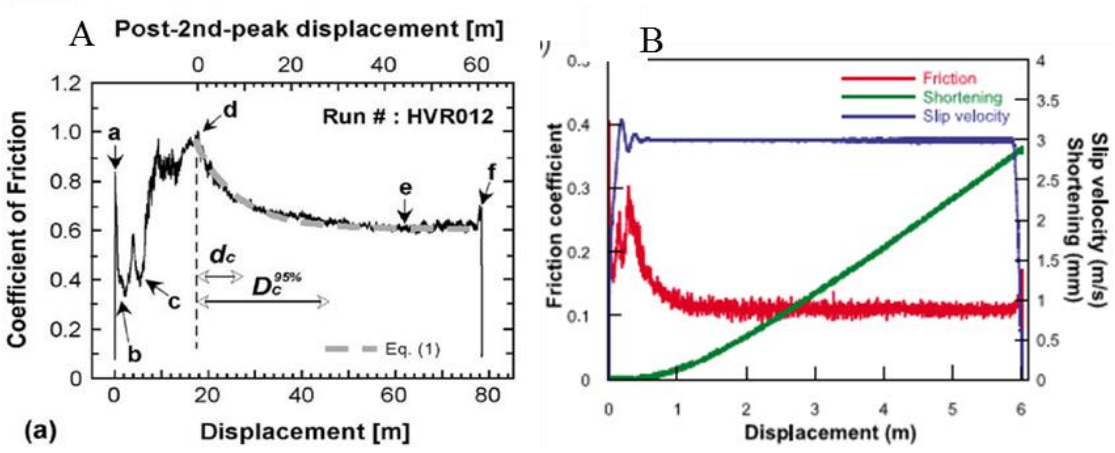

Figure 31. Examples of frictional melt on gabbro. A. Friction-distance curve for gabbro sample sheared at normal stress of 1.4 MPa, equivalent velocity of 0.85 m/s, and total slip of 78.65 m. Note the initial weakening from a to b, the transient strengthening from c to d, and the exponential decay from d to e. Peak strength occurred at d, corresponding to the onset of visible frictional melt covering whole fault. Adapted from Hirose and Shimamoto (2005). B. Friction (red), sample shortening (green), and slip velocity (blue) as functions of slip distance for the gabbro sample sheared at normal stress of 20 MPa, slip velocity of 3 m/s, and total slip of 6 m from Niemeijer et al. (2011).

Recently, Brown and Fialko (2012) investigated gabbro melting at moderate slip velocities of a few tens of cm/s. They found that the experimental faults switch from high friction to weakening with the formation of melt streaks, which they termed as 'melt-welt'. They proposed that this partial melt induced the weakening by temporarily acts against the normal load by local volumetric expansion, and by doing so reduces the normal load on rest of the fault leading to an overall lower friction. We found similarities between this behavior and granite melting, as discussed later.

Finally, the dependence of friction on slip velocity for granitic rocks showed a complex weakening-strengthening-weakening evolution (Reches and Lockner, 2010; Mizoguchi and Fukuyama, 2010; Kuwano and Hatano, 2011; Liao and Reches, 2012). This evolution was attributed either to granular dynamics (Kuwano and Hatano, 2010) or to dehydration of thin water layer of gouge particles (Sammis et al., 2011). The present analysis of granite melting provides more plausible explanation to the strengthening of granite at slip velocity > 0.1 m/s.

Microstructure Observations

The ROGA group conducted hundreds of experiments on granite group samples including Sierra white granite (SWG), Charcoal Black diorite (CBD), and Radiant red granite (RRG). I examined these tests and selected experiments with the following properties: (1) long slip distances of over 5 m, (2) moderate velocities of a few cm/s, and (2) occurrence of initial weakening followed by transition to strengthening. The selected experiments are listed in Table 4.

I discovered that experimental granitic faults undergo local melting through systematic SEM examination of cohesive crust flakes that developed during the experiments. The flakes are similar appearance as the flakes shown in Chapter 4. They are curved with shiny top surface, contain visible slickenside striations, and detached from the rock base. Melt features were observed mostly on flake surfaces with dense striation patterns and smooth tops. A distinct set of features was observed from experiment SWG 1592 (Table 4). The general view of the top of fault surface on a cohesive flake (Fig. 32A) displayed smoother areas in the center zone with visible striation patterns in E-W directions and the rougher edges along top and bottom with

flipped-over wedges of material indicative of stick slip events. An enlarged view of the zone of striations showed individual striations and horizons at different levels between striation bands (Fig. 32B). Note the concentric striations and elevated horizons within bands of striations. The fault surface is composed of a highly porous structure with large portion of the 3D matrix composed of melt (Fig. 32C-E). Melt features such as stretching of melt drops along slip direction (Fig. 32C, E), flattening of melts (Fig. 32B, D), and melt stretching in a form of simple shear (Fig. 32D) can be seen. Some highly stretched melts even formed micro-size glassy fibers (Fig. 32E).

The melt features appearing in the granite flake surface are different from the bulk melt as in the high speed experiments on gabbro in the following features: (1) the structure is a highly porous 3D structure, (2) melt features were highly-localized on areas of the principal slip surface and penetrated into depth of a few μm, as estimated from the porous structure (Fig. 32A, C, E), and (3) even in the areas with melt, the micro-structure reflects a mixture of melt and unmelted grains (Fig. 32B-E).

We found that the melting of the granite fault is not only a phase transition of the fault gouge, but also a "mechanical phase transition" (Mourchid et al., 1995; Shibayama et al., 1994) from a weakening stage to a strengthening stage as described below.

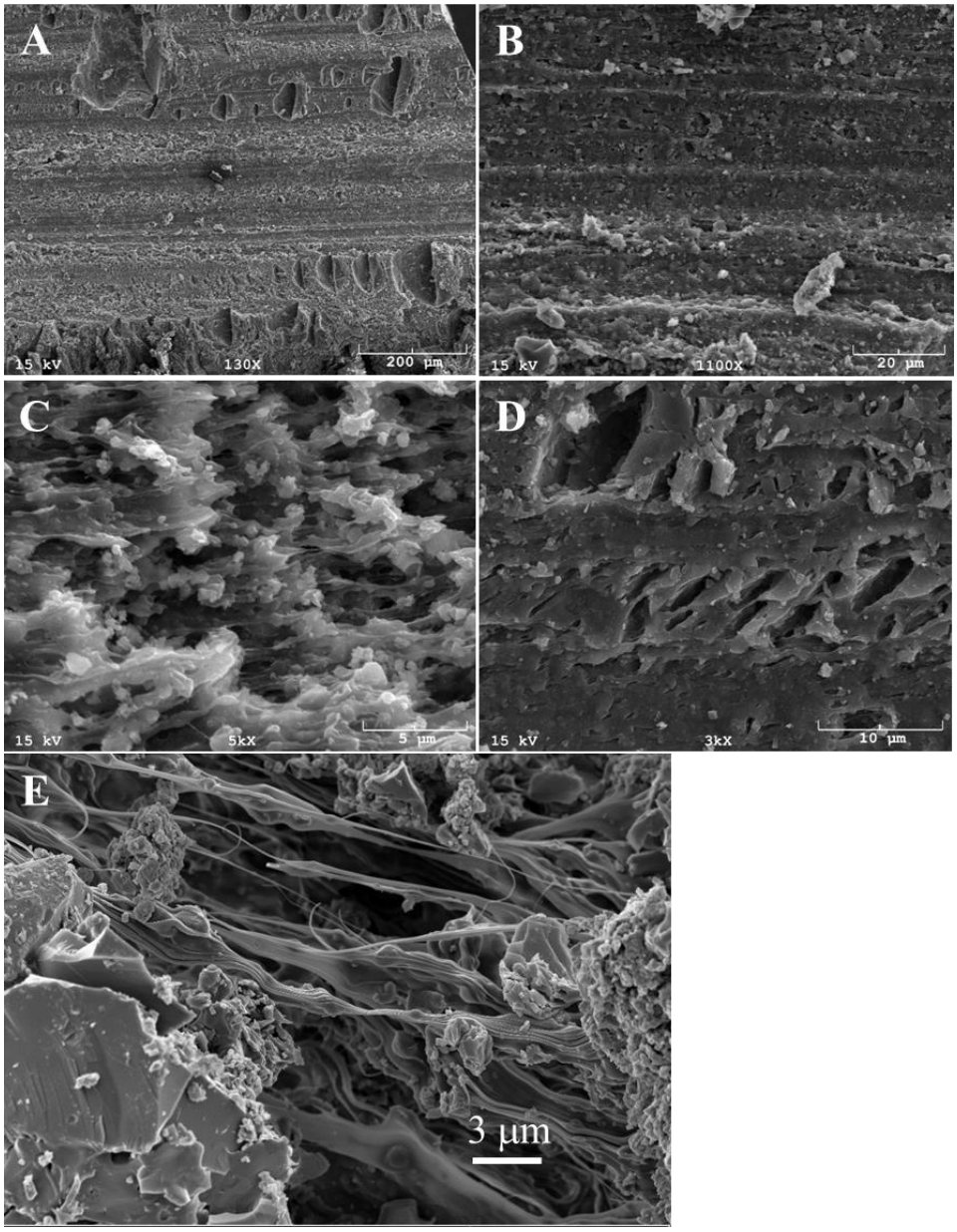

Figure 32. Microstructural observations of post SWG 1592 products with SEM. A. General view of the top of fault surface in a cohesive flake, with visible striation patterns from left to right and the rougher edges in top and bottom. B. Enlarged view of the zone of striations. Note the concentric striations and horizons within bands of striations. C. Magnified view of the striation zone with highly porous structure. Note the stretching of melt drops along slip direction, and visible sub-micron grains embedded within and attached to melt drops. D. Striation zone close-up view. Note the flattening on the melt top and stretched melt similar to the simple shear structure. E. Sub-micron glassy fibers in the close-up view, note solid grains attached to the fibers in the center and larger fractured grains in the lower left.

Mechanical results

Friction experiment results

Figure 33 displays the evolution of friction coefficient with slip distance in experiment for SWG 250, 290, 510_A, 720, 1551, and 1592 (sheared at ~ 4.7 cm/s, σn = 1-2.33 MPa), and for diorite 1313, 1315, and 1320 (V ~1 cm/s, σn = 2.43-2.6 MPa). Detailed, typical evolution of friction coefficient, temperature, and dilation with slip distance for SWG 1592 is shown in Fig. 34.

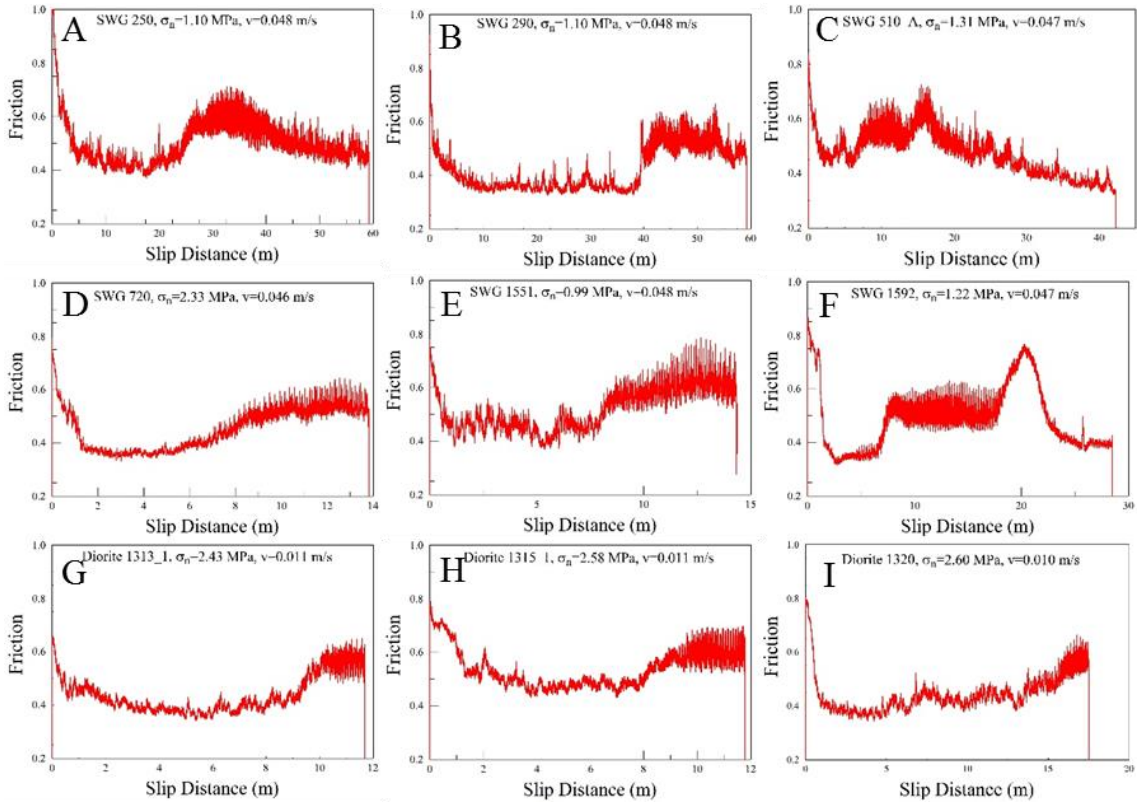

Figure 33. Summary of friction-distance curves for SWG and diorite runs at constant velocities. Experiment #, normal stress, and slip velocity are shown in the text box inside each plot. The transition from initial weakening to transient strengthening can be seen in these cases. A final weakening stage followed the transient strengthening can be seen in cases A, C, and F.

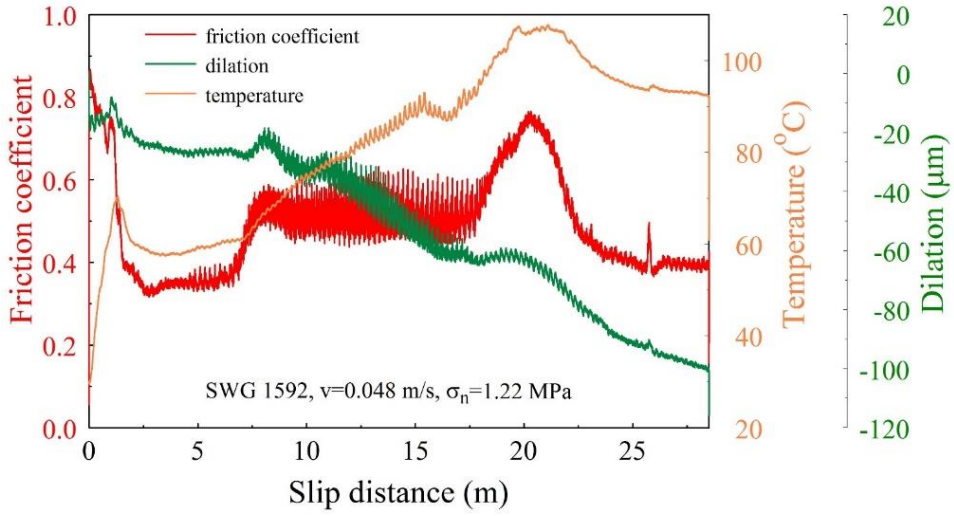

Figure 34. Friction, temperature, and dilation as a function of slip distance for sierra white granite run 1592. Initial weakening tended to stabilize after 2 m of slip, and the strengthening transition started at ~8 m. The peak friction occurred at ~21 m followed with a decay of friction until a stable value of 0.4. The temperature increased from 23 ℃ to 110 ℃ and dropped to 93℃ in the end. Wear was small in the initial weakening stage, but increased in the strengthening period. Note the wider and spikier friction response in the strengthening period, and the temporal dilation accompanied with friction strengthening.

The typical friction-distance relations in Figs. 33 and 34, indicate the following stages of friction evolution:

1. Initial weakening from static friction of μ_s =0.75-0.85 to steady value of μ_w = 0.3-0.5 after slip of the first few meters. The initial weakening stage commonly accompany with the stabilization of dilation (Fig. 34) during friction stabilization that indicates reduction of the wear-rate during steady state run (Boneh et al., 2014). The steady-state friction values in the initial weakening period during the first few meters of slip are about 0.3-0.45 for SWG, which is in good agreement with the friction-velocity curves derived in Reches and Lockner (2010).
2. A strengthening transition from low friction to a high friction stage after slip of ~7 m up to 40 m (Fig. 33). The strengthening periods have spikier friction curves

(Fig. 33), and fast wear rate as compared to the initial weakening period (Fig. 34). The weakening-strengthening transition also accompanied with a temporary normal expansion (small peak in the dilation curve at ~8 m in Fig. 34).

3. In some cases, a second weakening stage may appear, with gradually decrease of friction with slip distance from a peak value to the steady state (Figs. 33A, C, F).

Phase-transition of weakening-strengthening

We interpret the above observations as indicating that the melting of the granite fault is not only a melting phase transition of the fault gouge, but also a "mechanical phase transition" (Mourchid et al., 1995; Shibayama et al., 1994) from a weakening stage to a strengthening stage (Figs. 33-34). This mechanical transition is also associated with events of temporary increase of both normal and shear stresses. Fig. 35 displays these stress change events in nine experiments (the same as in Fig. 33) in which the normal stress increased by 0.4%-2% of the ambient stress, and the shear stress increase by 33%-56%. This difference in the intensity of the stress increases, led to the 32%-79% increase of friction coefficient (Figs. 33, 34). Similar stress change events were also observed in the gabbro melt-welt experiments as discussed later.

We noticed that the distance required for the mechanical phase transition was related to both the slip velocity and normal stress (table 4). For example, SWG 3401, 3402, and 3404 have the same normal stress (3.9 MPa), and the distance required for transition is longer for smaller velocity and shorter for higher velocity. SWG 250, 720, and 3401

have the same velocity (~4.5 cm/s), and the transition distance is shorter for higher normal stress and vice versa.

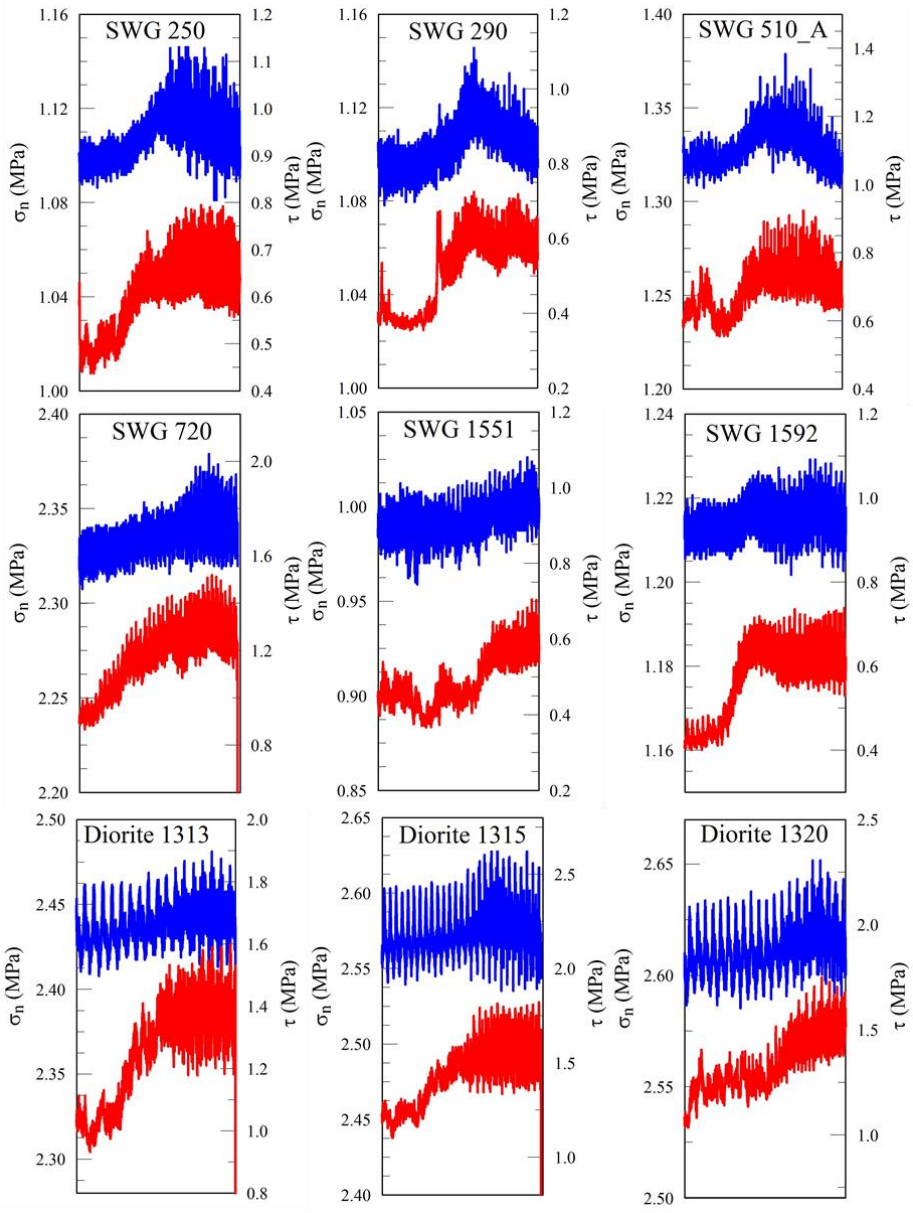

Figure 35. Normal stress (blue, left axis) and shear stress (red, right axis) response during the transition from initial weakening to the strengthening period for both granite and diorite. Note the systematic temporal increase of normal stress and shear stress during the transition.

To account for both normal stress and slip velocity, we use the 'dissipative-power-density', PD, that has units of MW/m^2, namely power per unit area of the fault,

PD = [shear stress] × [slip velocity].

The use of PD is effective in quantification of energy dependent friction processes as demonstrated by Boneh et al. (2013). As the shear stress changes during most runs (Figs. 33, 34), we calculated the average PD_A, from the run initiation to the transition step by

$$PD_A = \frac{\int_0^{t_C} \tau(t) \cdot v(t) \cdot dt}{t_c} = \frac{\int_0^{L_{WS}} \tau(L) \cdot dL}{t_c}$$

where $\tau(t)$ is the shear stress as a function of time, $\tau(L)$ is the shear stress as a function of slip distance, t_c is the time been used until the weakening-strengthening transition, and L_{WS} is the slip distance to the weakening-strengthening transition (see Table 4). In our experiments with Sierra white granite, diorite, and Radiant red granite, the distance L_{WS} to the weakening-strengthening is a clear function of PD_A with power law relationship (Fig. 36).

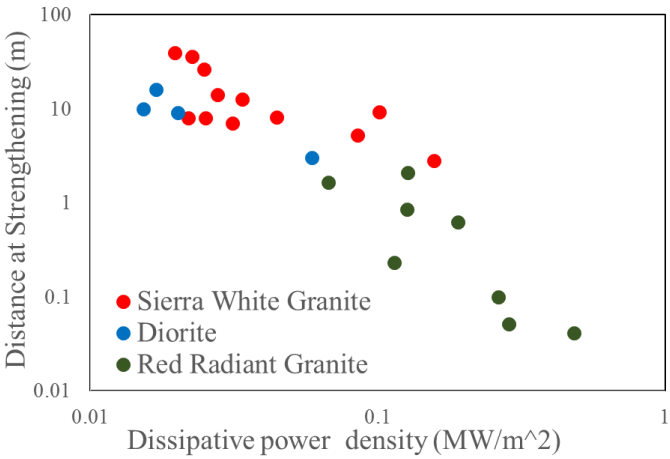

Figure 36. Slip distance required until weakening-strengthening transition as a function of dissipative power density in log-log scale. Note the general power law relationship showing the higher the dissipated power density the shorter the distance required for strengthening.

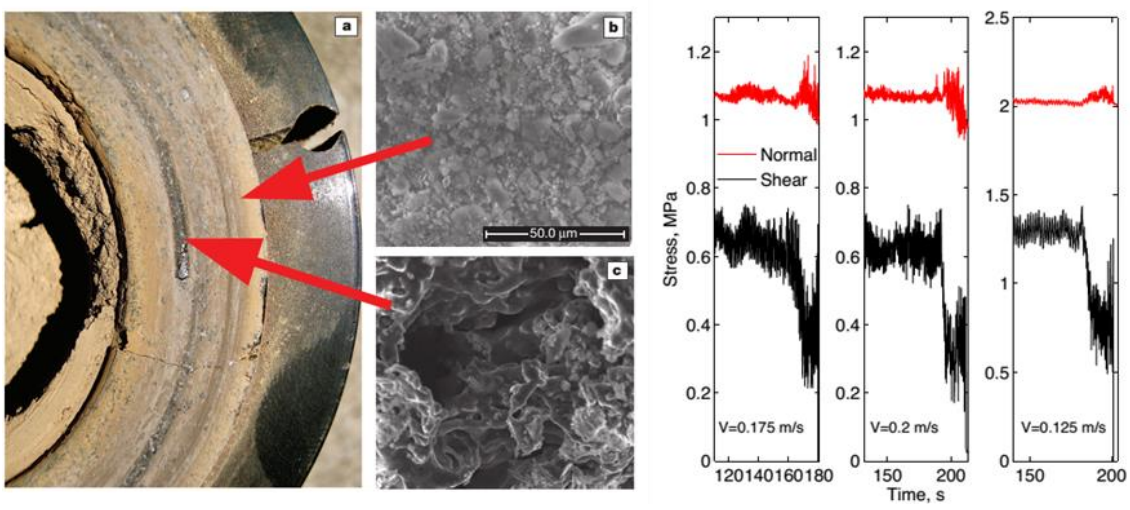

Figure 37. Left: Initiation of melt streaks formation with gabbro under normal stress of 4 MPa, velocity of 6.5 cm/s, and slip distance of 9.5 meters. Note the two SEM images to the right showing melting on dark streaks and non-melt on surfaces with gouge powder. Right: Three examples of the gabbro friction experiments showing the initiation of weakening was accompanied with the transient increase of normal stress, indicative of volumetric expansion against the normal stress. Adapted from Brown and Fialko (2012).

Discussion

Melt-welt: Weakening in gabbro and Strengthening in granite

Brown and Fialko (2012) recently reported the systematic dynamic weakening in gabbro experiments sheared at moderate velocities (a few cm/s to 30 cm/s), and low normal stresses (1-3 MPa). The weakening occurred when gouge particles melt locally and formed streaks of melt along the fault zone (Fig. 37 left). This phase transition induced volume increase that was large enough to generate a transient increase of dilation and normal stress (Fig. 37 right). Surprisingly, this increase of the normal stress led to reduction of the shear stress rather than the expected increase. The authors suggested that the local melt-welt streaks temporally unload the fault at large, and by doing so reduced the frictional contacts and the overall frictional resistance.

This behavior in the gabbro experiments bears some similarities to our granitic experiments. The temporary increases of the normal stress and dilation of Brown and Fialko (2012) during the weakening transition are similar to our observations of these two parameters during the strengthening stage (compare Fig. 37 and Fig. 33, 34). However, in the granitic rocks the transition is from weakening to strengthening, whereas in the gabbro faults the transition is from high friction to low friction. This difference reflects the difference of velocity dependence between these two lithologies at moderate slip-velocity of 5-30 cm/c. In this velocity range, the steady-state friction coefficient of gabbro is high, μ_s = 0.6 and 0.8, e.g, Tsutsumi and Shimamoto (1997), and Brown and Fialko (2012) (Fig. 38). On the other hand, friction-velocity relationships for granite rocks display low steady-state friction, μ_s = 0.3-0.4, at velocity ranges of a few cm/s (Reches and Lockner, 2010; Di Toro et al., 2011), in agreement with the present results (Figs. 33-34). When a gabbro fault enters the phase transition and starts to form melt streaks (Fig. 37), it has high friction of μ_s = 0.6-0.8, and we assume that it weakens by the mechanism suggested above by Brown and Fialko (2012). When a granite fault enters the phase transition, it is already very weak, μ_s ~ 0.3, due, for example to powder rolling (Chapter 4) or powder lubrication in general (Reches and Lockner, 2010). We propose that the strengthening of the granite during the phase transition is due to "viscous breaking" effect, arises from resistance of the melt patches from smearing, as proposed by Hirose and Shimamoto (2005) and mentioned in the Introduction (Fig. 31A). We assume that the gabbro weakening and the granite strengthening both reflect a phase transition from solid gouge particles to local melt streaks.

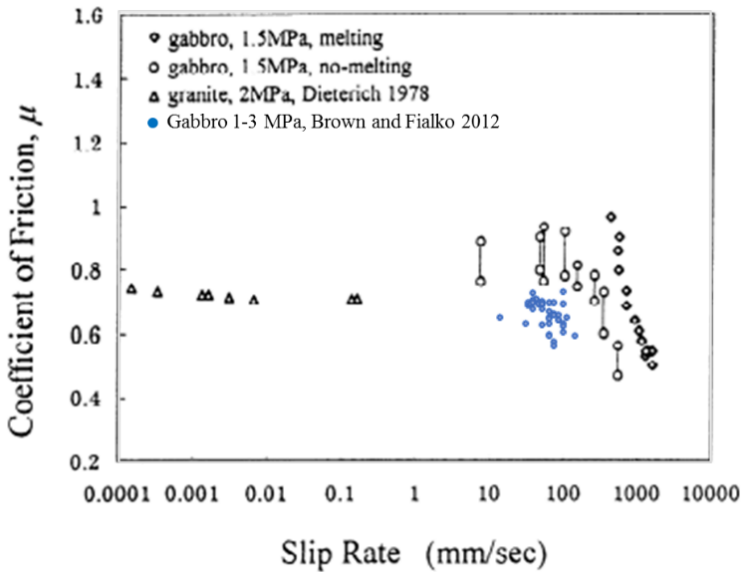

Figure 38. Steady-state friction coefficient as a function of slip rate for gabbro, from TsuTsumi and Shimamoto (1997) and Brown and Fialko (2012). Note the friction coefficient at velocity ranges of 5-30 cm/s is about 0.6-0.8.

Based on the above observations and assumptions, we now compare our results of slip distance, $L_{WS,}$ required to reach the mechanical phase transition (weakening-to-strengthening) to the (Fig. 36), to the equivalent transition (strong-to-weak) in the gabbro experiments of Brown and Fialko (2012). Fig. 39 displays L_{WS} as function of the integrated PD (equation above) for granite and gabbro and the equivalent in gabbro. Both lithologies show power law dependence between slip distance and power-density in the present range of dissipative power density (0.01-1 MW/m^2). The gabbro transition trend is above the granite/diorite transition line, and has a steeper slope. This indicates that for a given dissipative power density, gabbro needs longer slip distance to reach the transition relatively to granite/diorite. In other words, under the same normal stress and slip velocity, a granite fault is likely to reach the phase transition before a gabbro fault.

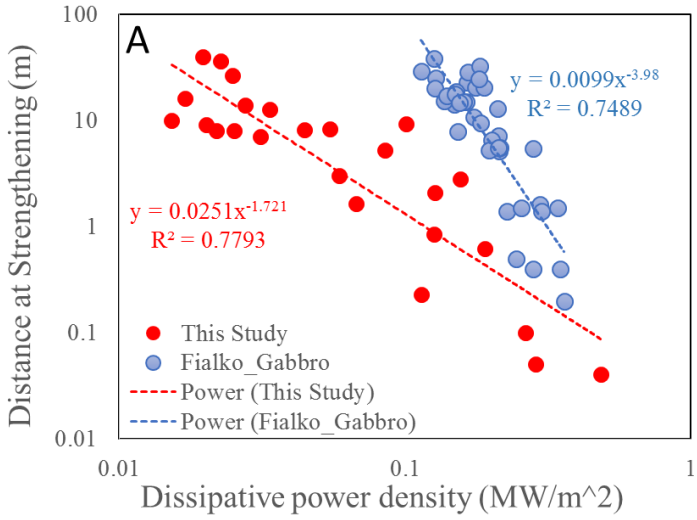

Figure 39. Cumulative distance until the weakening-strengthening transition as a function of dissipative power density (A) and elapsed time till weakening-strengthening transition as a function of dissipative power density (B). Blue data are from gabbro weakening transition by Brown and Fialko (2012). Note the consistency in power law dependence and slope variation in both cases.

A conceptual model for frictional strength evolution of granite faults

The evolution of granite friction coefficient with slip at moderate velocity ranges of a few cm/s can be summarized as follows (Fig. 40A):

Stage I: Initial stage, high friction, small amount of poorly organized gouge.

Stage II: Initial weakening. The characteristics of this stage is the formation of cohesive gouge flakes and generation of powder rolls on PSZ surface, with a stabilization of wear (Fig. 34) by the protective effect of the PSZ. The weakening mechanism is powder rolling.

Stage III: Transient strengthening. The characteristic of this stage is the spikier friction response (Figs. 33-34), humps in the responses of normal stress and dilation (Fig. 34-35), and a power law dependence of transition distance with respect to the

power density (Fig. 39). The mechanism for this strengthening is viscous braking by local melting.

Stage IV: Final weakening with the spread of melting leading to overall lubrication. Features in this stage is a peak friction followed with an exponential decay, and observation of partial melt on fault surfaces (Fig. 32).

A striking observation is the similarity of the friction evolution during granite fault slip at moderate velocity (Fig. 40A), and the equivalent evolution in gabbro fault slip at high-velocity (Fig. 40B). Stages I-II in the granite correspond to stage a-b-c of the gabbro, and the strengthening for the transition from II to III in the granite, fits stage c-d in the gabbro. Also the final weakening stage IV in the granite is similar to the gabbro bulk melt (stage e in Fig. 40B) such as the shape of a peak friction followed by a quasi-exponential decay of the frictional strength. However, the high-speed experiments on gabbro generate continuous and visible melt layer while our moderate speed runs generated only partial-melting layer without any observation of melt extrusion during the experiment (Fig. 32). This can be explained by the fact the strength of a partial-molten gouge starts to decrease when the melt fraction exceeds ~50% (Fialko et al., 2005; Rosenberg and Handy, 2005). The power density in our experiments is too low to reach bulk melting; however, intense slip localization could potentially lead to melt of thin zones within the gouge, as suggested by the microstructural images (Fig. 32). Further, the intense grain size reduction to tens of nanometers, reduces the melting temperature could also contribute to the melting at such low power inputs and low temperature.

Finally, we also noted a striking similarity between the friction evolution with slip distance at constant velocity (Fig. 40A), and the dependence of steady-state friction coefficient on slip velocity, as documented by Reches and Lockner (2010).

They noted systematic drop of the steady-state friction coefficient as the slip velocity increases up to about V~ 0.05 m/s, and weakening changed into strengthening at higher velocities (Fig. 40C). They and Sammis et al. (2011) attributed this transition to dehydration of water coating the nano-size gouge particles. We suggest that the present observations of local melting of granite and the proposed model explain the puzzling velocity strengthening of granite faults by attributing it to the local melting as discussed above. The model of Reches and Lockner (2010, Fig. 5) was modified (Fig. 40 D) to fit our four stage model presented above.

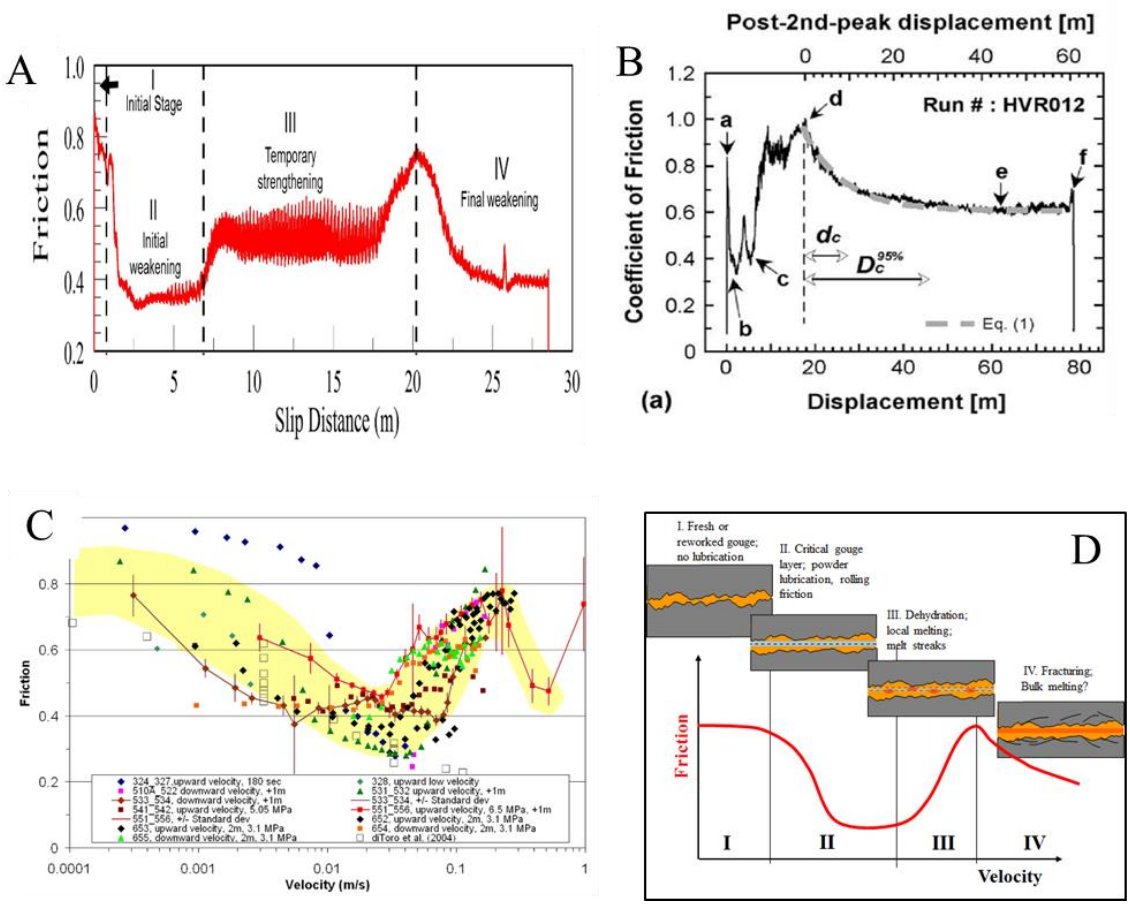

Figure 40. A. The evolution of friction coefficient as a function of slip for granite rock sheared at moderate velocity. Data from SWG run 1592 with normal stress of 1.22 MPa and constant slip rate of 4.8 cm/s. Four regions can be categorized as Initial stage, initial weakening, transient strengthening, and final weakening. B. Friction-distance curve for gabbro sample sheared at normal stress of 1.4 MPa, equivalent velocity of 0.85 m/s, and total slip of 78.65 m (same as Fig. 31). Note the similarity between A and B. C. Friction versus slip velocity. Experimental friction values for 35 runs with 254values; each dot is the average friction value at a velocity interval; standard deviation bars are shown only for two runs for sake of clarity; yellow shading bound the data without outliers. D. A proposed model, modified after Reches and Lockner (2010) for friction-velocity relation of a granite fault. Stage I. Initial setting, initial wear, no lubrication; Stage II. Cumulative wear, critical gouge layer and powder rolling lubrication; Stage III. Local melting leading to strengthening; Stage IV. Final weakening, possible bulk melting of the fault zone.

Supplementary information

Rock samples composition

Friction experiments were performed with solid blocks of Sierra White granite, Radiant red granite, and Charcoal black diorite. These rocks have been under multiple runs with cumulative slip distance of hundreds of meters. Composition and physical constants are listed below.

Radiant Red granite (RRG) (Commercial name). Sample supplier: ColdSpringGranite, TX. Properties by supplier: Quarried at Fredricksburg, TX; Bulk density = 2614 kg/m^3; Uniaxial strength = 146.5 MPa. Our powder XRD analysis shows four main minerals: quartz (43.6%), albite (19.7%), microcline (22.8%), and biotite (13.9%), in weight percent.

Charcoal Black diorite (CBD) (Commercial name). Sample supplier: ColdSpringGranite, TX. Properties by supplier: Quarried at St. Cloud, Minnesota; Bulk density = 2723 kg/m^3; Uniaxial strength =173.9 MPa. Our powder XRD analysis shows quartz (16.7%), feldspar (59.5%), albite (32.7%), and microcline (26.8%), amphibole (7.2%), and biotite (16.7%).

Sierra White granite (tonalite) (SWG) (Commercial name is granite but actual lithology is tonalite). Sample supplier: ColdSpringGranite, TX. Properties by supplier: Quarried at Raymond, California; Bulk density = 2641 kg/m^3; Uniaxial strength =118.5 MPa. The electron-microprobe (EPMA) modal analysis shows six main minerals in this rock: plagioclase (48%), quartz (38%), alkali-feldspar (5%), ferromagnesian- mica (5%), and muscovite (5%). Mean grain size is about 0.3 mm; mean void space in EPMA images is ~4%.

Table 4. Experimental conditions of the experiments for diorite and granites with weakening-strengthening transition.

Sample & Exp#	σn (MPa)	Total slip (m)	Velocity (m/s)	Weakening-strengthening transition		
				L_{WS}, Slip distance (m)	T_C, Time (s)	PD_A, Dissipative power density (MW/m^2)
SWG 1592	1.22	28.50	0.047	8.0	169	0.025
SWG 1551	0.99	14.35	0.048	8.0	168	0.022
SWG 720	2.33	13.82	0.046	8.1	177	0.044
SWG 250	1.10	59.30	0.048	26.3	552	0.025
SWG 290	1.10	59.34	0.048	39.5	831	0.020
SWG 330	1.13	58.77	0.047	36.0	765	0.023
SWG 510_A	1.31	42.22	0.047	7.0	149	0.031
SWG 3408	2.39	34.06	0.068	9.2	135	0.101
SWG 3407	2.30	27.30	0.045	12.6	274	0.034
SWG 3404	3.85	14.65	0.073	2.8	38	0.157
SWG 3402	3.90	16.10	0.025	14.0	573	0.028
SWG 3401	3.92	16.06	0.049	5.2	107	0.085
Diorite 1304_3	2.19	11.67	0.045	3.0	76	0.059
Diorite 1313_1	2.43	11.67	0.011	10.0	1030	0.015
Diorite 1315_1	2.58	11.77	0.011	9.1	929	0.020
Diorite 1320	2.60	17.47	0.010	16.0	1650	0.017
RRG 3258	1.19	2.96	0.111	1.6	15	0.067
RRG 3249	5.58	1.39	0.036	0.85	25	0.126
RRG 3244	2.13	1.64	0.115	0.23	3	0.114
RRG 2835	2.64	3.93	0.096	2.1	22	0.127
RRG 2851	6.84	2.43	0.048	0.62	13	0.190
RRG 2838	2.66	2.60	0.289	0.05	0.6	0.286
RRG 3245	2.13	1.79	0.326	0.10	0.8	0.263
RRG 2855	6.60	2.09	0.193	0.04	0.7	0.483

Chapter 6: Shear experiments of confined gouge

Approach

In this section, I used the terms ‘gouge’, ‘granular’, ‘grains’ and ‘powder’ interchangeably while they all mean ‘**incohesive granular material’,** unless otherwise specified.

The analyses presented in Chapter 3-5 focused on experimental faults made of solid rock blocks. Fault slip is always associated with pulverization and the formation of gine-grain gouge zone (BenZion and Sammis, 2003), as shown in the above experiments, all previous rock shear experiments (for summary see Reches and Lockner, 2010), and natural fault-zones (e.g., Wilson et al., 2005). The shear mechanics of a gouge layer can be experimentally tested in ROGA independent of the rock or mineral source by using the apparatus component, termed Confined ROtary Cell (CROC). CROC, which was described in Chapter 2, is capable of shearing 3 mm thick, ring shape gouge sample made of granular or powder material. The sample is confined and can be sheared at the full capacity of ROGA (Chapter 2). This section summarizes my preliminary results of gouge experiments with CROC. The starting materials were ground minerals or rocks including talc, ooids, dolomite, and gypsum. The present analysis presents the mechanical data of the friction, dilation-compaction, as well as microscopic characterization of structure and mineralogy. The experimental results are compared with solid rock experiments, highlighting the similarities and uniqueness of powder behavior.

One common observation in all CROC experiments is that the grain-size of the starting granular material was further reduced to nano-scale by continuous

pulverization, regardless of the initial grain-size or material type. In many cases, the localized slip-surfaces that developed in the gouge layer were strikingly similar to their equivalent in the solid rock experiments.

Talc gouge shear experiments

Mechanical data

Talc shear experiments were conducted on ground pure talc (>99%) and I used the fraction with grain size smaller than 150 μm. Experiments were run on either room-dry powder (referred to as 'dry') or samples with 20 wt% distilled water (referred to as 'wet'). Most of the experiments were run is stepping velocity style with a typical history of a single run includes two cycles of velocity loading with steps of 0.002, 0.006, and 0.018 m/s (or 0.018 m/s, 0.054 m/s, and 0.16 m/s in the high velocity modes).

The evolutions of the friction coefficient and slip-velocity as a function of slip distance are plotted in Fig. 41 for wet and dry talc. These data demonstrate: (1) wet talc has an overall low steady-state friction coefficient, μ_{ss} = 0.15-0.2, whereas the dry talc displays μ_{ss} =0.3-0.45; (2) the dry talc displays slip strengthening at all three velocity ranges, whereas only slight slip weakening occurred in the wet talc; (3) velocity-strengthening appears in both dry and wet talc runs.

The velocity dependence of the steady-state friction coefficient of talc in the present 19 runs (114 velocity-friction pairs) is summarized in Fig. 42. Slip velocities range between 0.001 m/s and 0.16 m/s, and the data are divided into three groups according to their slip distances: Very-short (slip ~ 0.06 m), Short (slip ~0.6 m), and Very-long (slip ~ 6.5m). The following features are noted:

(1) Wet talc powders have low friction, μ_{ss}= 0.1-0.2, with slight strengthening with slip distance and slip velocity.

(2) Distinct velocity-strengthening in dry talc, and gentler velocity strengthening in wet talc.

(3) Clear slip strengthening in dry powders, while no slip strengthening in wet powder.

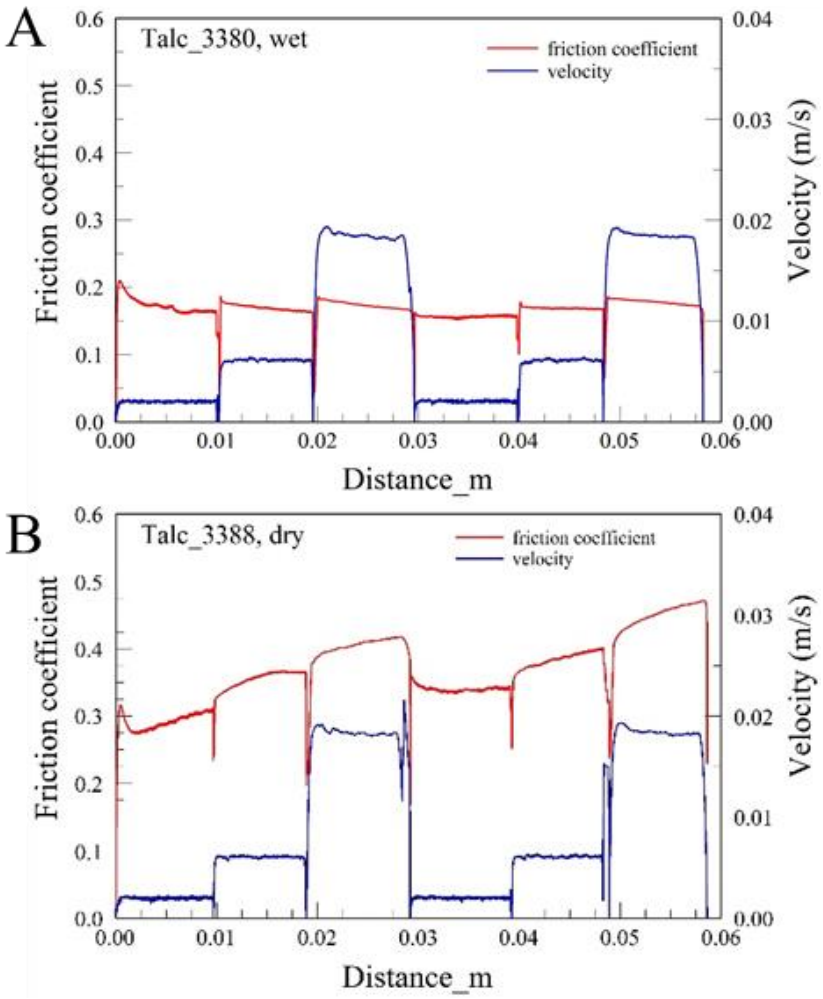

Figure 41. Friction (red) and velocity (blue) as a function of slip distances for talc run 3380 (A) and 3388 (B). Velocity values are 0.002 m/s, 0.06 m/s, and 0.018 m/s. Displacements are 0.01 m per stage; normal stress was 3.3 MPa

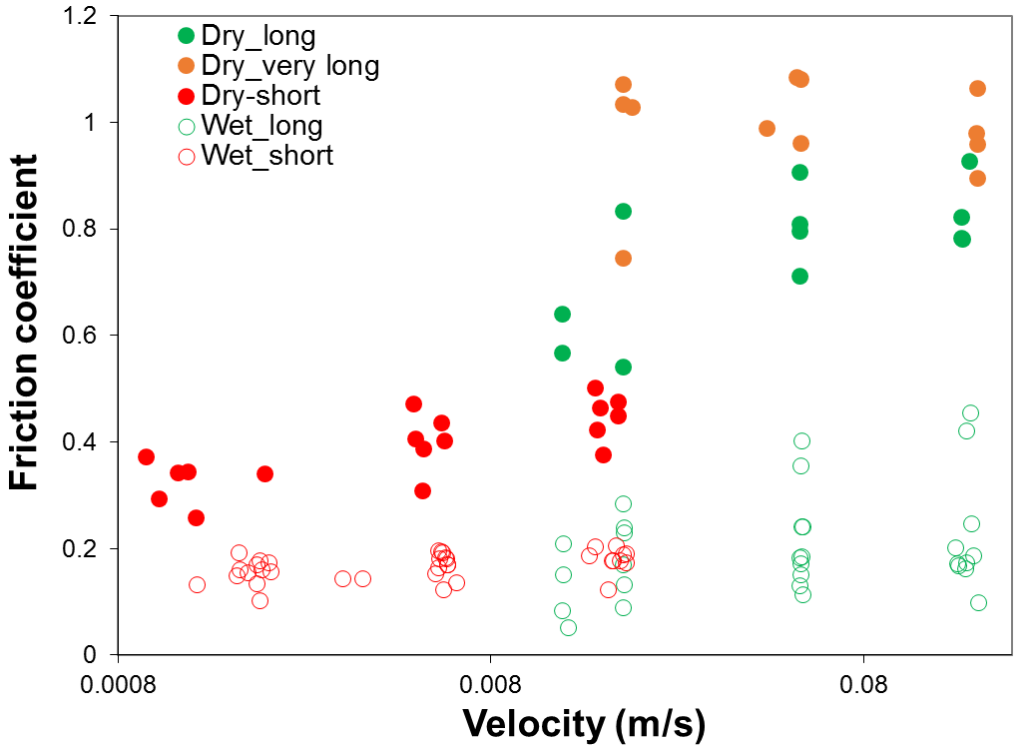

Figure 42. Friction coefficient as a function of slip velocity for both dry (solid circle) and wet (hollow circle) talc powder runs; 19 experiments with 114 velocity-friction pairs. Note the low friction value of wet talc compared to dry talc, and the consistent velocity strengthening in dry talc.

One important characteristics of talc is its dilation/compaction evolution during shear. In the CROC cell, the initial stage of each run is always associated with compaction that is the sum of two processes: (1) real compaction of the powder, and (2) flow of the loose powder from its ring-shaped chamber into the flexible seal space (Fig. 7, Chapter 2). It is estimated that process (2) is active only during the first velocity step of each run (Fig. 43). Commonly, wet talc displays compaction (negative dilation) associated with the shear (Fig. 43A), whereas dry talc experienced extensive dilation after a few cm of displacement (Fig. 43B). As seen in the post-shear structure of the talc fault zone (Fig. 44), the macroscopic dilation is associated with extensively developed

sets of Riedel shears across the whole gouge layer, and it appears that the dilation is due to thrusting along the Riedel shear surfaces.

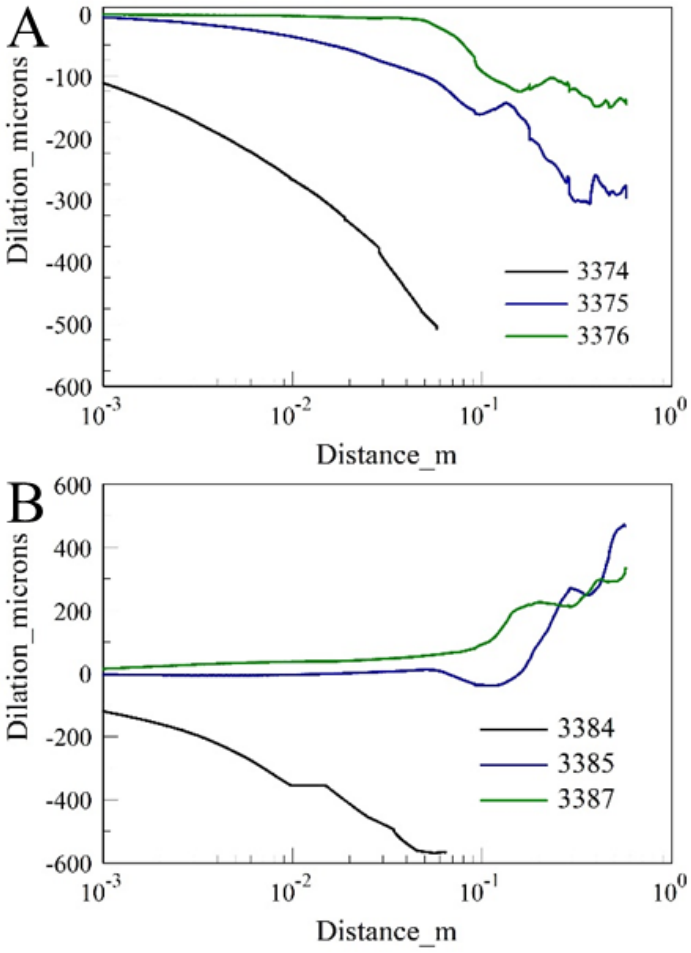

Figure 43. Fault-normal dilation as a function of slip distance (log scale) for wet (A) and dry (B) talc. Each plot contains a set of runs for the same sample. Velocity were at 0.002 m/s, 0.006 m/s, and 0.018 m/s. Normal stress was 3.3 MPa. Wet talc runs show, after the initial large compaction, decreased compaction rates but no dilation. Dry talc runs show, after initial large compaction, compaction rate decrease that eventually switched to dilation.



Figure 44. Side view of the dry talc powder sheared at velocity of 0.002 m/s and normal stress of 2.6 MPa for 3.5 m. Note the through-cutting Riedel shears within the talc powders.

Microstructural observations

Slip localization along thin, principal slip zone (PSZ in Chapter 4), which are recognized by well-developed surfaces is common in both dry and wet talc fault surfaces (Fig. 45). These surfaces were collected and examined using high resolution SEM. In the SEM images, the dry talc fault surfaces appeared rough and bumpy (Fig. 45A), whereas the wet talc surfaces have smoother appearance (Fig. 45B). Close up views showed that the dry talc sample experienced significant grain size reduction by crushing, and the smaller submicron size grains filled large portion of the open spaces (Fig. 45C). For wet talc powder, the fault structure is composed of stacking of flakes with only limited breaking or fracturing of talc flakes (Fig. 45D).

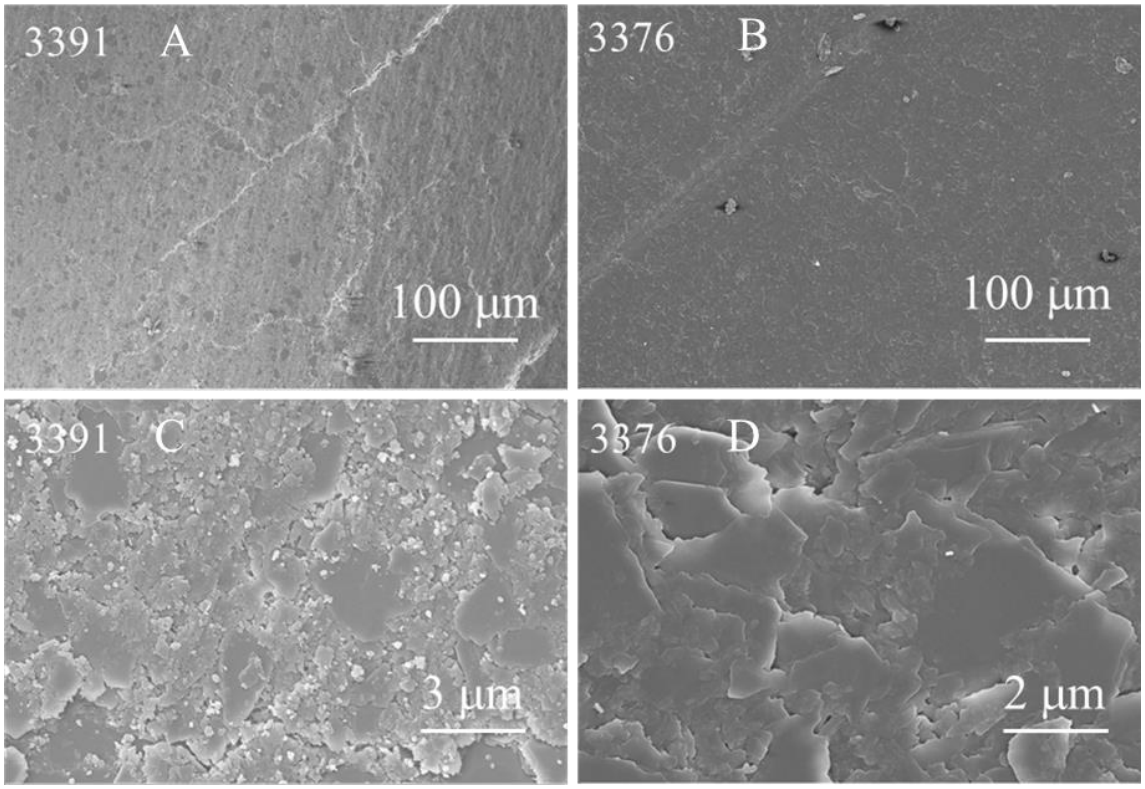

Figure 45. SEM images for the dry (3391) and wet (3376) talc powder fault surfaces developed after shearing experiments. Both faults showed well-developed fault plane. Note small submicron grains in dry talc surfaces, while few submicron grains in wet talc surfaces

Shear of dolomite and ooid grains

The micro-structural observations of four shear experiments with Kasota dolomite (KD) grains (grain size 150-250 μm) and ooid grains (original spherical grains ~250 μm) are presented here. Dolomite grains were sheared at v =0.4 m/s, σ_n = 3.5 MPa (run 3160), and v=1 m/s, σ_n = 3.6 MPa (run 3165), and ooid grains were sheared at velocity of 1 m/s, σ_n = 3.6 MPa (run 3169) and 0.8 m/s, σ_n = 3.6 MPa (run 3196). The initial composition of the ooids is calcite (92%), as confirmed with the XRD analysis.

Cross-section features

Cross sectional views of shear gouge were made by epoxying and cutting the material perpendicular to the fault planes. The sections normal to slip direction display arc shaped, shiny, zone of localized shear in both the dolomite gouge (color change in Fig. 46A, similar to solid dolomite experiments) and the grain comminution zone of the ooid grains (Fig. 46B). Sections along slip direction exposed bands of porous structures beneath the shiny crust, and fractures deep into the crust indicated by the better penetration of epoxy (Fig. 46C).

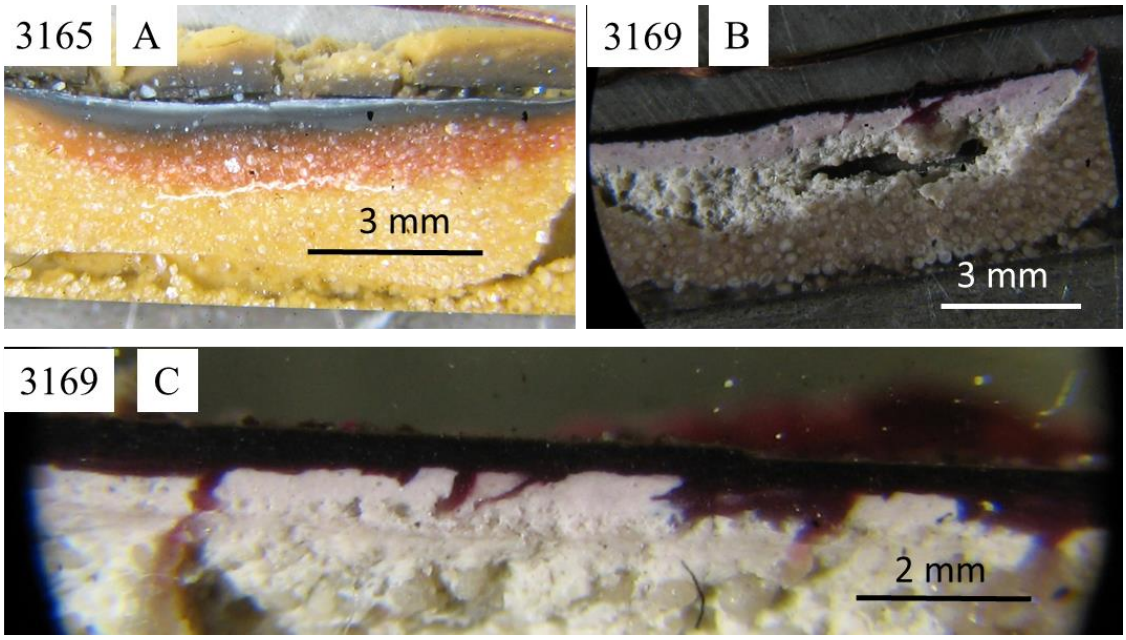

Figure 46. Cross section view of the fault zones. A. dolomite gouge 3165, cut normal to slip direction. B. Ooid grains 3169, cut normal to slip. C. Ooid grains 3169, cut along slip direction.

High-resolution SEM image of the cross-sections showed distinct features: (1) A crust of ~0.5 μm thick that was composed of tightly compacted nano-grains (Fig. 47A); (2) the grains beneath the crust were coarser with open, porous structure (Fig. 47A-D);

and (3) bands of coarser grains imbedded within the finer grains cut along slip direction (Fig. 47B, C). These bands are “channel”-like structures were similar to the highly porous bands beneath solid rock faults (Fig. 47E). Their inclination indicate that these bands are probably Riedel shears inside the gouge layer.

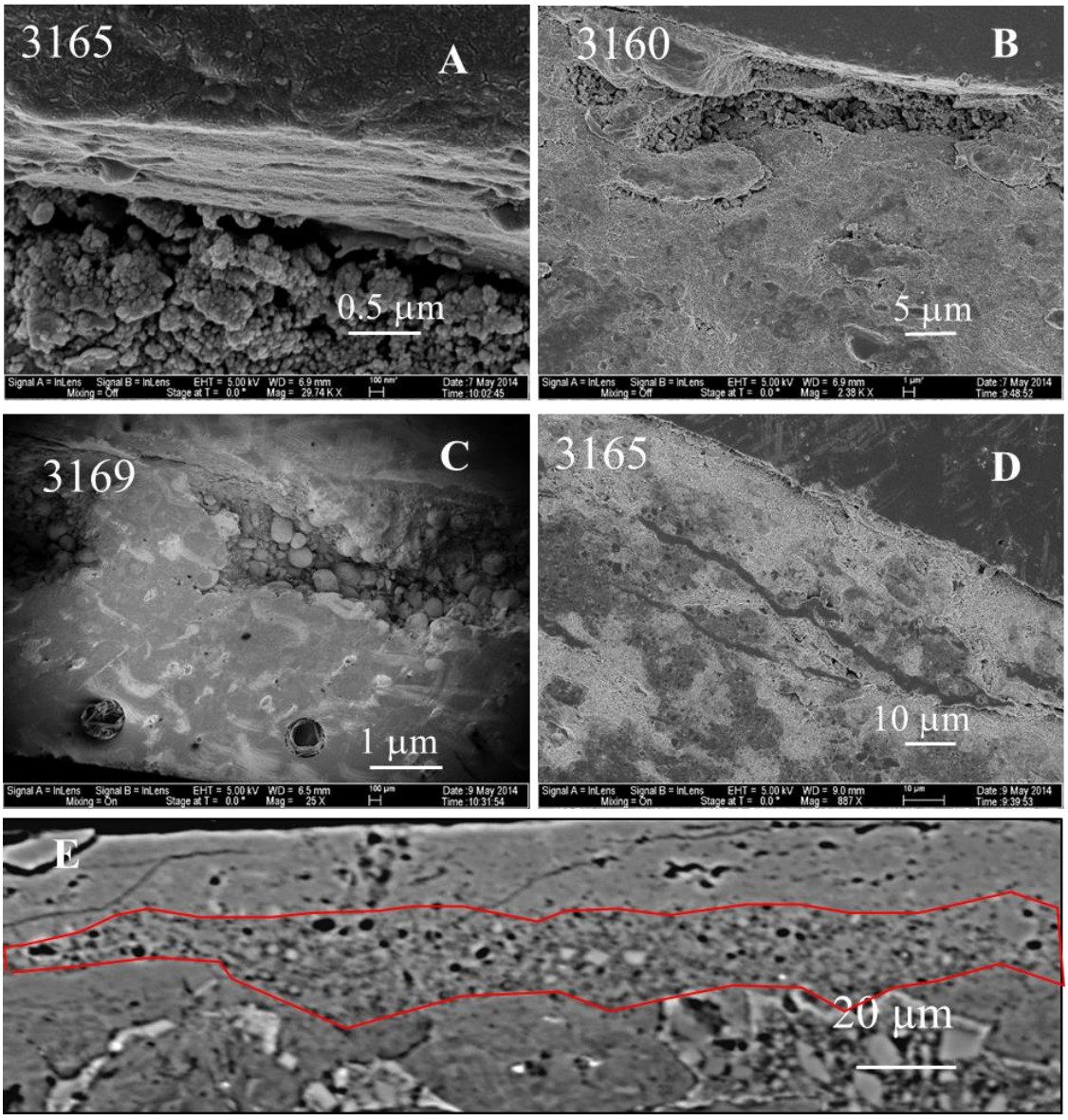

Figure 47. SEM images of cross sections for Kasota dolomite gouge experiments (3160 and 3165), ooid gouge (3169), and dolomite solid rock (1516, E). A, D, and E were cut normal to slip direction. B and C were cut along slip direction.

Fault zone surface structure

Shiny smooth fault surfaces similar to the carbonate solid rock friction experiments (Chapter 2) were developed in both dolomite gouge and ooid grains experiments. Microscopic observation of the fault surfaces showed highly smooth surfaces composed of tight packing nano-grains(Fig. 48B-D), recarbonation as indicated by hexagonal pavements (Fig. 48C, Green et al. 2010), degassing with pores left on fault surface (Fig. 48B), and partial decarbonation confirmed by backscatter image. These features are similar to the carbonate solid rock experiments for both the dolomite grains and ooids.

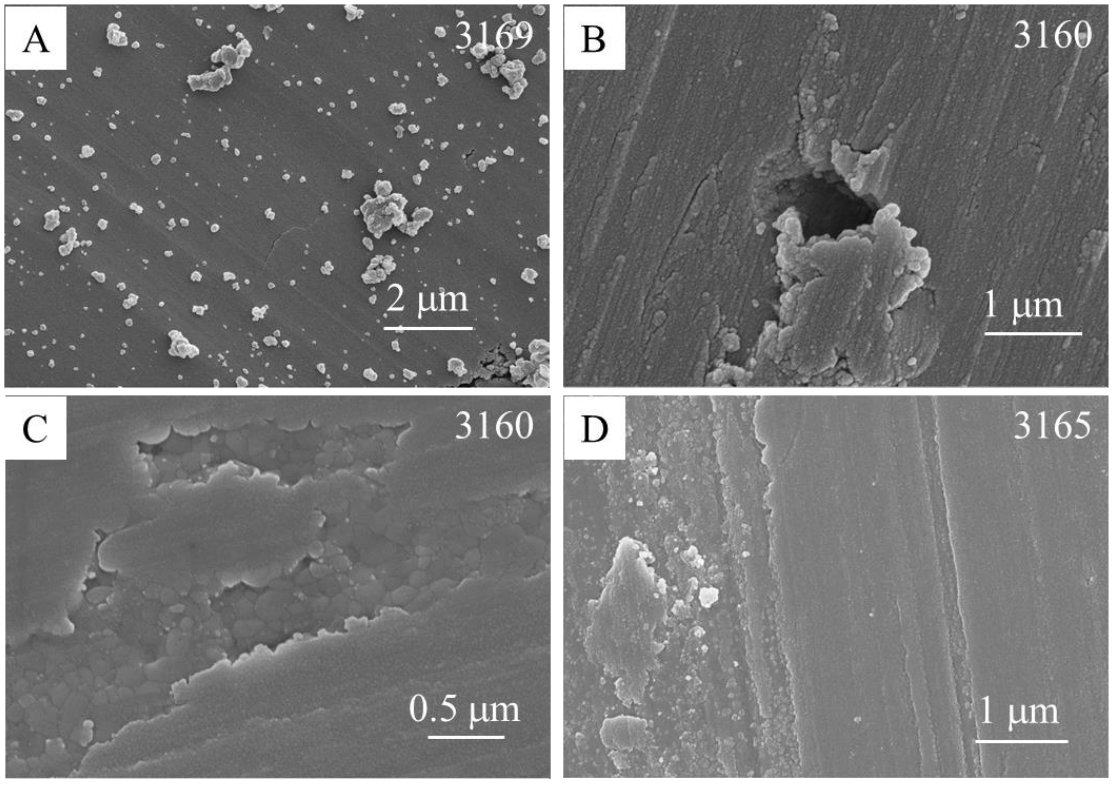

Figure 48. High-resolution SEM images of fault surface structures for gouge experiments with KD and ooid grains.

Shear experiments of gypsum grains

Micro-structure

Crushed gypsum crystals were used to run friction tests at a velocity of 0.05 m/s and normal stress of 2.6 MPa (run 2671-2674). SEM images of the gypsum gouge are shown in Fig. 49. Large areas of the gypsum fault surfaces were flat and smooth (Fig. 49A-C) and composed of fractured submicron gypsum grains (Fig. 49B, C). The fractured grains appeared elongated (Fig. 49B, E), indicating that slip along cleavage was the main pulverization mechanism. Finer grains, below 100 nm, appeared rounded and had a tendency to compact tighter (Fig. 49C) and more adhesive to form grain aggregates (Fig. 49E, F). Powder rolls (Chapter 4) composed of gypsum nano-grains were also observed (Fig. 49D-F).

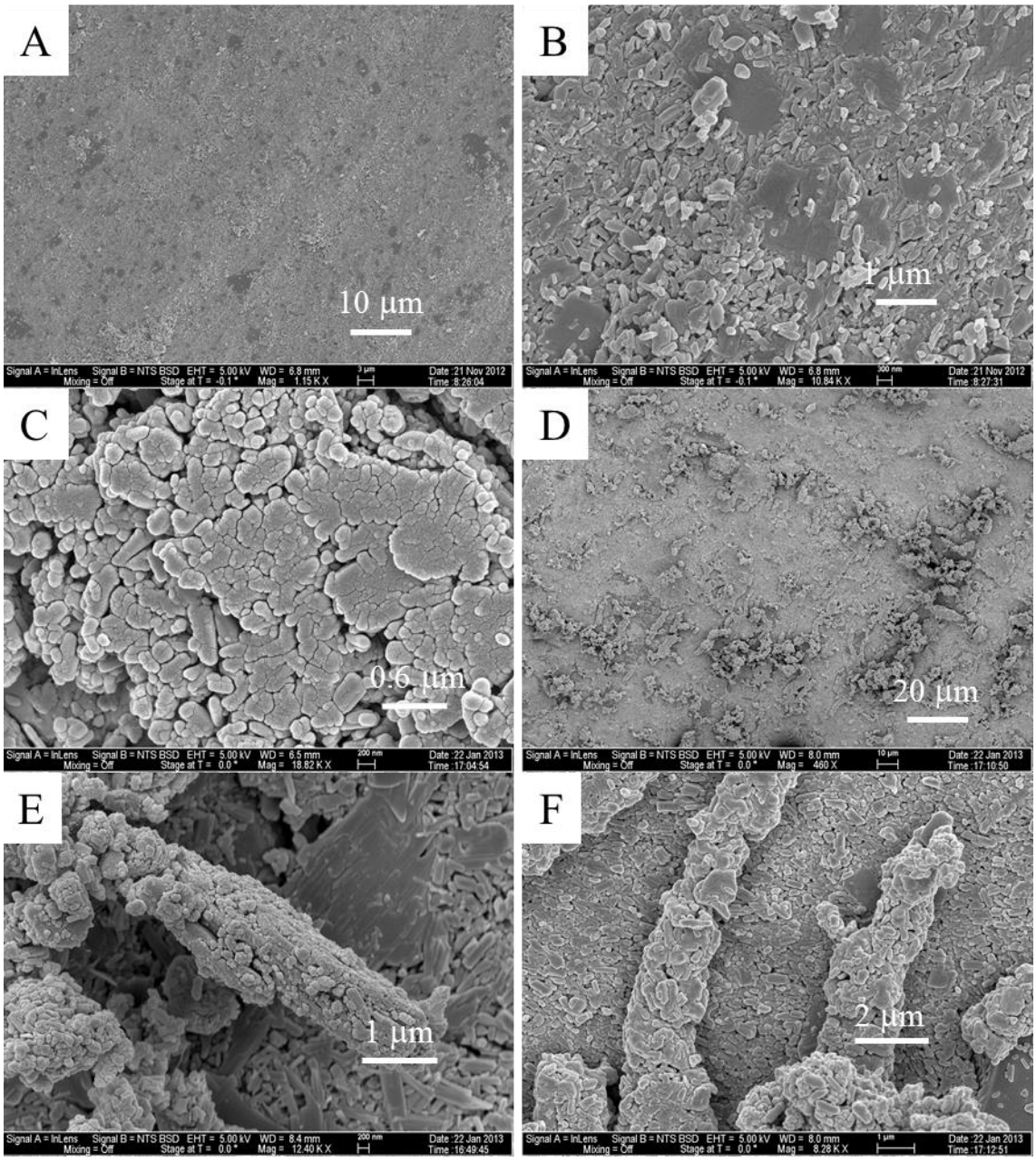

Figure 49. SEM images of the gypsum fault surfaces. A. General view of the well-developed fault surface, with visible striations. B. Close-up view of the fault surface showing the constituent elongated gypsum grains. C. Zoom-in view of the flat surfaces composed of round nano-grains. D. General view of the powder roll along fault surfaces. E. An aggregated roll lying on top of a flat substrate, note the elongated grains in the bottom surface. F. Close-up view of the roll structure showing the constituent nano-grains.

Mineralogy

The glancing incidence XRD method was used to determine the mineralogical composition of the gypsum fault surface to detect possible mineralogical alterations near fault surface. The X-ray beam was incident onto the sample at a very shallow angle close to the fault plane, ensuring the interaction between X-rays and sample largely came from the near-surfaces. The results (Fig. 50) indicate bassanite ($CaSO_4 \cdot 0.5H_2O$) peaks in the post-shearing powder, while the starting material contains only gypsum ($CaSO_4 \cdot 2H_2O$). This observation indicates thermal decomposition of gypsum (Prasad, 1999).

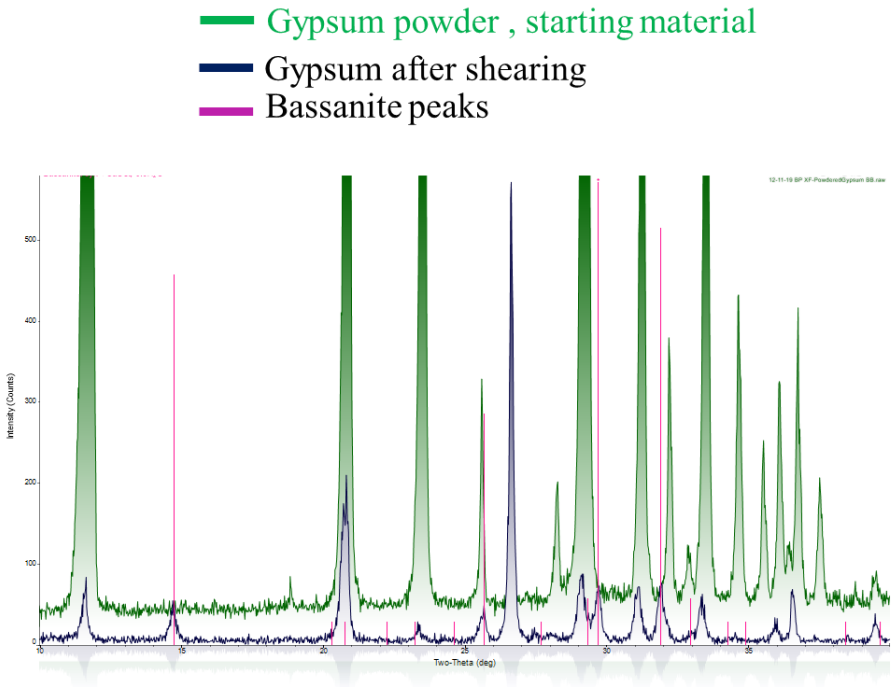

Figure 50. XRD pattern for the gypsum (green) and the post-shearing gypsum fault surface (blue). Note the bassinite peaks in the post-shear material (pink).

Summary

Compaction

Due to the loose packing of the starting gouge made of the granular materials, the gouge layers underwent significant compacting during initial shear (Fig. 43). This compaction led to tight packing and grain size reduction caused the volume decrease. On the other hand, powder materials do not always have the tendency to compact. Dry talc powder has strong tendency to expand by thrusting along Riedel shears, and carbonate faults contain a highly porous layer just beneath the tight packing top crust (Fig. 47). In solid rock experiments, gouge powders generated in the shear zone can eject out, and this may lead to different compaction behaviors (Boneh et al. 2013, 2014).

Localization

The effect of localization is strikingly similar in both gouge experiments in CROC and solid rock experiments in the standard ROGA runs (Chapter 3, 4). Slip was localized in a narrow zone represented by well-developed fault planes with cumulative displacements. Frictional heat and associated chemical reactions also developed and localized along these slip surfaces.

References

Amontons, G. 1699, Method of substituting the force of fire for horse and man power to move machines, Histoire et Mémoires de l'Académie Royale des Sciences, p.112.

Andrews, D.J. 2002, A fault constitutive relation accounting for thermal pressurization of pore fluid, J. Geophys. Res., v. 107, p. 2363.

Attard, P., Stiernstedt, J., and Rutland, M.W., 2007, Measurement of friction coefficient with the atomic force microscope.Journal of Physics: Conference Series, v. 61, p. 51–55.

Ben-Zion, Y. & Sammis, C. G., 2003, Characterization of fault zones. Pure and Applied Geophysics, v. 160, p. 677-715.

Boch, P., Platon, F., Kapelski, G., 1989, Tribological and interfacial phenomena in Al2O3/SiC and SiC/SiC couples at high temperature. Journal of the European Ceramic Society, v. 5, p. 223-228.

Boneh, Y., 2012, Wear and gouge along faults: experimental and mechanical analysis [Master thesis]: Norman, University of Oklahoma, 72p.

Boneh, Y., Sagy, A. & Reches, Z., 2013, Frictional strength and wear-rate of carbonate faults during high-velocity, steady-state sliding. Earth and Planetary Science Letters, v. 381, p. 127-137.

Boheh, Y., Chang, J. C., Lockner, D. A., and Reches, Z., 2014, Evolution of wear and friction along experimental faults, Pure and Applied Geophysics, v. 171, p. 3125-3141.

Boutareaud, S., Hirose, T., Andreani, M., Pec, M., Calugaru, D., Boullier, A., and Doan, M., 2012, On the role of phyllosilicates on fault lubrication: insight from micro-

and nanostructural investigations on talc friction experiments. J. Geophys. Res. 117, B08408.

Bowden, F. P. & Tabor, D. 1954. The friction and lubrication of solids, ch. V. Oxford, UK: Oxford University Press.

Brace, W.F. & Byerlee, J.D. 1966, Stick-slip as a mechanism for earthquakes, Science, 153, p. 990-992.

Brodsky, E. E. & Kanamori, H., 2001, Elastohydrodynamic lubrication of faults. Journal of Geophysical Research, v. 106, p. 16357-16374.

Brown, K.M. and Fialko, Y. 2012, 'Melt welt' mechanism of extreme weakening of gabbro at seismic slip rates, Nature, 488, 638-641.

Byerlee, J.D., 1967, Theory of friction based on brittle fracture: Journal of Applied Physics, v. 38, p. 2928–2934.

Byerlee, J.D., 1978, Friction of rocks: Pure and Applied Geophysics, v. 116, p. 615–626.

Candela, T., Renard, F., Bouchon, M., Schmittbuhl, J., and Brodsky, E.E., 2011, Stress drop during earthquakes: Effect of fault roughness scaling: Bulletin of the Seismological Society of America, v. 101, p. 2369–2387.

Carpick, R.W., Agrait, N., Ogletree, D.F., and Salmeron, M., 1996, Variation of the interfacial shear strength and adhesion of a nanometer-sized contact: Langmuir, v. 12, p. 3334–3340.

Chang, J. C., Lockner, D. A., and Reches, Z., 2012, Rapid acceleration leads to rapid weakening in earthquake-like laboratory experiments; Science, v. 338, p. 101-105.

Chen, X., Madden, A. S., Bickmore, B. R., Reches, Z., 2013, Dynamic weakening by nanoscale smoothing during high velocity fault slip. Geology, v. 41, p. 739-742.

Chen, X., Madden, A. S., and Reches, Z. 2015, Frictional melting of granite faults as mechanical and material phase transition, in preparation.

Chester, F. M., Evans, J. P., Biegel, R. L., 1993, Internal structure and weakening mechanisms of the San Andreas fault. Journal of Geophysical Research, v. 98, p. 771-786.

Chester, J. S., Chester, F. M., Kronenberg, A. K., 2005, Fracture surface energy of the Punchbowl fault, San Andreas system. Nature, v. 437, p. 133-136.

Collettini, C. Niemeijer, A., Viti, C., and Marone, C. 2009, Fault zone fabric and fault weakness, Nature, 462, 907-910.

Del Gaudio, P., Di Toro, G., Han, R., Hirose, T., Nielsen, S., Shimamoto, T., and Cavallo, A., 2009, Frictional melting of peridotite and seismic slip, J. Geophys. Res. 114, B06306.

Di Toro G., Goldsby D. L., Tullis T. E., 2004, Friction falls towards zero in quartz rock as slip velocity approaches seismic rates. Nature, 427, 436-439.

Di Toro, G., Hirose, T., Nielsen, S., Pennacchioni, G. and Shimamoto, T. 2006. Natural and experimental evidence of melt lubrication of faults during earthquakes. Science, 331, 647-649.

Di Toro, G., Han, R., Hirose, T., De Paola, N., Nielsen, S., Mizoguchi, K., Ferri, F., Cocco, M. and Shimamoto, T. 2011. Fault lubrication during earthquakes. Nature, 471, 494-498.

Dieterich, J.H., 1978, Time-dependent friction and the mechanics of stick-slip, Pageoph, v. 116, p. 790-806.

Dieterich, J. H., 1979, Modeling of rock friction: 1. Experimental results and constitutive equations. Journal of Geophysical Research, v. 84, p. 2161-2168.

Dieterich, J.H., and Kilgore, B.D., 1994, Direct observation of frictional contacts: New insights for state-dependent properties: Pure and Applied Geophysics, v. 143, no. 1–3, p. 283–302.

Dong, X., Said, J., Stephen, M. H., 1991, Tribological characteristics of α-Alumina at elevated temperatures. Journal of the American Ceramic Society, v. 74, no. 5, p. 1036-1044.

Eldredge, K. R. & Tabor, D., 1955, The mechanism of rolling friction. I. the plastic range. Proceedings of the Royal Society A, v. 229, p. 181-198.

Fialko, Y. and Khazan, Y. 2005, Fusion by earthquake fault friction: Stick or slip? J. Geophys. Res., 110, B12407.

Fukuyama, E., Mizoguchi, K., 2010. Constitutive parameters for earthquake rup-ture dynamics based on high-velocity friction tests with variable slip rate. Int. J.Fract.163, 15–26.

Goldsby, D. L. & Tullis, T. E., 2002, Low frictional strength of quartz rocks at subseismic slip rates. Geophysical Research Letters, v. 29, p. 25-1 – 25-4.

Goldsby, D. L. & Tullis, T. E., 2011, Flash heating leads to low frictional strength of crustal rocks at earthquake slip rates. Science, v. 334, p. 216-218.

Green, H.W., Lockner, D.A., Bozhilov, K.N., Madden, A.S., Beeler, N.M., and Reches, Z., 2010, Nanometric gouge in high-speed shearing experiments: Superplasticity?: American Geophysical Union, Fall Meeting 2010, Abstract #T31D-08.

Gunasekaran, S. and Anbalagan, G. 2007, Thermal decomposition of natural dolomite, Bull. Mater. Sci. 30, 339-344.

Han, R., Shimamoto, T., Hirose, T., Ree, J. and Ando, J. 2007a, Ultralow friction of carbonate faults caused by thermal decomposition. Science, 316, 878-881.

Han, R.H., Shimamoto, T., Ando, J.I., and Ree, J.H., 2007b, Seismic slip record in carbonate-bearing fault zones: An insight from high-velocity friction experiments on siderite gouge: Geology, v. 35, p. 1131–1134.

Han, R., Hirose, T., Shimamoto, T., 2010, Strong velocity weakening and powder lubrication of simulated carbonate faults at seismic slip rates. Journal of Geophysical Research, v. 115, p. B03412.

Hayashi, N. & Tsutsumi, A., 2010, Deformation textures and mechanical behavior of a hydrated amorphous silica formed along an experimentally produced fault in chert. Geophysical Research Letters, v. 37, p. L12305.

Hayward, I.P., Singer, I.L., and Seitzman, L.E., 1992, Effect of roughness on the friction of diamond on CVD diamond coatings: Wear, v. 157, p. 215–227.

Hertz, H. 1881, On the contact of elastic solids, J. ReineAngew. Math.92, 156.

Heshmat, H., 1995, The quasi-hydrodynamic mechanism of powder lubrication-part III: on theory and rheology of triboparticulates. Tribology Transactions, v. 38, p. 269-276.

Hirose, T. & Shimamoto, T. 2005, Growth of molten zone as a mechanism of slip weakening of simulated faults in gabbro during frictional melting, J. Geophys. Res., 110, B05202.

Katz, O., Reches, Z., Baer, G., 2003, Faults and their associated host rock deformation: part I. structure of small faults in a quartz-syenite body, southern Israel. Journal of Structural Geology, v. 25, p. 1675-1689.

Kosoglu, L.M., Bickmore, B.R., Filz, G.M., and Madden, A.S., 2010, Atomic force microscopy method for measuring smectite coefficient of friction: Clays and Clay Minerals, v. 58, p. 813–820.

Kuwano, O. & Hatano, T. 2011, Flashing weakening is limited by granular dynamics, Geophys. Res. Lett., 38, L17305.

Li, Q., and Kim, K., 2008, Micromechanics of friction: effects of nanometer-scale roughness: Proceedings of the Royal Society of London. Series A, v. 464, p. 1319–1343.

Li, Q., Tullis, T.E., Goldsby, D.L., and Carpick, R.W., 2011, Frictional ageing from interfacial bonding and the origins of rate and state friction: Nature, v. 480, p. 233–236.

Liao, Z., and Reches Z, 2012, Modeling Dynamic-Weakening and Dynamic-Strengthening of Granite in High-Velocity. Chapter in "Earthquake Research and Analysis - New Advances in Seismology", open access book.

Liao, Z, Chang, JC, Reches, Z, 2014, Fault strength evolution during high velocity friction experiments with slip-pulse and constant-velocity loading. Earth and Planetary Science Letters, V. 406, p. 93-101.

Lin, A. 2008. Fossil earthquakes: the formation and preservation of pseudotachylytes. Springer.

Lockner, D. A. & Okubo, P. G., 1983, Measurements of frictional heating in granite. Journal of Geophysical Research, v. 88, p. 4313–4320.

Lu, K., Brodsky, E. E., Kavenpour, H. P., 2007, Shear-weakening of the transitional regime for granular flow. Journal of Fluid Mechanics, v. 587, p. 347-372.

Madden, A.S., Hochella Jr, M.F., Glasson, G.E., Grady, J.R., Bank, T.L., Green, A.M., Norris, M.A., Hurst, A.N., Eriksson, S.C., 2011, Welcome to nanoscience: interdisciplinary environmental explorations, grades 9-12, NSTA Press.

Mair, K, & Marone, C. J., 1999, Friction of simulated fault gouge for a wide range of velocities and normal stresses. Journal of Geophysical Research, v. 104, p. 28,899-28,914.

Marone, C. 1998, The effect of loading rate on static friction and the rate of fault healing during the earthquake cycle. Nature, 391, 69-72.

Maurice, P.A., and Lower, S.K., 2008, Use of atomic force microscopy to study soil particle properties and interactions, in Treloar, P.J., and Searle, M., eds., Methods of Soil Analysis, Part 5, Mineralogical Methods, p. 299-334, Madison, Soil Science Society of America.

Meyer, G. and Amer, N.M. 1990, Simultaneous measurement of lateral and normal forces with an optical beamdeflection atomic force microscope, Appl, Phys. Lett. 57, 2089.

Mizoguchi, K., Hirose, T., Shimamoto, T., Fukuyama, E., 2007, Reconstruction of seismic faulting by high-velocity friction experiments: an example of the 1995 Kobe earthquake. Geophys. Res. Lett. v. 34, p. L01308.

Mo, Y., Turner, K.T., and Szlufarska, I., 2009, Friction laws at the nanoscale: Nature, v. 457, p. 1116–1119.

Moore, D.E., and Rymer, M.J., 2007, Talc-bearing serpentinite and the creeping section of the San Andreas fault: Nature, v. 448, p. 795–797.

Mourchid, A., Delville, A., Lambard, J., Lecolier, E. and Levitz, P. 1995. Phase diagram of colloidal dispersions of anisotropic charged particles: equilibrium properties, structure, and rheology of laponite suspensions. Langmuir, 11, 1942-1950.

Nakamura, Y., Muto, J., Nagahama, H., Shimizu, I., Miura, T., Arakawa, I., 2012, Amorphization of quartz by friction: Implication to silica-gel lubrication of fault surfaces. Geophysical Research Letters, v. 39, p. L21303.

Niemeijer, A., Di Toro, G., Nielsen, S., and Di Felice, F. 2011, Frictional melting of gabbro under extreme experimental conditions of normal stress, acceleration, and sliding velocity, J. Geophys. Res., 116, B07404.

Power, W. L., Tullis, T. E. & Weeks, J. D. 1988. Roughness and wear during brittle faulting. J. Geophys. Res. 93, 15268-15278.

Power, W.L., and Tullis, T.E., 1991, Euclidean and fractal models for the description of rock surface roughness: Journal of Geophysical Research, v. 96, p. 415–424.

Power, W.L., Tullis, T.E., Brown, S.R., Boitnott, G.N., and Scholz, C.H., 1987, Roughness of natural fault surfaces: Geophysical Research Letters, v. 14, no. 1, p. 29–32.

Reches, Z. & Lockner, D. A., 2010, Fault weakening and earthquake instability by powder lubrication. Nature, v. 467, p. 452-455.

Renard, F., Voisin, C., Marsan, D., and Schmittbuhl, J., 2006, High resolution 3D laser scanner measurements of a strike-slip fault quantify its morphological anisotropy at all scales: Geophysical Research Letters, v. 33, L04305.

Rice, J. R. 1999, Flash heating at asperity contacts and rate-depend friction, Eos Trans AGU, 80(46), Fall Meet. Suppl., F681.

Rice, J. R. 2006, Heating and weakening of faults during earthquake slip, J. Geophys. Res. 111, B05311.

Rubinstein, S.M., Cohen, G. and Fineberg, J. 2004, Detachment fronts and the onset of dynamic friction, Nature, 430, 1005-1009.

Sader, J. E., Chon, J. W. M. & Mulvaney, P. 1999. Calibration of rectangular atomic force microscope cantilevers. Rev. Sci. Instrum.70, 3967-3969.

Sagy, A., Beodsky, E.E., and Axen, G.J., 2007, Evolution of fault-surface roughness with slip: Geology, v. 35, p. 283–286.

Sagy, A. & Brodsky, E. E. 2009. Geometric and rheological asperities in an exposed fault zone. J. Geophys. Res. 114, B02301.

Sammis, C.G., Lockner, D.A., and Reches, Z. 2011, The role of adsorbed water on the friction of a layer of submicron particles, Pure and Applied Geophysics, 168, 2325-2334.

Scholz, C.H., 1998, Earthquakes and friction laws: Nature, v. 391, p. 37–42.

Shibayama, M., Morioto, M. and Nomura, S. 1994. Phase separation induced mechanical transition of poly (N-isopropylacrylamide)/water isochore gels. Macromolecules, 27, 5060-5066.

Shimamoto, T. and Lin, A. 1994, Is frictional melting equilibrium melting, or non-equilibrium melting? J. Tectonic Res. Group of Japan, 39, 79-84.

Sibson, R. H., 2003, Thickness of the seismic slip zone. Bulletin of the Seismological Society of America, v. 93, p. 1,169-1,178.

Siman-Tov, S., Aharonov, E., Sagy, A., Emmanuel, S., 2013, Nanograins form carbonate fault mirrors. Geology, v. 41, p. 703-706.

Smith, S. A. F., Billi, A., Di Toro, G., Spiess, R., 2011, Principal slip zones in limestone: microstructural characterization and implications for the seismic cycle (Tre Monti Fault, Central Apennines, Italy). Pure and Applied Geophysics, v. 168, p. 2365-2393.

Smith, S.A.F., Di Toro, G., Kim, S., Ree, J.H., Nielsen, S., Billi, A., and Spiess, R., 2012, Co-seismic recrystallization during shallow earthquake slip: Geology, v. 41, p. 63-66.

Spray, J.G. 1993. Viscosity determinations of some frictionally generated silicate melts: implications for fault zone phenology at high strain rates. J. Geophys. Res. 98, 8053-8068.

Spray, J.G. 2005. Evidence for melt lubrication during large earthquakes. Geophys. Res. Lett. 32, L07301.

Spray, J.G. 2010. Frictional melting processes in planetary materials: from hypervelocity impact to earthquakes. Annu. Rev. Earth Planet. Sci. 38, 221-254.

Stiernstedt, J., Rutland, M.W., and Attard, P., 2005, A novel technique for the in situ calibration and measurement of friction with the atomic force microscope: The Review of Scientific Instruments, v. 76, 083710.

Tabor, D., 1955, The mechanism of rolling friction. II. The elastic range. Proceedings of the Royal Society A, v. 229, p. 198-220.

Tisato, N., Di Toro, G., De Rossi, N., Quaresimin, M., and Candela, T., 2012, Experimental investigation of flash weakening in limestone: Journal of Structural Geology, v. 38, p. 183–199.

Tsutsumi, A. & Shimamoto, T., 1997, High-velocity frictional properties of gabbro. Geophysical Research Letters, v. 24, p. 699-702.

Tullis, T.E., 1996, Rock friction and its implications for earthquake prediction examined via models of Parkfield earthquakes: Proceedings of the National Academy of Sciences of the United States of America, v. 93, p. 3803–3810.

Wilson, B., Dewers, T., Reches, Z., Brune, J., 2005, Particle size and energetics of gouge from earthquake rupture zones. Nature, v. 434, p. 749-752.

Wornyoh, E.Y.A., Jasti, V.K. and Higgs III, C.F. 2007, A review of dry particulate lubrication: powder and granular materials, J. Tribology, 129, 438-449.

Zanoria, E. S., Danyluk, S., McNallan, M. J., 1995a, Formation of cylindrical sliding-wear debris on silicon in humid conditions and elevated temperatures. Tribology Transactions, v. 38, p. 721-727.

Zanoria, E. S., Danyluk, S., McNallan, M. J., 1995b, Effects of length, diameter and population density of tribological rolls on friction between self-mated silicon. Wear, v. 181-183, p. 784-789.

Zoback, M.D. & Zoback, M.L. 1981, State of stress and intraplate earthquakes in the central and eastern United States, Science, 213, p. 96-104.